Dimitrios E. Kiousis

Biomechanical and Computational Modeling of Atherosclerotic Arteries

Monographic Series TU Graz

Computation in Engineering and Science

Series Editors

Monographic Series TU Graz

Computation in Engineering and Science Volume 4

Dimitrios E. Kiousis

Biomechanical and Computational Modeling of Atherosclerotic Arteries

Insights into Plaque Vulnerability and Vascular Stenting

This work is based on the dissertation *Biomechanical and Computational Modeling of Atherosclerotic Arteries*, presented by Dimitrios E. Kiousis at Graz University of Technology, Institute for Biomechanics in September 2008.
Supervisor: G. Holzapfel (Graz University of Technology)

Bibliographic information published by Die Deutsche Bibliothek.
Die Deutsche Bibliothek lists this publication in the Deutsche Nationalbibliografie; detailed bibliographic data are available at http://dnb.ddb.de.

Cover photo	Vier-Spezies-Rechenmaschine by courtesy of the Gottfried Wilhelm Leibniz Bibliothek – Niedersächsische Landesbibliothek Hannover
Layout	Wolfgang Karl, TU Graz / Universitätsbibliothek
Printed	by TU Graz / Büroservice

Verlag der Technischen Universität Graz

www.ub.tugraz.at/Verlag

ISBN: 978-3-85125-023-7

Abstract

In western countries, cardiovascular disease is the most common cause of death, often related to atherosclerosis which can cause narrowing, rupture or erosion of the arterial wall, and eventually reduction or complete blockage of the blood flow.

Nowadays, imaging modalities (MRI, IVUS) have the ability to identify morphological characteristics of rupture-prone plaques. Additionally, recent advances in stent technology (drug elution) have improved the outcome of angioplasty. However, reliable vulnerability analyses require additional information on the mechanical stresses occurring in the lesion's structural components. There is also a pressing need to deeper and better understand the mechanical characteristics of the transient expansion of balloon-expandable stent systems inside the arterial wall in order to improve the clinical protocols and decrease in-stent restenosis rates.

This thesis presents a computational methodology, able to accurately (i) analyze the mechanical environment of atherosclerotic lesions and consequently identify high-risk plaques, and (ii) simulate the mechanical aspects of angioplasty interventions and study the outcome of different stent designs.

In particular, the thesis considers patient-specific models of human stenotic lesions. This is accomplished by means of MRI, automatic segmentation algorithms and NURBS modeling. The inhomogeneity of the plaque is regarded, and the adopted constitutive models account for the nonlinear, anisotropic, incompressible behavior of the arterial constituents. To avoid stability problems during the interaction between the arterial wall and the medical devices, surface smoothing techniques are employed. In order to assess the vulnerability risk of lesions or the performance of stent geometries, novel scalar indices are introduced, linked to mechanical measures such as stress changes.

The proposed morpho-mechanical approaches are able to investigate quantitatively the biomechanical behavior of atherosclerotic plaques and to provide clear markers for the patient-specific choice of the optimal stent configuration.

Keywords–balloon angioplasty, stenting, contact, C^2-continuity, plaque vulnerability, finite element method

Zusammenfassung

In den westlichen Ländern sind Herz-Kreislauf-Erkrankungen die häufigste Todesursache. Diese treten meist in Verbindung mit Atherosklerose auf, die eine Verengung, Ruptur oder Erosion der Arterienwand verursacht und den Blutfluss reduzieren oder komplett blockieren kann.

Heutzutage ermöglichen bildgebende Verfahren (MRI, IVUS) die morphologische Eigenschaften von rupturanfälligem Plaque zu identifizieren. Weiters haben neue Fortschritte in der Stenttechnologie (drug elution) die Ergebnisse einer Angioplastie verbessert. Verlässliche Verwundbarkeitsanalysen brauchen jedoch zusätzliche Informationen über die mechanischen Spannungen die in den strukturellen Komponenten der Verletzung auftreten. Außerdem besteht dringender Bedarf die mechanischen Eigenschaften von ballonerweiterbaren Stentsystems in der Arterienwand besser zu verstehen um die klinischen Protokolle zu verbessern und die Rate von in-stent Restenosen zu verringern.

Die vorliegende Dissertation präsentiert eine computerunterstützte Methode, die es ermöglicht (i) die mechanische Umgebung von atherosklerotischen Verletzungen präzise zu analysieren und in weiterer Folge Hochrisiko-plaques zu identifizieren und (ii) den mechanischen Aspekt von angioplastischen Eingriffen genau zu simulieren und die Ergebnisse verschiedener Stent-Designs zu studieren.

Im Besonderen berücksichtigt diese Dissertation patienten-spezifische Modelle von menschlichen stenotischen Läsionen. Dies wird mit Hilfe von MRI, automatischen Segmentationsalgorithmen und NURBS-Modellierung bewerkstelligt. Die Inhomogenität von Plaques wird berücksichtigt und das adoptierte konstitutive Modell begründet das nichtlineare, anisotrope, inkompressible Verhalten der arteriellen Bestandteile. Um Stabilitätsprobleme während der Interaktion zwischen Arterienwand und dem Stent zu vermeiden werden oberflächenglättende Techniken eingesetzt. Um das Verwundbarkeitsrisiko von Läsionen oder die Effizienz der Stentgeometrie festzustellen, wurden neue Skalarindizes eingeführt, die mit mechanischen Maßen, wie z.B. Spannungsveränderungen, verbunden wurden.

Der vorgeschlagene morpho-mechanische Ansatz ermölicht es, das biomechanische Verhalten von atherosklerotischen Arterien quantitativ zu untersuchen um Wegweiser für die patienten-spezifische Wahl der optimalen Stentkonfiguration bereitszustellen.

Schlagwörter–Ballon Angioplastie, Stenting, Kontakt, C^2-Kontinuität, Finite Elemente Methode

CONTENTS

1 INTRODUCTION AND MOTIVATION

1.1 Cardiovascular diseases and atherosclerosis

Cardiovascular diseases (CVDs) include high blood pressure (HBP), coronary heart disease (CHD), heart failure (HF) and stroke. According to the latest statistical data, they are the number one cause of morbidity and mortality in countries of the western world [148]. Nearly 2400 Americans die of CVDs each day (an average of 1 death every 37 seconds) while in Europe, CVDs account for more than 40% of total deaths[137]. The social and economical burden of the disease remains very high, and the importance of understanding better the natural history of CVDs, including the *biomechanics*, cannot be overemphasized.

CVDs are mainly caused by *atherosclerosis*, a common disorder of the arteries, characterized by accumulation of cells, lipids, connective tissue, calcium, and other substances inside the inner lining of the arterial wall. This fatty tissue –known as atheroma– can cause hardening of the arteries, rupture or erosion of the arterial wall, and eventually reduction or complete blockage of the blood flow. Atherosclerosis appears preferentially at sites of complex geometry (e.g., along the outer portions of the bifurcation), most often in the abdominal aorta, iliacs, coronaries, femorals, popliteals, carotids, and cerebrals. The atherosclerotic process starts early in life and advances throughout adulthood. Risk factors for atherosclerosis include elevated serum cholesterol (i.e., hyperlipidemia), cigarette smoking, diabetes mellitus, a genetic predisposition, social stress or a sedantary lifestyle, and hypertension.

1.1.1 Pathogenesis and progression of atherosclerosis

Atherosclerosis is a highly progressive disease; it tends to begin as a fatty streak on the endothelial surface but usually develops into a focally thickened intima. The etiology of atherosclerosis is not understood completely, but there have been many hypotheses. The 'responce-to-injury' hypothesis by Ross [149] suggests that 'lesions result from an excessive, inflammatory-fibroproliferative response to various forms of insult to the endothelium and smooth muscle of the arterial wall'. In particular, it was suggested that following an insult, monocytes adhere to the altered endothelium and then migrate into the inner wall where they transform into macrophages and eventually lipid-laden foam cells. In concert, contributing events include migration of smooth muscle cells into the intima, production of proteases and growth factors, altered apoptosis, attendant degradation and synthesis of

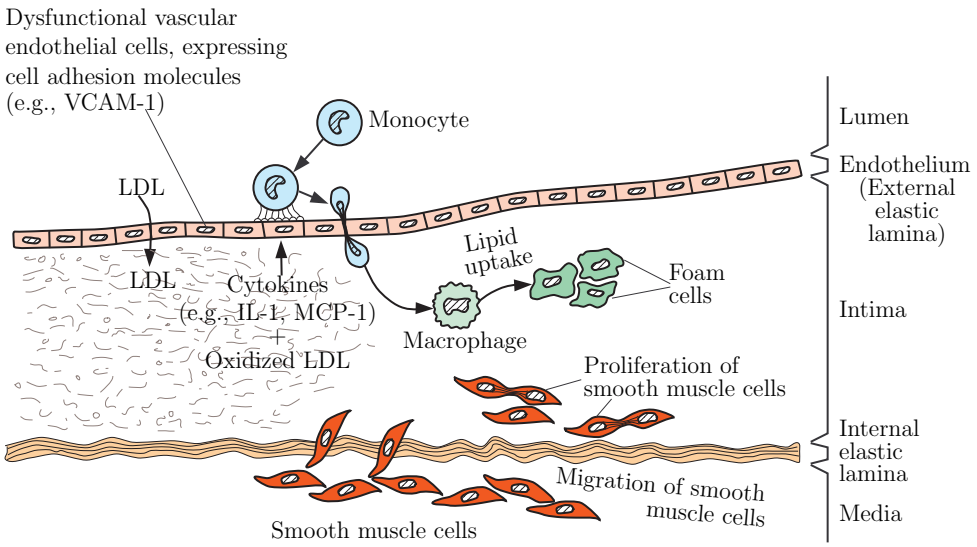

Figure 1.1: Progression of atherosclerosis. Endothelial dysfunction due to inury leads to adherence of monocytes and macrophages to the intima. These cells later migrate and localize subendothelially. Macrophages accumulate lipid and become large foam cells and together with smooth muscle cells form a fatty streak. The fatty streak can progress to an intermediate, fibrofatty lesion and ultimately to a fibrous plaque. Illustration based on [90].

matrix in the intima, and local accumulation of calcium [58, 149, 155]. Figure 1.1 demonstrates in detail the progression of atherosclerosis.

Inflammation during macrophage foam cell formation plays an important role during the progression of atherosclerosis, because it is involved with lesion initiation, lesion progression, and with thrombotic complications. Hence, inflammation of the artery is the main factor leading to early atheromas. From this stage on, the stenosis can either progress into a stable plaque or a vulnerable plaque (see Figure 1.2). The main characteristics of these lesions are as following.

- *Stable*: The fibrous plaque is localized under the intima resulting into thickening and expansion of the wall, and often into spotty localized narrowing of the lumen, with some atrophy of the muscular layer. The fibrous plaque contains collagen fibres, precipitates of calcium, and rarely lipid-laden cells.
- *Vulnerable*: The fibro-lipid plaque is characterized by an accumulation of lipid-laden cells underneath the intima, typically without narrowing the lumen due to compensatory expansion of the bounding muscular layer of the artery wall. Beneath the endothelium there is a *fibrous cap* covering the atheromatous core of the plaque. The core, or *lipid pool* consists of macrophages and smooth muscle cells, fibrin, collagen, and cellular debris. In advanced plaques, the central core of the plaque usually contains extracellular cholesterol deposits. The periphery of the plaque is composed by younger foamy cells and capillaries. An example of such an atherosclerotic lesion

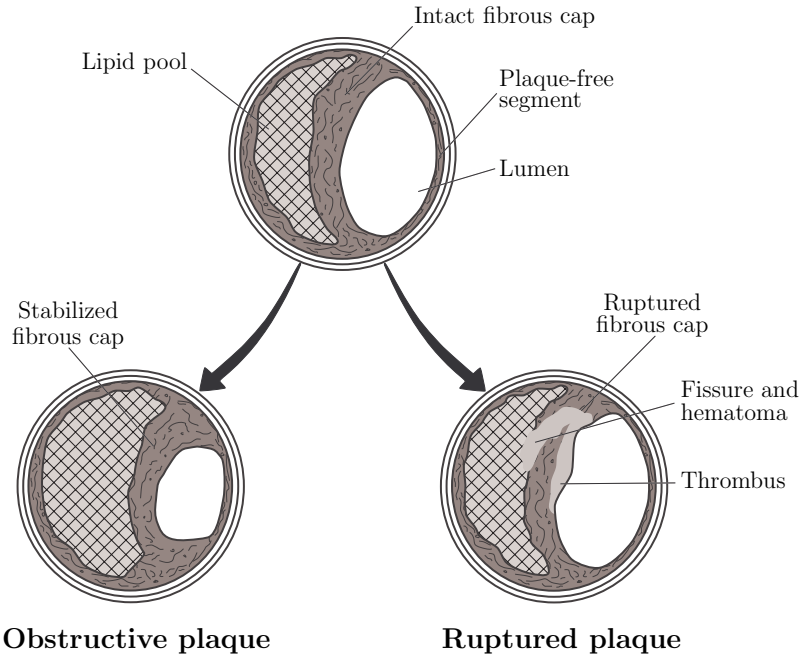

Figure 1.2: Development of an atherosclerotic lesion into a stabilized obstructive plaque, or into a ruptured plaque.

is shown in Figure 1.3.

As aforementioned, atherosclerosis progresses slowly over decades and usually remains asymptomatic until the atheroma obstructs the bloodstream in the artery. This is either by *stenosis*, which results in an obstructive stabilized plaque, or by *plaque rupture*, or often by combination of both.

While the formation of a stenosis is a slow process, the disruption of an atherosclerotic plaque is a sudden event. Plaque rupture can release embolic debris from the necrotic core of the lesion, which can eventually cause distal occlusions, or it can expose highly thrombotic collagen in the arterial wall and plaque to the bloodstream, which results in the formation of intraluminal thrombi. Obstructive thrombi are thought to associate with the most sudden cardiac events, such as acute myocardial infarction and unstable angina. It is, therefore, very important to reliably identify vulnerable plaques. Unfortunately, such a technique does not exist to date. Two examples of ruptured lesions are depicted in Figure 1.4.

The specific mechanisms by which a vulnerable plaque ruptures remain unknown. It has been hypothesized, for example, that rupture results from vasospam-induced stress and strain, hemodynamically induced fluid shear stress or pressure fluctuations, blood pressure-induced circumferential stress concentrations in the plaque cap, or negative transmural pressures in the stenosis [66, 143, 64, 115]. Regardless, the bottom line is that rupture occurs when the stress exceeds the strength. Increased strength can be achieved by increased collagen deposition and cross-linking in the plaque cap or overall increases in the number

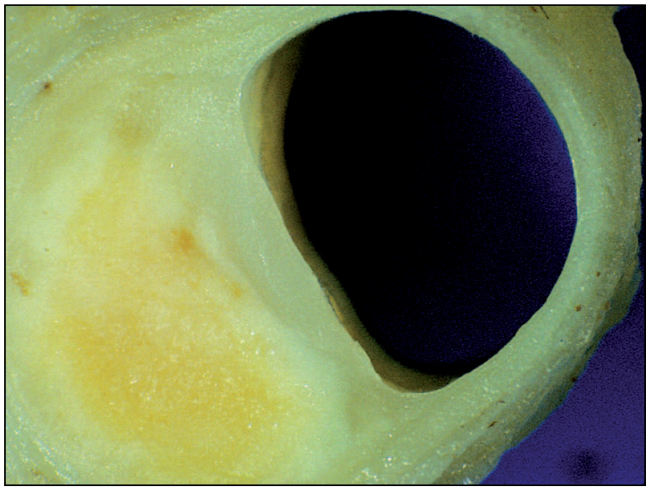

Figure 1.3: A lipid-rich atherosclerotic coronary lesion. The plaque has a core of yellow lipids that is separated from the lumen of the artery by a cap of fibrous tissue. Opposite of the plaque is an arc of normal vessel wall. Image courtesy of [30].

of smooth muscle cells and matrix in the core; decreased strength can be caused by degradation of the collagen, death of smooth muscle cells, and an increased percentage of lipids and necrotic debris in the core of the lesion.

1.1.2 Diagnosis and treatment

Nowadays, there is a number of imaging and screening techniques for diagnosis of atherosclerotic lesions and for characterization of plaques. Contrast X-ray, magnetic resonance (MR), or ultrafast computer tomography (CT), as well as intravascular ultrasound (IVUS) are widely used arterial imaging modalities. Contrast angiography is unable to image the vascular wall. Therefore, stable and vulnerable plaques cannot be delineated from angiography (% stenosis). IVUS is an excellent tool for assessing arterial plaque and wall morphology. Nevertheless, no methodology exists that can determine plaque composition with sufficient classification detail, robustness, and accuracy. Additionally, IVUS is an invasive technique, not suitable for screening purposes. Compared with other screening methods, MRI has the greatest potential for noninvasive and comprehensive assessments of atherosclerotic plaques, not only on luminal stenosis and plaque burden, but also on differentiation of plaque components such as lipid-rich necrotic core, fibrous cap, intraplaque thrombosis, and calcification [52, 53].

Atherosclerotic lesions can be treated in several ways. The most important treatment methods can be categorized to

- non-surgical (pharmacological) treatments (risk-factor minimization, reduction of fat and cholesterol in blood),
- minimally invasive treatments (balloon angioplasty, stenting)

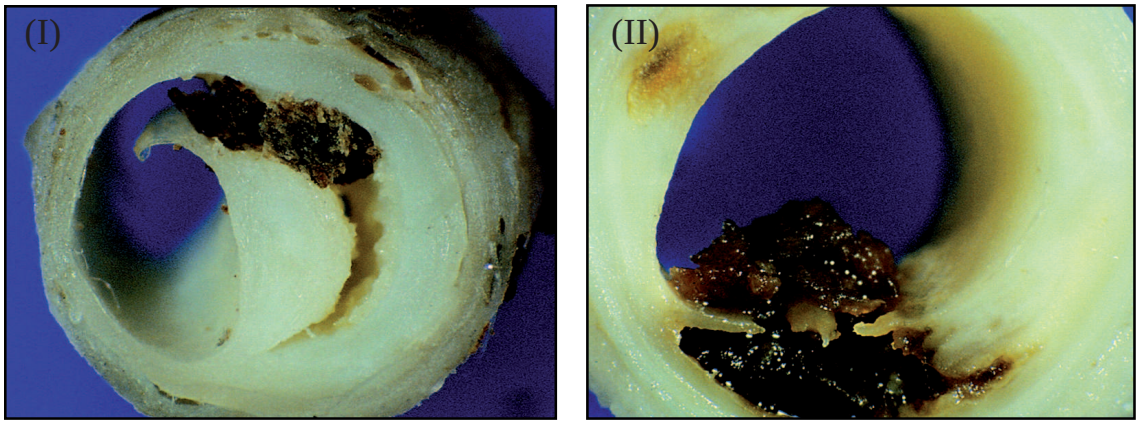

Figure 1.4: Typical lesions of unstable angina: (I) an episode of plaque disruption in the lateral edge of the cap. The torn cap projects into the lumen of the artery and thrombus is contained within the plaque core; (II) plaque with multiple breaks in the middle region of the thin fibrous cap. Both an intraplaque and intraluminal mural component of thrombosis are observed. Image courtesy of [30].

- extensive surgical treatments (bypass grafting, endarterectomy, bypass grafting, amputation).

1.1.3 Balloon angioplasty and stenting

Balloon angioplasty is a well established interventional procedure to treat occluded arteries. In convential balloon angioplasty, a balloon-tipped catheter is inflated within an atherosclerotic artery to dilate the lumen and thereby improve blood flow. In a more general context, it is known as **P**ercutaneous (through the skin) **T**ransluminal (within the lumen) **A**ngioplasty (remodeling the artery). The minimally invasive character of the procedure makes it an effective and inexpensive alternative to vascular surgery. Figure 1.5 shows the successfully restored blood flow in a coronary artery where PTA has been performed.

The mechanisms of balloon angioplasty are particularly complex and have not been yet completely understood. Histological, physiological, mechanical, and clinical data consistently reveal that acute effects of balloon angioplasty include denudation of endothelium, disruption of the atherosclerotic plaque with frequent separation from or dissection of the media, overstretching of nondiseased portions of the arterial wall, and possibly extrusion of fluid from the lesion [55, 68, 180, 173]. Of these, plaque fracture and wall stretch appear to be the primary acute mechanisms.

Although PTA has a high primary success rate, the long-term success is not satisfying. This is mainly due to the re-narrowing of the vessel, called *restenosis*, which occurs in 25% to 50% of all cases [130, 154, 65]. This problem can be partially avoided by *stenting*. A stent is a wire mesh tube which is delivered to the lesion site through a catheter, and

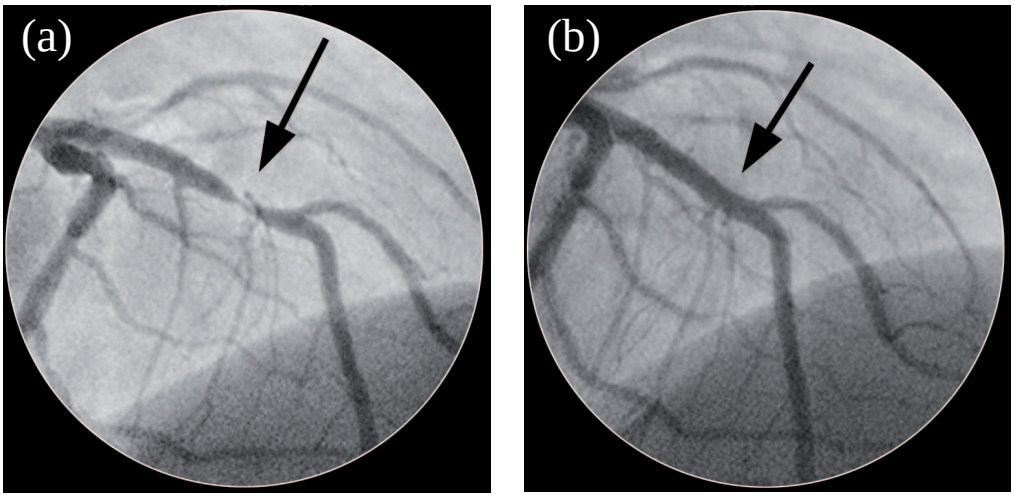

Figure 1.5: (a) Angiogram of a coronary artery demonstrating high level of occlusion; (b) post-procedural angiogram showing restoration of flow after balloon angioplasty.

is next deployed with a balloon. It acts like a scaffold which aims to keep the arterial lumen open. The stenting procedure is clearly illustrated in Figure 1.6. Several studies, among which [75], which compare classical PTA with stented PTA, clearly document that the patience rate with stenting has been significantly higher. Hence, vascular stents have gained wide popularity over the last years. There is a wide variety of stent products with different characteristics, in different stages of clinical use.

1.2 Aim of the study

1.2.1 Biomechanical modeling and computational modeling of stenting

Despite the constantly increasing success rate of stenting through technological progresses in stent design and drug coatings on the stents' surface[18], the procedure can still fail, mainly because of in-stent restenosis [50]. The focal vascular trauma imposed by the struts of the stent, the stress and strain environments around the expanded stent, and the existence of a foreign material in the injured artery may trigger inflammation, granulation and extracellular matrix production [181, 184, 153]. These processes may lead to reclosure of the blood vessel, which results in the need for further interventions.

Since balloon angioplasty and stenting is a mechanical solution to a clinical problem, one may claim that the imposed vascular injury and the resulting restenosis depend on the stent design (structure and material) and the deployment technique, and consequently on the way the medical devices interact with the lesion. There is still a need for more advanced and efficient models that incorporate the highly nonlinear behavior of the individual components

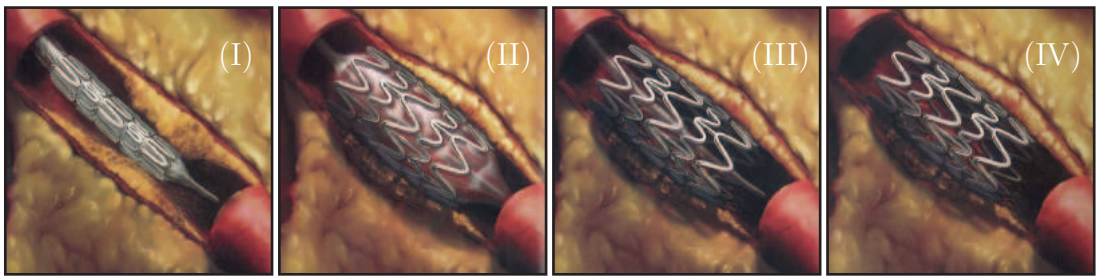

Figure 1.6: (a) Illustration of balloon angioplasty with stenting. (I) A thin stent is crimped over a balloon and threaded through the narrow segment of the plaque-filled artery, (II) pressure is used to inflate the balloon, expanding the stent, (III) the balloon is deflated and removed, while the stent is left in place, (IV) the stent provides a mechanical scaffolding, which prevents the complete blockage of the artery. Image courtesy of [164].

of the system, and the complexity of their contact interaction. Additionally, the validation of these models with pertinent experimental data is crucial.

The main motivation of the thesis is the development of an experimental and computational environment which enables the simulation of the mechanical aspects of these interventional treatments. This should serve two purposes: (i) to study and deeper understand the short-term outcome of PTA with stenting by using a particular device set for a patient-specific stenosis, and (ii) to provide a virtual test bed to choose the optimal clinical devices for a specific stenosis. More particularly, the thesis focuses on:

- the three-dimensional contact interaction of the involved medical devices (balloon catheter, stent) and the vessel wall,
- the post-angioplasty strain and stress environments, which may be correlated with restenosis,
- the redistribution of the plaque components inside the wall, during and after stenting,
- the stent design parameters and their influence on the outcome of the interventional procedure.

The arising (initial) boundary-value problems (BVPs) are (approximately) solved with the finite element method (FEM), which employs nonlinear continuum mechanics as a fundamental basis. The interaction between the artery, the balloon catheter and the stent is simulated by means of a special contact algorithm, based on smooth surface parametrizations. This addressed topic is of particular interest, since contact modeling between finite deformable bodies is still under scientific research. The approaches mentioned above have the potential to take all important nonlinearities and mechanical effects of the procedure into account.

1.2.2 Computational assessment of plaque vulnerability

Growing evidence suggests that disruption of atherosclerotic plaques and the associated formation of occlusive intraluminal thrombi is a major factor precipitating most sudden cardiac events. After numerous histopathological studies of disrupted plaques, there is widespread unanimity in the belief that a large lipid core occupying at least 50% of the overall plaque volume, and a thin plaque cap, in which the collagen structure is disorganised, are the major structural components of rupture-prone plaques [46, 47, 59, 31].

Recent technological advances in the field of medical imaging (MRI, IVUS) continue to provide increasingly better information on plaque geometry and composition, and have successfully allowed the identification of the characteristics mentioned above. However, fracture of any biological tissue depends also greatly on the imposed mechanical stresses and its innate mechanical strength [150, 5, 11]. This is supported by numerous numerical studies, among which [143, 23], where it has been shown that stress concentration sites are associated with plaque rupture locations.

Consequently, morphological criteria alone cannot fully explain and identify vulnerability. Assessment of plaque vulnerability requires detailed 3D stress analysis. This is a challenging task, since diseased arteries show a complex structure of viscous components, calcifications, and a multitude of soft tissues. The latter exhibit strongly nonlinear and anisotropic mechanical responses, and therefore, appropriate mechanical models of diseased arteries have to be established.

Based on the arguments above, one of the main objectives of this thesis is the development of a combined imaging and computational methodology, able to analyze the 3D mechanical environment of complex atherosclerotic lesions, and to identify high-risk plaques. In particular, the work aims to contribute to non-invasive determination of plaque composition by means of three-dimensional MR imaging strategies, coupled to a highly automated method for plaque segmentation and characterization. The analysis of plaque mechanics by application of the nonlinear finite element method should identify the biomechanical stresses inside the arterial tissues, and assess the rupture risk for patient-specific mechanical models. Finally, the thesis' goal is to bridge the gap between the medical and engineering community by providing clinicians with an index of vulnerability, linked to the mechanical strength and stress of the clinically important fibrous cap. Such an imaging and computational platform has the potential to serve as a tool for diagnosis, prevention and better treatment of atherosclerotic plaques.

1.3 Organization of the thesis

The thesis is a compilation of four scientific papers which fall within two main ares of interest: *cardiovascular stenting* and *plaque vulnerability*. The included publications focus mainly on the contact interaction of the medical devices (balloon catheter, stent) with the

arterial wall during stenting, and on the biomechanical environment and risk assessment of atherosclerotic lesions. In more detail:

1. D. E. KIOUSIS, T. C. GASSER & G. A. HOLZAPFEL [2008]. 'Smooth contact strategies with emphasis on the modeling of balloon angioplasty with stenting', *Int. J. Numer. Meth. Eng.*, Vol. 75, pp. 826–855.

   The paper introduces a novel contact algorithm where the target surfaces are described by polynomial expressions with C^2-continuity. Based on uniform cubic B-splines, two different parametrization techniques are presented and compared, while the related implementation of the algorithm into the multipurpose finite element program FEAP is described. Two numerical examples are selected to demonstrate the special merits of the proposed contact formulation. The first example is a benchmark 3D contact problem including large deformations and sliding. The second example is concerned with the simulation of balloon angioplasty and stenting, where contact between the balloon, the stent and the arterial wall is numerically modeled. A patient-specific 3D model of a stenotic femoral artery is considered.

2. D. E. KIOUSIS, T. C. GASSER & G. A. HOLZAPFEL [2007]. 'A numerical model to study the interaction of vascular stents with human atherosclerotic lesions', *Ann. Biomed. Eng.*, Vol. 35, pp. 1857–1869.

   A methodology is proposed that enables to predict the effect of stent design on the mechanical environment of stenotic arteries. The stress evolution in four different tissue components of a human iliac lesion, during and after stenting, is investigated. Anisotropic, highly nonlinear material models are applied to describe the behavior of tissues at finite strains. The 3D balloon-stent-artery interaction problem is numerically solved by means of the contact algorithm presented previously. In the simulations, three different stent designs are studied. The performance of each stent is characterized by scalar quantities relating to stress changes in the artery, contact forces and changes in lumen area. The study concludes by suggesting two optimal stent designs for two different clinically relevant parameters.

3. D. E. KIOUSIS, A. R. WULFF & G. A. HOLZAPFEL [2008]. 'Experimental studies and numerical analysis of the inflation and interaction of vascular balloon catheter-stent systems', *Ann. Biomed. Eng.*, in Press.

   The study experimentally investigates the mechanical characteristics of the transient expansion of six commercially available balloon-expandable stent systems. A robust finite element model based on the obtained experimental results is additionally developed. Characteristic pressure-diameter diagrams for the balloon-expandable stents and the detached balloons are obtained. Next, typical measures of clinical interest, such as the burst opening pressure, the maximum dog-boning and foreshortening, and the elastic recoil are determined. The computational model is able to successfully capture the experimentally-observed deformation mechanisms.

4. D. E. KIOUSIS, S. F. RUBINIGG, M. AUER & G. A. HOLZAPFEL [2008]. 'A methodology to analyze changes in lipid core and calcification onto fibrous cap vul-

nerability: The human atherosclerotic carotid bifurcation as an illustratory example', submitted for publication.

This work presents a computational methodology, able to accurately analyze the mechanical environment of atherosclerotic lesions and consequently to identify high-risk plaques. By means of MRI, a patient-specific, 3D geometric model of a stenotic human carotid bifurcation is obtained. The inhomogeneity of the plaque is considered, and the adopted constitutive model accounts for the nonlinear, anisotropic behavior of the arterial constituents. A novel numerical concept is implemented for the laborious computation of the local material axes in case of large 3D, arbitrarily curved, patient-specific geometries. The nonlinear finite element method is used for the analysis of lesion mechanics. The composition of the plaque is introduced as a study parameter. The proposed morpho-mechanical approach, in conjunction with medical imaging, offers a meaningful approach to assess vulnerability of atherosclerotic lesions.

The following conference contributions, in form of abstract, are also a result of the thesis.

D.E. Kiousis, G.A. HOLZAPFEL: 'Effects of tissue components on the vulnerability of atherosclerotic plaques: A computational study', *World Congress on Computational Mechanics*, Venice, Italy, 29th June - 4th July, 2008

G.A. HOLZAPFEL, **D.E. Kiousis**, M. KROON: 'On modeling multi-layered soft collagenous tissues ', *World Congress on Computational Mechanics*, Venice, Italy, 29th June - 4th July, 2008

D.E. Kiousis, G.A. HOLZAPFEL: 'Computational contact analysis of stents interacting with patient-specific stenotic arteries using smooth surface discretization', *IX International Conference on Computational Plasticity*, Barcelona, Spain, 5th - 7th September, 2007

D.E. Kiousis, T.C. GASSER, G.A. HOLZAPFEL: 'Changes in the mechanical environment of lesions due to stent-artery interaction - A computational analysis', *5th World Congress of Biomechanics*, Munich, Germany, 29th July - 4th August, 2006

G.A. HOLZAPFEL, M. AUER, **D.E. Kiousis**, T.C. GASSER: 'Fusion of imaging and computational biomechanics: A promising approach for improved analysis of the biomechanics of atherosclerotic plaques', *5th World Congress of Biomechanics*, Munich, Germany, 29th July - 4th August, 2006.

G.A. HOLZAPFEL, T.C. GASSER, **D.E. Kiousis**: 'Mechanobiology: Computation and Clinical Application', *ECCM2006 - III European Conference on Computational Mechanics*, Lisbon, Portugal, 5th - 9th June, 2006

D.E. Kiousis, T.C. GASSER, G.A. HOLZAPFEL: 'Numerical simulation of balloon angioplasty with stenting by means of a smooth contact surface representation', *1st GACM - Colloquium for Young Scientists on Computational Mechanics*, Bochum, Germany, 5th - 7th October, 2005

G.A. HOLZAPFEL, T.C. GASSER, **D.E. Kiousis**: 'Recent advances in the modeling of Balloon Angioplasty', *ICCB2005 - II International Conference on Computational Bioengineering*, Lisbon, Portugal, 14th - 16th September, 2005

G.A. HOLZAPFEL, M. AUER, F. CACHO, G. FRANCESCHINI, T.C. GASSER, **D.E. Kiousis**, G. SOMMER: 'Was kann die Ingenieurwissenschaft zur Verbesserung von therapeutischen Eingriffen an atherosklerotischen Blutgefässen beitragen?', *Workshop: Zukunft durch Forschung - Forschung heisst Zukunft gestalten. Forum Technik und Gesellschaft an der Technischen Universität Graz*, Graz, Austria, 28th November, 2003.

2 SMOOTH CONTACT STRATEGIES WITH EMPHASIS ON THE MODELING OF BALLOON ANGIOPLASTY WITH STENTING

Abstract— Critical to the simulation of balloon angioplasty is the modeling of the contact between the artery wall and the medical devices. In standard approaches, the 3D contact surfaces are described by means of C^0-continuous facet-based techniques, which may lead to numerical problems. This chapter introduces a novel contact algorithm where the target surfaces are described by polynomial expressions with C^2-continuity. Based on uniform cubic B-splines two different parametrization techniques are presented and compared, while the related implementation of the algorithm into FEAP is described. Two numerical examples are selected to demonstrate the special merits of the proposed contact formulation. The first example is a benchmark contact problem selected to point out the special features of the proposed strategies. The second example is concerned with the simulation of balloon angioplasty and stenting, where contact between the balloon, the stent and the artery wall is numerically modeled. A patient-specific 3D model of a stenotic femoral artery serves as a basis. The study concludes by identifying the changes in the mechanical environment of the artery in terms of contact forces and strains by considering two different stent designs.

Keywords— contact mechanics; smooth surfaces; B-spline; balloon angioplasty; stent

2.1 Introduction

Balloon angioplasty with or without stenting is an interventional clinical treatment aiming at the dilation of stenotic arteries in order to increase the blood flow through the artery. Its steadily growing medical, economical and scientific interest (see [177]) has motivated clinical and biomechanical communities to a considerable research effort. An increasing number of computational studies, by means of numerical tools such as the finite element method, has been noted during the last decades. Common target of all presented works is the detailed understanding of the underlying mechanisms, the optimization of the interventional protocols and finally the improvement of the clinical outcome.

Especially for the engineering community, the modeling and analysis of stent dilation in an artery turns out to be of great interest. It involves a number of challenging areas within computational mechanics such as nonlinear continuum mechanics and the development of nonlinear and anisotropic constitutive laws. However, most critical to a reliable modeling of the stenting procedure is the contact mechanics formulation. The stenting technique involves three different contact problems (balloon-stent, stent-artery, balloon-artery), and

thus a robust and stable contact algorithm should be used in order to successfully and efficiently address the problem.

For the finite element analysis of contact problems various methods are applied to incorporate the contact constraints in the variational formulation (details are provided in the textbooks [107, 186]). However, the often encountered choice of C^0-continuous descriptions for the arbitrarily curved contact interfaces may lead to numerical instabilities. These instabilities arise from the sliding of contractor nodes over target facet boundaries, where a jump of the normal vector occurs, and the assumption of smoothness is violated [67]. This discontinuity of the normal vector usually leads to rough non-physical behavior, oscillation of contact forces, numerical instabilities and loss of the quadratic convergence rate. This is especially the case when highly-curved surfaces of engineering or biological structures such as blood vessel walls are modeled. One possible remedy that addresses the mentioned problems is the use of a disproportionately fine mesh in the vicinity of the contact regions. Such an attempt could lead to high computational costs and is for this reason considered to be inefficient and is often avoided. Hence, the need for special algorithmic treatment is implied.

Towards this direction, higher-order parametrizations have recently been derived with the aim to describe one of the contact surfaces, allowing thus smooth sliding of the nodes on the contact interface. Through this approach, the discontinuities induced by spatial discretizations can be avoided and the numerical outcome can be improved. Among the most common smooth parametrizations used in conjunction with contact algorithms are the cubic Hermite interpolations [104, 136], the cubic B-splines [139], the Overhauser splines [44, 2] and NURBS [29, 161]. The more recent publication [160] makes use of a more advanced smooth parametrization, i.e. subdivision surfaces, which was first introduced in [22] and which originates from the computer aided design community. All the previously mentioned smooth discretizations have been successfully applied into a series of engineering contact problems, exploiting significant advantages over facet-based approaches [105, 161]. Therefore, the use of at least C^1-continuous interpolation schemes in the modeling of the contact-dominated stenting procedure is also appreciated. In this way, stability problems which are present in typical simulations of cardiovascular intervention (see [165]), could be avoided.

A detailed study of the literature reveals a large number of papers that attempt to model numerically the stent expansion in atherosclerotic arteries. Despite the promising scientific outcomes of these papers, the majority consider cylindrical arterial geometries [146, 9, 125, 106, 190, 174]. More refined patient-specific models are included in the papers [87, 86], while the balloon catheter and its contact with the artery wall are not modeled. This is also the case for the above cited papers. To the authors' knowledge the recent article [114] is the first that presents a finite element computation of the contact interaction between the balloon, the stent and the arterial wall. Nevertheless, a cylindrical model for the artery was used again.

The present study aims to propose an innovative 3D contact algorithm which uses C^2-continuous parametrizations for the description of the target surfaces of the involved con-

tacting bodies. In particular, two different polynomial functions are investigated. We employ the uniform cubic B-splines [118, 15, 49] that have been used previously in computer design, aerospace and in the automotive industry. Then we present a novel modification of the fourth-order B-spline polynomials, which, with no significant computational cost, manages to additionally interpolate the points of the control net. Thus, a more precise approximation of the geometric models can be achieved. The smooth contact approach is implemented into the multi-purpose finite element program FEAP [171]. The necessary implementation steps are provided in detail. The developed numerical tool is applied to a classical contact mechanics problem, often encountered in the literature [105, 141]. The example involves finite deformations and large sliding and the acquired results (in form of contact forces) point out the robustness of the contact algorithm and the features of the selected parametrizations.

As a second example we present a 3D simulation of stenting. It investigates one stenosis that is located in a human femoral artery. The geometric model of the arterial wall is obtained from high-resolution magnetic resonance imaging (hrMRI) and is re-constructed by means of NURBS [8]. The vessel is modeled as a homogeneous, isotropic material, exposing a nonlinear behavior at higher strains. Uniaxial tensile tests of femoral artery tissues are used to establish the constitutive law and the associated material parameters. A novel, cylindrically orthotropic material model is developed in order to capture the realistic behavior of the balloon catheter. To the authors' knowledge it appears that no model considers yet the three-dimensional, non-axisymmetrical geometries and contact interactions between the three continua. In addition, the approach documented here is, along with [77], one of the first attempts to employ specific contact algorithmic treatments to the demanding simulation of balloon angioplasty and stenting. The final target of the work is to predict the outcome of the treatment for two different stent configurations. More specifically, the development of mechanical strains and contact forces on the inner arterial wall during and after the expansion of the stents are studied.

2.2 Contact kinematics

A sufficient way to model contact problems involving large deformations is the finite strain approach in conjunction with the target-contractor concept. Without loss of generality, two bodies $\mathcal{B}^\alpha$, $\alpha = \mathrm{m,s}$, are considered, approaching each other during a finite deformation process and coming into contact on parts of their boundaries, denoted by Γ_c^α (see Figure 2.1). Each of the two continua occupies the bounded domain $\Omega^\alpha \subset \mathbb{R}^\zeta$, where ζ denotes the number of space dimensions of the problem. The target (or master) body is denoted by $\mathcal{B}^\mathrm{m}$, while $\mathcal{B}^\mathrm{s}$ denotes the contractor (or slave) body. The boundary Γ^α of $\mathcal{B}^\alpha$ consists of three parts $\Gamma_{\boldsymbol{\sigma}}^\alpha$, $\Gamma_{\mathbf{u}}^\alpha$ and Γ_c^α, so that $\partial\Omega^\alpha = \Gamma_{\boldsymbol{\sigma}}^\alpha \cup \Gamma_{\mathbf{u}}^\alpha \cup \Gamma_c^\alpha$, where von Neumann, Dirichlet and contact boundary conditions are prescribed, respectively. The spatial points of the current configuration are denoted by $\mathbf{x}^\alpha$. In order to specify the contact constraints, it is useful to introduce the mapping $\Psi : \mathcal{A} \to \mathbb{R}^{\zeta-1}$ so that $\mathbf{x}^\mathrm{m} = \Psi(\xi, \eta)$, where ξ and η

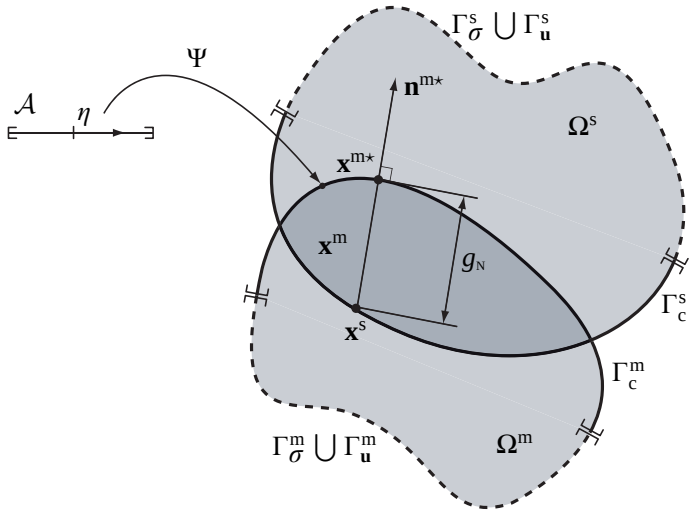

Figure 2.1: Two-dimensional representation of the deformed configuration of two contact bodies $\mathcal{B}^{\alpha}$, and definition of the closest point projection.

are the convective coordinates of the parameter plane $\mathcal{A}$. The derivation of the governing equations, discussed next, follows closely the approaches documented in [188, 108].

2.2.1 Normal contact of three-dimensional bodies

Every point $\mathbf{x}^{\mathrm{s}}$ on Γ^{s} can be associated to a point $\mathbf{x}^{\mathrm{m}\star} = \mathbf{x}^{\mathrm{m}}(\xi^{\star}, \eta^{\star})$ via the minimum distance problem

$$d(\xi, \eta) = \|\mathbf{x}^{\mathrm{s}} - \mathbf{x}^{\mathrm{m}\star}\| = \min_{\mathbf{x}^{\mathrm{m}} \subseteq \Gamma^{\mathrm{m}}_{\mathrm{c}}} \|\mathbf{x}^{\mathrm{s}} - \mathbf{x}^{\mathrm{m}}(\xi, \eta)\|. \tag{2.1}$$

The solution of (2.1), hence the target point $\mathbf{x}^{\mathrm{m}\star}$, is the orthogonal projection of the contractor point $\mathbf{x}^{\mathrm{s}}$ onto the current target surface $\Gamma^{\mathrm{m}}_{\mathrm{c}}$, as depicted in Figure 2.1. The minimum distance problem can be solved by means of a local Newton iteration algorithm of the form

$$\boldsymbol{\xi}^{\star}_{i+1} = \boldsymbol{\xi}^{\star}_{i} - \left. \frac{\dfrac{\partial d}{\partial \boldsymbol{\xi}}}{\dfrac{\partial^2 d}{\partial \boldsymbol{\xi}^2}} \right|_{\boldsymbol{\xi} = \boldsymbol{\xi}^{\star}_{i}}, \tag{2.2}$$

where the solution vector $\boldsymbol{\xi}^{\star}$ stands for the set of the convective coordinates $(\xi^{\star}, \eta^{\star})$, which is not always unique. Once the point $\mathbf{x}^{\mathrm{m}\star}$ is known, a gap function g_{N} can be defined as

$$g_{\mathrm{N}} = (\mathbf{x}^{\mathrm{s}} - \mathbf{x}^{\mathrm{m}\star}) \cdot \mathbf{n}^{\mathrm{m}\star}, \tag{2.3}$$

where $\mathbf{n}^{\mathrm{m}\star}$ is the outward unit normal on the target surface at the target point $\mathbf{x}^{m\star}$ (see Figure 2.1). The gap function g_{N} defines the state of normal contact. The conditions upon

admissibility of $\mathbf{x}^{\mathrm{s}}$ are summarized in the Karush-Kuhn-Tucker conditions

$$g_{\mathrm{N}} \geq 0, \quad t_{\mathrm{N}} \leq 0, \quad t_{\mathrm{N}}\, g_{\mathrm{N}} = 0, \tag{2.4}$$

where t_{N} is associated with the contact force $\mathbf{t}$ via $\mathbf{t} = t_{\mathrm{N}}\mathbf{n}$ for the case of frictionless contact. The three relations in (2.4) represent conditions for impenetrability, compressive normal interaction and complementarity of gap and contact pressure, respectively.

2.2.2 Variational formulation

In order to obtain solutions for the frictionless contact problem, a finite element framework is developed which treats normal contact as a unilateral constraint problem. In this case, the normal contact pressure is not computed from a constitutive equation, but can be deduced from the constraint equations. The later can be incorporated into the formulation through the virtual work contributions due to contact.

The virtual work statement for the interacting bodies is described by the relation

$$\sum_{\alpha=\mathrm{m,s}} \delta W^{\alpha}_{\mathrm{ext}} + \sum_{\alpha=\mathrm{m,s}} \delta W^{\alpha}_{\mathrm{ext,c}} = \sum_{\alpha=\mathrm{m,s}} \delta W^{\alpha}_{\mathrm{int}}. \tag{2.5}$$

The contact contribution of the two bodies to the external virtual work is

$$\sum_{\alpha=\mathrm{m,s}} \delta W^{\alpha}_{\mathrm{ext,c}} = \int_{\Gamma^{\mathrm{s}}_{\mathrm{c}}} \mathbf{t}^{\mathrm{s}} \cdot \delta\mathbf{u}^{\mathrm{s}}\, \mathrm{d}\Gamma^{\mathrm{s}}_{\mathrm{c}} + \int_{\Gamma^{\mathrm{m}}_{\mathrm{c}}} \mathbf{t}^{\mathrm{m}} \cdot \delta\mathbf{u}^{\mathrm{m}}\, \mathrm{d}\Gamma^{\mathrm{m}}_{\mathrm{c}}, \tag{2.6}$$

where $\mathbf{u}^{\alpha}$ denotes the prescribed displacement field. The balance of linear momentum implies that the differential contact force exerted on $\mathcal{B}^{\mathrm{m}}$ is equal and opposite to the force on the body $\mathcal{B}^{\mathrm{s}}$ everywhere on $\Gamma^{\alpha}_{\mathrm{c}}, \alpha = \mathrm{m,s}$; therefore, $\mathbf{t}^{\mathrm{s}} = -\mathbf{t}^{\mathrm{m}} = \mathbf{t}$. Equation (2.6) then deduces into

$$\sum_{\alpha=\mathrm{m,s}} \delta W^{\alpha}_{\mathrm{ext,c}} = \int_{\Gamma^{\mathrm{s}}_{\mathrm{c}}} \mathbf{t} \cdot \left[\delta\mathbf{u}^{\mathrm{s}} - \delta\mathbf{u}^{\mathrm{m}}(\xi,\eta)\right] \mathrm{d}\Gamma^{\mathrm{s}}_{\mathrm{c}}. \tag{2.7}$$

Since $\mathbf{t} = t_{\mathrm{N}}\,\mathbf{n}$, the expression $\mathbf{n} \cdot \left[\delta\mathbf{u}^{\mathrm{s}} - \delta\mathbf{u}^{\mathrm{m}}(\xi,\eta)\right]$ can be derived, which is equal to δg_{N}. Thus, (2.7) yields

$$\sum_{\alpha=\mathrm{m,s}} \delta W^{\alpha}_{\mathrm{ext,c}} = \int_{\Gamma^{\mathrm{s}}_{\mathrm{c}}} t_{\mathrm{N}}\, \delta g_{\mathrm{N}}\, \mathrm{d}\Gamma^{\mathrm{s}}_{\mathrm{c}}. \tag{2.8}$$

The conditions described in $(2.4)_{1,2}$ state an inequality variational principle. Therefore, a regularization technique is required. The one chosen here is the penalty method. Then, for normal contact, the Karush-Kuhn-Tucker conditions are replaced by the expression $\varepsilon_{\mathrm{N}} \langle g_{\mathrm{N}} \rangle$, where $\langle \bullet \rangle$ denotes the Macauley bracket representing the positive part of its argument and ε_{N} is the normal penalty parameter. The advantage of the penalty method (more than its simplicity) is that it evaluates the contact pressure in a displacement-driven way since it

associates the contact force only with the penetration g_N. However, it must be mentioned that the solution of the penalty method is recovered from the above formulation for $\varepsilon_N \to \infty$. Too high penalizations, though, can lead to ill-conditioning of the system of equations.

Next, to incorporate the contact contributions, as described in (3.5), into the finite element procedure, the associated residual vector $[\mathbf{f}_c]$ and the stiffness matrix $[\mathbf{K}_c]$, i.e.

$$[\mathbf{f}_c]_i = \varepsilon_N g_N \left(\frac{\partial g_N}{\partial [\mathbf{u}]_i} \right), \quad [\mathbf{K}_c]_{ij} = \varepsilon_N \frac{\partial}{\partial [\mathbf{u}]_j} \left(g_N \frac{\partial g_N}{\partial [\mathbf{u}]_i} \right), \tag{2.9}$$

have to be evaluated for $i, j = 1, \ldots, w$, respectively, where w is the total number of the involved nodes (contractor node and the nodes of the target surface). For example, in the 3D case of spatial discretizations, $w = 5$, while when a smooth target surfaces is considered, defined by a control polyhedron consisting of $r \times r$ target nodes, the total number of nodes of the contact partners is $w = (r^2 + 1)$. The derivation of the matrix formulae described in Equations (2.9) are presented in detail in Section 2.4.3.

2.3 Smooth surface discretizations for contact problems

As mentioned in Section 2.1, the observed non-continuity of the normal vector due to spatial discretizations of the master contact surface may lead to numerical instabilities. A solution that addresses efficiently the problem is the approximation of the contact surfaces by means of higher-order parametrizations. In this section, two C^2-continuous functions are discussed. The first employed parametrization is the uniform cubic B-splines. The second parametrization is a new technique, developed in the context of the present work. It is based on B-splines but provides a closer approximation of the contacting bodies' geometry.

2.3.1 Cubic B-spline surfaces

B-splines have been extensively used in the aerospace and automotive industries during the last 30 years and they are a powerful tool for the design of free form curves or surfaces [118, 15, 49]. In particular, uniform cubic B-spline surfaces (spline order $n = 4$) are defined over a bidirectional net of 16 control points $\mathbf{P}_{i,j}, i, j = 1 \ldots 4$, which may be characterized by the tensor product

$$\mathbf{S}(u,v) = \sum_{i=1}^{4} \sum_{j=1}^{4} B_i(u) B_j(v) \mathbf{P}_{i,j}, \qquad 0 \le u, v \le 1, \tag{2.10}$$

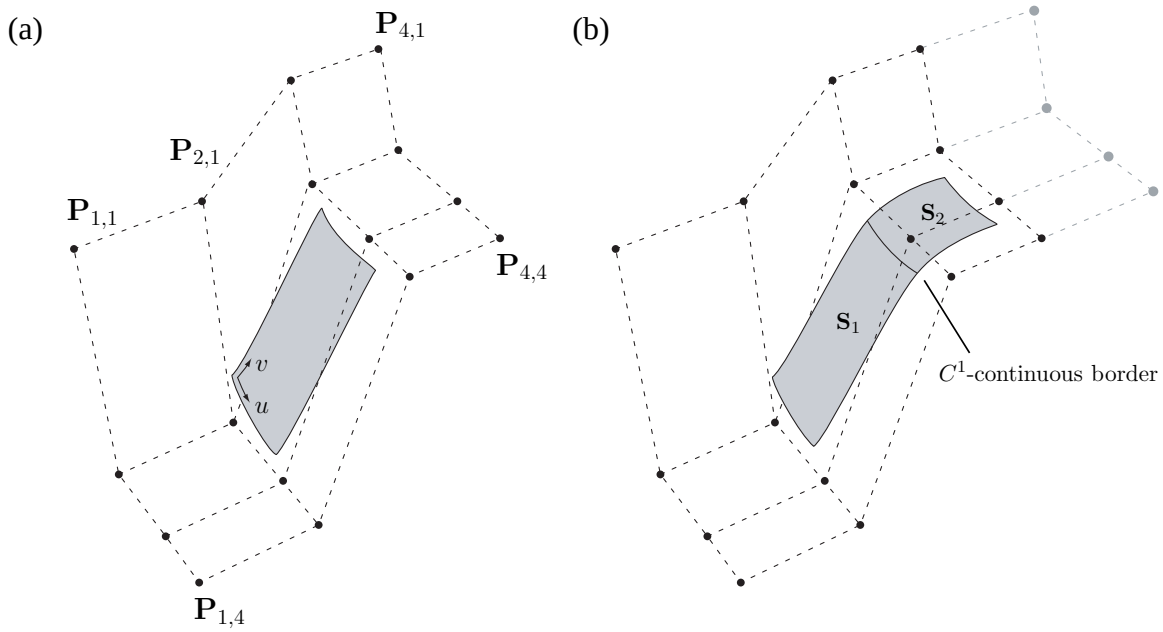

Figure 2.2: Uniform cubic B-spline surfaces: (a) 4×4 control mesh and its corresponding uniform cubic B-spline surface; (b) example of two overlapping control grids and two adjacent cubic B-spline surfaces, where C^1-continuity property of the surfaces is pointed out.

where $B_i(t), i = 1 \ldots 4$ are the cubic basis functions

$$\begin{aligned} B_1(t) &= 1/6 \quad (1 - 3t + 3t^2 - t^3), \\ B_2(t) &= 1/6 \quad (4 - 6t^2 + 3t^3), \\ B_3(t) &= 1/6 \quad (1 + 3t + 3t^2 - 3t^3), \\ B_4(t) &= 1/6 \quad t^3, \end{aligned} \tag{2.11}$$

and t stands for either the parameter u or v.

Figure 2.2(a) shows an example of a 4×4 control mesh and its corresponding uniform cubic B-spline surface $\mathbf{S}$, computed and plotted in MATHEMATICA [185]. In Figure 2.2(b) two overlapping control polyhedrons and two adjacent uniform cubic B-spline surfaces ($\mathbf{S}_1$ and $\mathbf{S}_2$) are shown. In the same figure, the C^1-continuous border between the two surfaces is also graphically represented.

Among the main properties of cubic B-splines, two are of particular interest for contact algorithms. Cubic B-splines have *second degree (C^2-) continuity*, meaning that $\mathbf{S}$ (Equation (2.10)) is twice continuously differentiable. This, as mentioned in [161], is a necessary requirement for quadratic rate of convergence within nonlinear solution schemes. Due to the higher order continuity of B-splines, the normal vector on the surface is uniquely and continuously defined. Furthermore, B-splines offer *local support* which enables the definition of a region of influence for a particular control point on the surface.

2.3.2 Modified uniform cubic B-spline surfaces

Besides the useful properties of B-splines, one inherent disadvantage of the parametrization is that it cannot represent surfaces with arbitrary mesh topology, being thus restricted to surfaces described by quadrilateral structured meshes. This problem can be overcome through several approaches such as Gregory patches [140], subdivision schemes [22] or other polynomial expressions [6, 72] (these techniques are not addressed here though). In addition, B-spline surfaces do not necessarily interpolate any of their control points (refer to the literature cited previously). This is clearly depicted in the Figures 2.2(a),(b). During the last years, several methods (based mainly on splines) have been developed in order to model biological structures more effectively and more smoothly (for example, joints and femurs). Among the most promising works are [6, 121, 37], where polynomial functions are fitted to random surface points. These approaches remove the need for structured control meshes and provide sufficient and more accurate smoothing of the surface data.

With this in mind a new parametrization is proposed here. It is based on the uniform cubic B-splines (Equation (2.10)), enhanced by one more polynomial function in order to interpolate the four central vertices of the control grid. The mathematical expression of this new parametrization, which we subsequently call *modified* uniform cubic B-splines, and denote by $\mathbf{S}'$, is

$$\mathbf{S}'(u,v) = \sum_{i=1}^{4}\sum_{j=1}^{4} B_i(u)B_j(v)\mathbf{P}_{i,j} + \sum_{i=1}^{4} N_i(u,v)\mathbf{U}_i, \qquad 0 \le u,v \le 1. \tag{2.12}$$

The term $\sum_{i=1}^{4} N_i(u,v)\mathbf{U}_i$ in (2.12) is the sum of the product of a set of basis functions $N_i(u,v)$, $i = 1,\ldots,4$, based on the trigonometric functions, and defined as

$$\begin{aligned} N_1(u,v) &= 1/4 \quad (1+\cos(\pi u))(1+\cos(\pi v)),\\ N_2(u,v) &= 1/4 \quad (1-\cos(\pi u))(1+\cos(\pi v)),\\ N_3(u,v) &= 1/4 \quad (1-\cos(\pi u))(1-\cos(\pi v)),\\ N_4(u,v) &= 1/4 \quad (1+\cos(\pi u))(1-\cos(\pi v)), \end{aligned} \tag{2.13}$$

with the displacement vectors $\mathbf{U}_i$, $i = 1,\ldots,4$. An example of the modified cubic B-splines is presented in Figure 2.3(a), in which it can be seen that the new surface $\mathbf{S}'$ interpolates the four inner points of its control mesh. In the same figure, the 'original' cubic B-spline surface is plotted and the definition of the displacement vector $\mathbf{U}_3$ is shown. In more detail, the displacement vectors are given as the distance between the edges of the uniform cubic B-spline surface and the (inner) four corresponding control points according to

$$\begin{aligned} \mathbf{U}_1 &= \mathbf{P}_{2,2} - \mathbf{S}(0,0),\\ \mathbf{U}_2 &= \mathbf{P}_{2,3} - \mathbf{S}(1,0),\\ \mathbf{U}_3 &= \mathbf{P}_{3,3} - \mathbf{S}(1,1),\\ \mathbf{U}_4 &= \mathbf{P}_{3,2} - \mathbf{S}(0,1). \end{aligned} \tag{2.14}$$

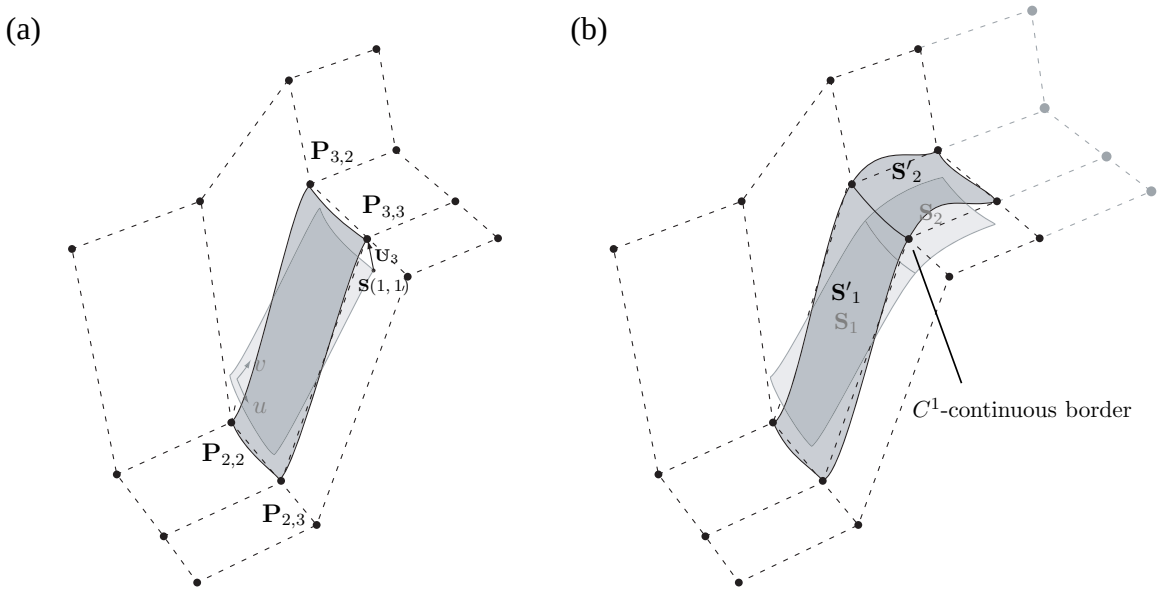

Figure 2.3: Modified uniform cubic B-splines: (a) 4×4 control mesh, the 'original' uniform cubic B-spline surface $\mathbf{S}$, and its modification $\mathbf{S}'$ that passes through the four inner nodes of the control polyhedron. The definition of the displacement vector $\mathbf{U}_3$ is also shown; (b) two adjacent 'original' uniform cubic B-spline surfaces $\mathbf{S}_1$ and $\mathbf{S}_2$, and the generated modified surfaces $\mathbf{S'}_1$ and $\mathbf{S'}_2$.

A similar approach to the one proposed here is given in [72] where a parametric polynomial and the Fourier series functions are superimposed to form a new parametrization technique. Through this method, the authors claim smoother results for the swine femoral surface, when compared to B-splines alone. Additionally, the superposition of the two functions does not tend to smoothen localized undulations and can model complex surfaces with ripples.

As can be seen the newly introduced part of relation (2.12) is infinitely continuously differentiable due to the trigonometric nature of the basis functions $N_i(u,v)$, $i = 1,\ldots,4$, i.e. Equation (2.13). Therefore, the modified expression of the uniform cubic B-spline surfaces retains the property of the C^2-continuity and the continuous definition of the normal vector along them. In addition, the basis functions N have the properties of nonnegativity, partition of unity and local support but the modified cubic B-spline surfaces do not have the geometric characteristic of the strong convex hull property.

In Figure 2.3(b) the C^1-continuous border between two adjacent modified uniform cubic B-spline surfaces ($\mathbf{S'}_1$ and $\mathbf{S'}_2$) is pointed out. The same figure indicates also that even though one modified surface passes through only four nodes of the control mesh, the consideration of overlapping control polyhedrons leads to the interpolation of all points, hence, of all superficial nodes of a finite element mesh.

One of the advantages of the parametrization described in Equation (2.12) is its simplicity.

No fitting is required and thus no additional linear systems have to be solved, as in other approaches [6, 121, 37]. In complex 3D contact problems computational cost is an important aspect that should be by all means taken into consideration. The modified cubic B-splines are to this extent a faster and more straightforward parametrization tool, able to accurately interpolate the nodes of the control grid. A closer observation of Figure 2.3 (and Figure 2.8 given later) shows, however, one drawback of the new parametrization. When abrupt curvature changes take place within short distances, the parametrization leads to local waviness. This behavior derives from the requirement of the surface to pass through the control net. That is not usually the case for the more thorough approaches cited above. On the other hand, however, the number of oscillations should be limited since the C^2-continuous surface is not required to fit a large amount of scarcely positioned image data points, but a comparatively smaller and smoother set of finite element nodes. One should also note, that it is this property which, at the same time, allows modified B-splines to represent surfaces with possible undulations or ripples. The features of the new parametrization technique are further discussed in Section 2.5.1.

2.4 Implementation strategies

One of the most demanding and at the same time most challenging task of the present work is the incorporation of the smooth parametrization techniques into a finite element framework. For the development of a contact algorithm based on smooth parametrizations the following four major points should be taken into consideration:

(i) the evaluation of the interpolation functions, and consequently of the smooth target contact surfaces,

(ii) the identification of the contact pairs,

(iii) the calculation of the contact contributions,

(iv) the assembling of the contact elements' residuum and stiffness into the global residuum vector and stiffness matrix.

The open-source program FEAP [171] provides the possibility for the implementation of such a numerical scheme and it is, therefore, chosen as the basis of the developed contact algorithm. The additional needs are met by a series of subroutines, forming the user contact driver **SmooC** (standing for *Smooth Contact*), which communicates with FEAP through user-defined macro commands. All implementation steps are discussed in the section that follows.

2.4.1 Implementation of the smooth interpolation schemes

As already mentioned in Section 2.3, each uniform cubic (and modified) B-spline surface is defined by a structured mesh of control points, $\mathbf{P}_{i,j}$, $i, j = 1, \ldots, 4$, see Equations (2.10)

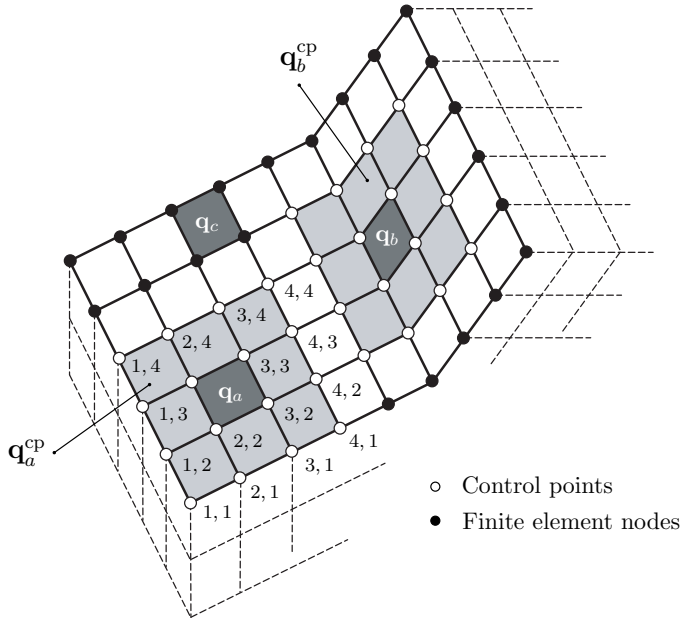

Figure 2.4: Discretized arbitrary master contact body: the control polyhedrons that define the smooth interpolations of two different master contact facets ($\mathbf{q}_a$, $\mathbf{q}_b$) are shown.

and (2.12). Thus, the evaluation of the smooth surface $\mathbf{S}_k$ associated with a specific facet $\mathbf{q}_\kappa$ of the discretized target contact surfaces requires initially the definition of a 4×4 control polyhedron. In the context of the present work, each control grid is formed by the nodes of the considered facet $\mathbf{q}_\kappa$, as well as the nodes of its neighbor facets that are located on the contact surface, as in the two examples of facets $\mathbf{q}_a$ and $\mathbf{q}_b$ shown in Figure 2.4. This is a significant advantage of the proposed approach since it allows to base the geometrical modeling and the finite element analysis on an identical representation paradigm. Such a unified framework yields a robust interface between geometric design and mechanical analysis, as discussed in [95, 26]. The structured control patch consists of 16 nodes for each contact facet, subsequently denoted by $\mathbf{q}_\kappa^{\mathrm{cp}}$. This ingredient, hence the control polyhedron for each facet of the master surfaces, is provided by **SmooC**, and more specifically by the macro **CPoin**, executed before the beginning of the computation. The macro reads the mesh coordinates and connectivity list, identifies the adjacent facets of each facet $\mathbf{q}_\kappa$ belonging to the target surfaces, and generates the structured, control point patches $\mathbf{q}_\kappa^{\mathrm{cp}}$.

After acquiring the control polyhedrons $\mathbf{q}^{\mathrm{cp}}$, the parametrization of every contact facet by the interpolation functions, described in Equations (2.10) and (2.12), is straightforward. The smooth surface $\mathbf{S}_\kappa(u,v)$ for each facet is computed by a self-programmed MATHEMATICA-generated function, called by the macro **MSurf**. The required inputs of **MSurf** are the obtained control polyhedrons $\mathbf{q}^{\mathrm{cp}}$, as well as the contractor nodes $\mathbf{x}^{\mathrm{s}}$. The same macro performs a series of further operations, defined by an index, which are discussed in the following paragraphs.

2.4.2 Contact search

The algorithms for detecting contact are of utmost importance since the time for the definition of the possible contact bodies and contact pairs could dominate the overall cost of the numerical simulation. Therefore, even though search algorithms are not the main focus here, an attempt is made to tackle the search problem by means of refined and time-efficient methods.

In the present work, no global search is taken into consideration. The possible contact bodies are predefined, and hence considered as an input of the contact problem. In other words, only local search algorithms are addressed, where two bodies are in contact but it is not clear which contractor node contacts which target segment. There are several possibilities to deal with this problem. The approach followed here splits the detection of local contact for a given contractor node $\mathbf{x}^{\mathrm{s}}$ into two different phases.

Initially, the set of the closest target facets $\mathbf{q}_\kappa$ for the contractor node $\mathbf{x}^{\mathrm{s}}$ is identified. This can be performed by defining a search radius r_{search}, which is related to the problem and highly dependent on the discretization size of the target contact surfaces. In the case that $\|\mathbf{x}^{\mathrm{s}} - \mathbf{x}^{\mathrm{m}}_{\kappa,\mathrm{mid}}\| \leq r_{\mathrm{search}}$, where $\mathbf{x}^{\mathrm{m}}_{\kappa,\mathrm{mid}}$ is the middle point of the facet $\mathbf{q}_\kappa$, the target facet $\mathbf{q}_\kappa$ is considered as a part of the set mentioned above. The purpose of this step is to limit the number of contact search iterations, and consequently their computational time.

In a second step, the parametrization of the closest target facets is carried out by application of (2.10) or (2.12), and the minimum distance problem (depicted in (2.1)) is solved, and the smooth surface $\mathbf{S}^\star_\kappa$ which contains the orthogonal projection $\mathbf{x}^{\mathrm{m}\star}$ is obtained. The first part of this step is local in nature and for this reason not computationally expensive, while the minimum distance problem does not have a closed form solution. Therefore, a Newton algorithm has to be applied, see (2.2). In order to further limit the computational time, a better initialization of the Newton algorithm is required. This is achieved by generating an equally divided mesh of the smooth surface, and by considering the mesh point which is closer to the contractor node $\mathbf{x}^{\mathrm{s}}$ as an initial guess of the iteration procedure. The evaluation of $\mathbf{x}^{\mathrm{m}\star}$ is followed by the computation of the gap function g_{N}. If the Karush-Kuhn-Tucker conditions are violated, i.e. Equation (2.4), then the pair $\mathbf{x}^{\mathrm{s}} - \mathbf{S}^\star_\kappa$ is considered as in contact. All the above operations are performed by the macro **MSurf**, introduced previously.

2.4.3 Evaluation and assembling of the contact contributions

The next step after the definition of the contact pairs is the computation of the virtual work contributions due to contact, and more specifically, of the associated contact residual vector $[\mathbf{f}_{\mathrm{C}}]$ and the stiffness matrix $[\mathbf{K}_{\mathrm{C}}]$.

As can be seen from (2.9), both the contact residuum and the stiffness depend on the gap function g_{N} and on its derivative with respect to the displacements of the associated contractor point and target contact surface. In the approach presented here, the two derivations are carried out on an abstract mathematical level, by making use of the MATHEMATICA

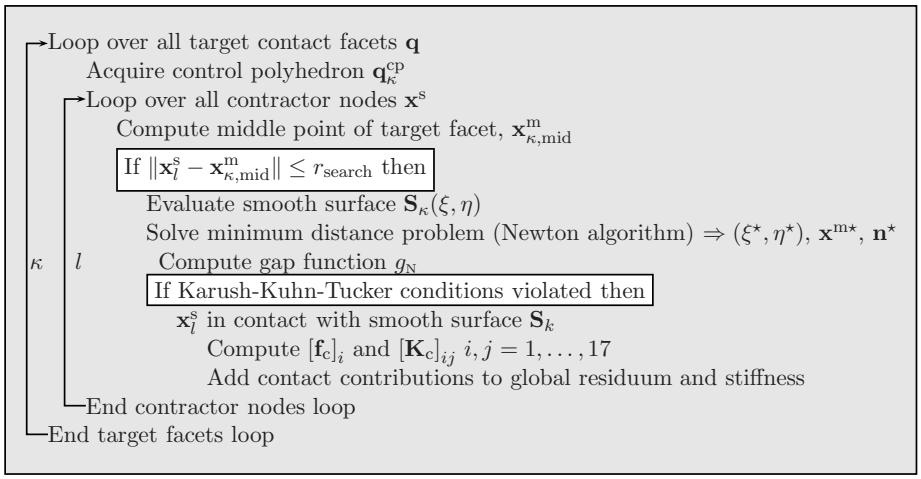

Figure 2.5: Implementation steps for computing and assembling contact contributions to the residuum and stiffness of an element.

package ACEGEN, [102]. The same method for contact problems is also applied and documented in the References [161, 160].

ACEGEN combines several techniques such as the symbolic capabilities of MATHEMATICA, automatic differentiation, simultaneous optimization of expressions and stochastic evaluation of formulas instead of conventional pattern matching method. The above provides an efficient evaluation method of the nonlinear contact quantities that requires less effort compared to manually written codes. The derived symbolic formulae for the expressions (2.9) are computed with MATHEMATICA and translated into an efficient compiled language (Fortran), and the generated subroutine is implemented into FEAP. The call of this subroutine and the computation of the contact residuum and stiffness are the last functions of the macro command **MSurf**.

When the two described techniques are used for the parametrization of the contact surfaces, the involved nodes in each contact pair are the 4×4 control points-finite element nodes $\mathbf{q}_\kappa^{\mathrm{cp}}$ of the smooth target surface and the contractor point $\mathbf{x}^{\mathrm{s}}_l$. Therefore, the total degrees of freedom and number of contact contributions for each contact pair are equal to $3(4^2 + 1) = 51$. The obtained results of (2.9) have to be added to the residuum and the stiffness of the global nonlinear system of equations. This operation is performed by the already existing FEAP subroutines **MODPROF** and **CONSTASS**. The first modifies the profile of the residuum and the stiffness by taking into consideration the 51 inputs mentioned above, while the second performs the assembling of the residuum vector and the stiffness matrix.

For a better overview, the implementation steps and the flowchart of the developed contact algorithm are summarized in the Figures 2.5 and 2.6, respectively.

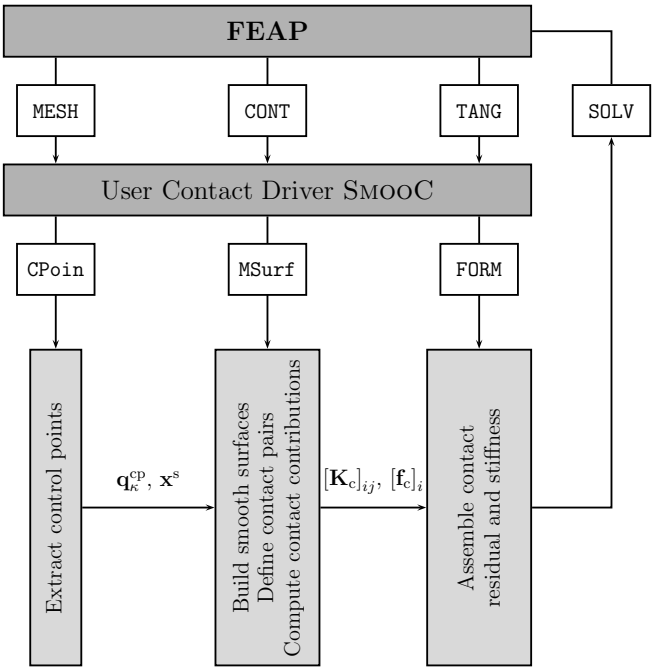

Figure 2.6: Flowchart of the implementation of the contact algorithm based on C^2-continuous surfaces into the multi-purpose finite element analysis program FEAP [171].

2.5 Numerical examples

The features and special merits of the proposed parametrization techniques and of the presented contact approach are demonstrated by the means of two numerical examples. Their main aim is to exhibit the numerical robustness of the proposed contact scheme and its ability to numerically treat complex 3D contact problems. Both examples consider contact interactions between incompressible and finite deformable bodies. In the first example contact between a brick and a plate is modeled. It is a challenging problem since large sliding is involved. The distribution of the contact forces along the path of the brick is analyzed for the two surface discretizations. The second example is concerned with the numerical simulation of balloon angioplasty with stenting, which, in the field of biomechanics, is a research area of its own. The contact interaction between three different bodies (arterial wall, balloon and stent) is modeled while a patient-specific 3D geometry of a femoral artery is taken into consideration. The induced contact forces and strains in the arterial wall are discussed in detail.

2.5.1 Brick sliding across a plate

The 3D problem consists of an orthogonal plate and a cubic brick. The dimensions of the plate are $10\,\mathrm{mm}\times 20\,\mathrm{mm}\times 3\,\mathrm{mm}$ and the brick's edges have a length of $2\,\mathrm{mm}$. The contact

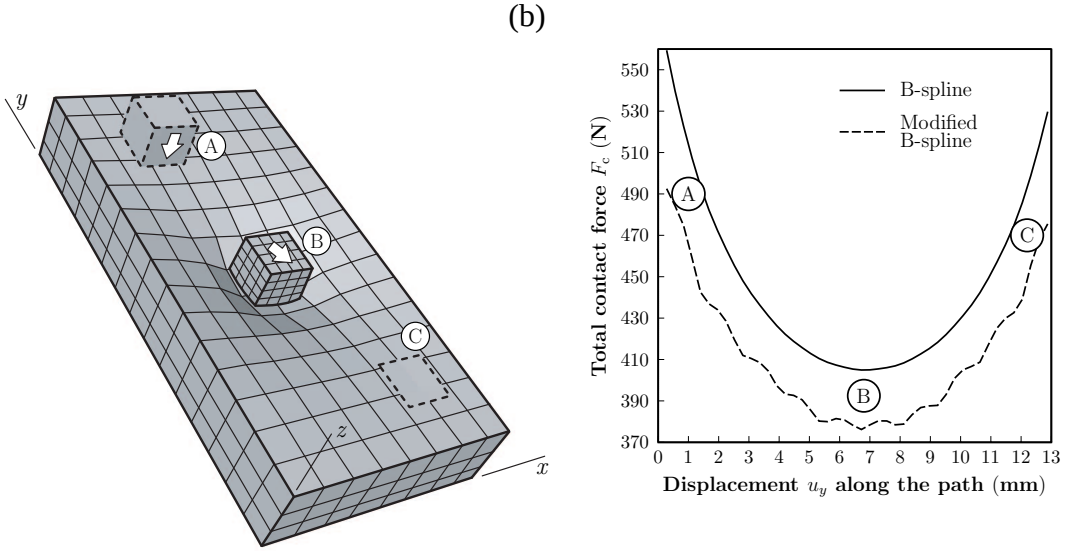

Figure 2.7: Cubic brick sliding across an orthogonal plate: (a) geometry and finite element mesh of the contacting bodies. Initially the brick is pressed downwards until it reaches the plate's midplane Ⓐ, and then it is dragged diagonally over the plate's upper surface Ⓑ until its final position Ⓒ; (b) distribution of the total contact force along the path of the cubic contractor, computed with the different smooth parametrizations of the target contact surface.

interaction of the two bodies is depicted in Figure 2.7(a) and involves the two steps: (i) the brick is pressed vertically against the plate until it reaches the plate's midplane; (ii) the brick is dragged diagonally along the plate's upper surface.

The material of both bodies is hyperelastic, nearly incompressible and described by the neo-Hookean strain-energy function

$$\Psi = \left(\frac{\kappa}{4} - \frac{\mu}{6}\right)(J^2 - 1 - 2\ln J) + \frac{\mu}{2}(\bar{I}_1 - 3). \tag{2.15}$$

The plate is characterized by a bulk modulus of $\kappa = 1.66 \cdot 10^3\,\mathrm{N/mm^2}$ and a shear modulus of $\mu = 34\,\mathrm{N/mm^2}$, while the brick is characterized by a bulk modulus $\kappa = 1.66 \cdot 10^4\,\mathrm{N/mm^2}$ and a shear modulus of $\mu = 340\,\mathrm{N/mm^2}$. In (2.15), $\bar{I}_1 = \mathrm{tr}\overline{\mathbf{C}}$ is the first invariant of the modified right Cauchy-Green tensor $\overline{\mathbf{C}} = \overline{\mathbf{F}}^T\overline{\mathbf{F}}$, where $\overline{\mathbf{F}} = J^{-1/3}\mathbf{F}$ is the modified deformation gradient with $J = \det\mathbf{F} > 0$ and $\det\overline{\mathbf{F}} = 1$, see [76].

For the discretization of both bodies relatively coarse meshes are used in order to point out the differences between the used surface parametrizations. More specifically, the finite element computation uses 424 hexahedral elements and 701 nodes, each one has three degrees of freedom. The four peripheral faces of the plate are considered bounded in all three directions. Both loading conditions (pressing and sliding) are applied by means of prescribed displacements on the brick's upper surface and the complete loading history is applied in 360 time steps (i.e. 360 prescribed displacements).

The upper face of the plate is considered as the target surface, while the nodes on the lower face of the brick are the contractor nodes. The target contact surface is discretized by means of the three discussed parametrizations, i.e. (i) planar elements, (ii) uniform cubic B-spline surfaces, and (iii) modified uniform cubic B-spline surfaces. The value $\varepsilon_{\mathrm{N}} = 4500\,\mathrm{N/mm}$ is chosen as the normal penalty parameter and no friction is considered.

The computation is initially performed by making use of the pre-existing FEAP contact scheme that is based on planar elements. In this case loss of convergence is experienced at the very beginning of the load path Ⓐ-Ⓑ (see Figure 2.7(a)) and no solution is obtained. As it seems, the main cause of this behavior is that the normal vector jumps when the slave nodes slide over the master elements. This is not the case when the target surface is described by means of the two smooth parametrizations and the developed contact algorithm is used. Then, the nonlinear solution scheme converges quadratically and a solution is always achieved.

The contact forces generated during the loading procedure are of special interest since they provide an insight on the contact interaction of the involved bodies and on the used parametrizations of the master contact surface. In Figure 2.7(b), the contact forces induced on the brick during sliding are plotted with respect to its *y*-displacements (as indicated in Figure 2.7(a)). The contact forces are obtained as the sum of all reaction forces on the brick where displacements are applied, while the different curves refer to the different parametrization techniques. The form of the two curves (minimum value in the middle of the path and maximum values at both ends) is dictated by the applied boundary conditions of the plate.

The results, as illustrated in Figure 2.7(b), reveal that when the uniform cubic B-splines are employed the contact forces develop smoothly along the path of the contractor. In the case of the modified B-splines, the contact force curve contains oscillations. Nevertheless, the curve remains smooth and no convergence problems are noted. Moreover, the obtained results are smoother when compared to the highly varying results computed with piecewise planar descriptions [105, 160]. The reason for the waviness in the force-displacement curve was already discussed in Section 2.3, and it is again depicted in Figure 2.8. The requirement of the surface to interpolate the nodes of the finite element mesh, hence its control points, leads to small waves in areas of abrupt curvature changes within short distances (middle segments of the mesh shown in Figure 2.8). However, in all other regions the C^2-continuous surface remains sufficiently smooth. Finally, the difference in the obtained results in the case of the normal B-splines and the modified B-splines derives from the difference in the surfaces' expressions and the resulting difference in the computed gap function g_{N} (see Figure 2.3(b)).

2.5.2 Numerical simulation of balloon angioplasty with stenting

In the following section, a finite element model for balloon angioplasty with stenting is presented. The model is used to simulate the contact interaction between the three involved

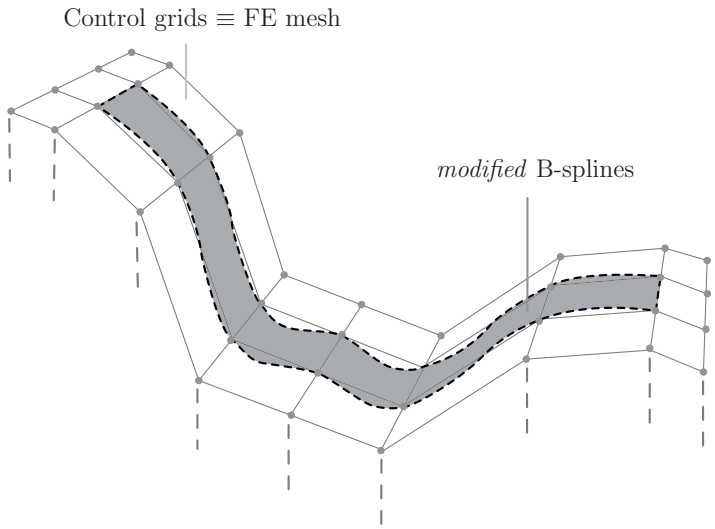

Figure 2.8: Part of the deformed finite element mesh (shown in Figure 2.7) where the contractor cube is in contact with the target plate. The modified cubic B-spline surfaces, that are used for the contact surface's description, are shown. The parametrization accurately interpolates the nodes of the discretized model. However, small waves are noted for abrupt curvature changes within short distances (see the middle section).

deformable bodies, i.e. the artery and the medical devices (balloon and stent). In the first paragraphs, the geometric and constitutive models for the three bodies are described in detail. Then, the different aspects of the simulation are given such as the used techniques, the loading procedure, the chosen boundary conditions and the generated computational mesh. Finally, the most important results of the 3D nonlinear analysis are presented. The scope of this example is to exploit the ability of the developed numerical tool to treat more complex contact problems but also to provide an insight into the interventional treatment and on the related changes in the mechanical environment of the arterial wall.

Arterial model

A realistic (patient-specific) 3D geometric model of an atherosclerotic femoral artery is considered. This, as pointed out in Section 2.1, is in contrast to the vast majority of documented numerical simulations of balloon angioplasty, in which simplified cylindrical arterial models are studied. Appropriate morphological models that represent the 3D boundary surface of diseased arterial wall are pre-requisites for a meaningful computation of strain distributions under various loading conditions and are, therefore, of significant importance. The generation of the 3D artery model is based on high-resolution MRI and NURBS surface parametrizations. A detailed description of the imaging acquisition method is documented in [8]. The reconstructed model is shown in Figure 2.9(a).

Regardless of the type, all arteries consist of three layers (intima, media, adventitia) with

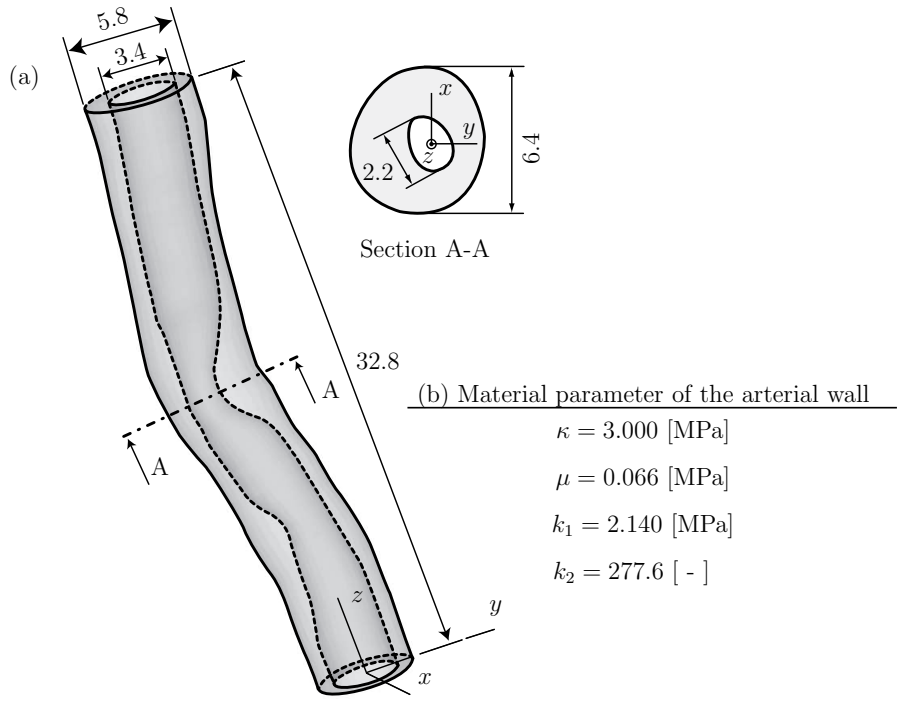

Figure 2.9: (a) Three-dimensional geometric model of a highly atherosclerotic femoral artery re-constructed on the basis of hrMRI (dimensions in mm). The table summarizes the artery's material parameters determined through data fitting of uniaxial extension tests performed on arterial strips that are cut out from the circumferential and the axial directions of 11 human femoral arteries (b).

different mechanical properties [142, 84, 77]. In addition, in the case of atherosclerosis, the formed plaque adds an extra degree of heterogeneity since it exhibits a different behavior compared to the non-diseased vessel wall [28, 83, 85]. Nevertheless, in a first attempt, the artery is modeled as a homogeneous material. This simplification does not affect in any way the study of the contact interactions and restricts only the biological interpretation of the results.

Arterial walls are highly anisotropic due to the organized arrangement of the load carrying (collagen fibrils) components [27]. However, there are many isotropic strain-energy functions used in practice to characterize the mechanical response of the arterial walls. The one chosen for this example is a rubber-like potential, similar to the one documented in [35]. This model is able to describe the typical stiffening effect of arteries in the high pressure domain. The decoupled form of the strain-energy function Ψ is

$$\Psi = U(J) + \overline{\Psi}(\bar{I}_1), \tag{2.16}$$

where U is a purely volumetric contribution and $\overline{\Psi}$ is a purely isochoric contribution to the strain energy. For the volumetric part the strictly convex function $U = \kappa(J-1)^2/2$ is considered, where κ is the bulk modulus and $J = \det\mathbf{F} > 0$ is the local volume ratio.

The bulk modulus κ serves as a user-specified penalty parameter chosen from numerical experiments so that the requirement of incompressibility ($J = 1$) is satisfied. The isochoric part $\overline{\Psi}$ of the strain-energy function Ψ is

$$\overline{\Psi} = \frac{\mu}{2}(\overline{I}_1 - 3) + \frac{k_1}{2k_2}\left\{\exp\left[k_2(\overline{I}_1 - 3)^2\right] - 1\right\}, \tag{2.17}$$

where $\mu > 0$ and $k_1 > 0$ are material parameters with the dimensions of stress, k_2 is a dimensionless parameter, and $\overline{I}_1$ is the first invariant of $\overline{\mathbf{C}}$, as introduced in previous example.

The passive, quasi-static stretch-stress response of the femoral artery, and consequently the material parameters mentioned above, are determined through mechanical tests, performed on a computer-controlled, high precision tensile machine. The procedure is documented in, for example, [85]. Briefly, uniaxial tests are performed on axial and circumferential strips extracted from the three layers (adventitia, media, intima) of 11 femoral arteries, which have undergone *in vitro* balloon angioplasty. All tissue samples are stretched far beyond the physiological loading domain up to failure in order to capture the range of deformations induced by the stent. The above constitutive model is fitted to the (averaged) behavior of all three layers in both artery directions. A least-square fitting algorithm provides the values for the three parameters, which are summarized in Figure 2.9(b).

Stent model

In the presented simulation one type of stent design is investigated. It is based on the previously commercially available Palmaz-Schatz™ (Johnson & Johnson) balloon-expandable stent. The chosen stent geometry is traced from photographs and in its undeformed configuration it resembles a tube with rectangular slots (see Figure 2.10(a)).

The 3D computer model of the stent is generated by means of a parametrization algorithm. The developed technique is able to describe the stent's overall dimensions as well as the geometry of its cells. In addition, the design parameters of the algorithm are: stent length, unexpanded diameter, number of its cells in the axial and circumferential directions, thickness of strut which is considered to have a cylindrical cross section. The algorithm can provide the finite element mesh for the parametrized stent. The advantage of such a method is the automated and fast generation of different stent designs. A systematic parametric study (as the one presented in [86]) could lead to optimal, patient-tailored stent designs. In the present study two stent designs are investigated. Their geometrical models are identical, but the thickness of their struts differ. The chosen stent parameters are summarized in Figure 2.10(b).

The material of the stents is considered to be of stainless steel. For the elastic domain of the material, a neo-Hookean model is used, while its inelastic constitutive response is described through a von Mises-Hill plasticity model with linear isotropic hardening. The Young's modulus is chosen to be $E = 2.01 \cdot 10^5\,\mathrm{N/mm^2}$ and the Poisson's ratio is $\nu = 0.3$.

(a)

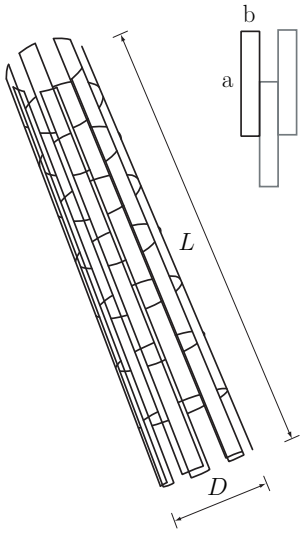

(b)

Stent design and discretization parameters	
Length L	10 mm
Diameter D	2 mm
Number of axial cells	4
Number of circumferential cells	7
Strut thickness	0.1 mm, 0.05 mm
Nodes on strut a	24
Nodes on strut b	3

Figure 2.10: Model of a Palmaz-Schatz™ balloon-expandable stent: (a) undeformed configuration of the stent; (b) design and discretization parameters used for the automatic generation of the geometry and computational mesh of the stent.

The parameters $\sigma_y = 3.0 \cdot 10^2\,\mathrm{N/mm^2}$ and $H_{\mathrm{iso}} = 2.0 \cdot 10^3\,\mathrm{N/mm^2}$ are selected for the yield stress and the hardening modulus, respectively.

Balloon model

We consider a Grüntzig-type balloon catheter [69]. This specific type is widely used in clinical practice and therefore selected. The reference configuration of the balloon is modeled as a cylindrical tube with external diameter $D_{\mathrm{e}} = 2.0\,\mathrm{mm}$, wall thickness $H = 0.2\,\mathrm{mm}$, and length $L = 12.0\,\mathrm{mm}$, as shown in Figure 2.11(a).

The dilation of this type of balloon catheters is characterized by complex kinematics, where the unfolding process of the balloon is followed by a typically nonlinear, stiffening behavior at a higher pressure level. In the present simulation, the complex unfolding process of the balloon is neglected, while a cylindrically orthotropic model is developed in order to describe the overall mechanical behavior of the balloon. This material model is described below and is based on a fiber-reinforced material, as used in [80].

Two material axes are introduced, which are oriented in circumferential and longitudinal directions. The matrix material of the balloon catheter is considered as a (soft) isotropic material. The balloon in the circumferential direction is assumed to be very soft at its initial configuration and particularly stiff after a predefined stretch limit, while in the longitudinal direction it is assumed to be already stiff at its reference configuration. This 'artificial' setting, as shown next, is able to satisfyingly model the physical behavior of balloon catheters.

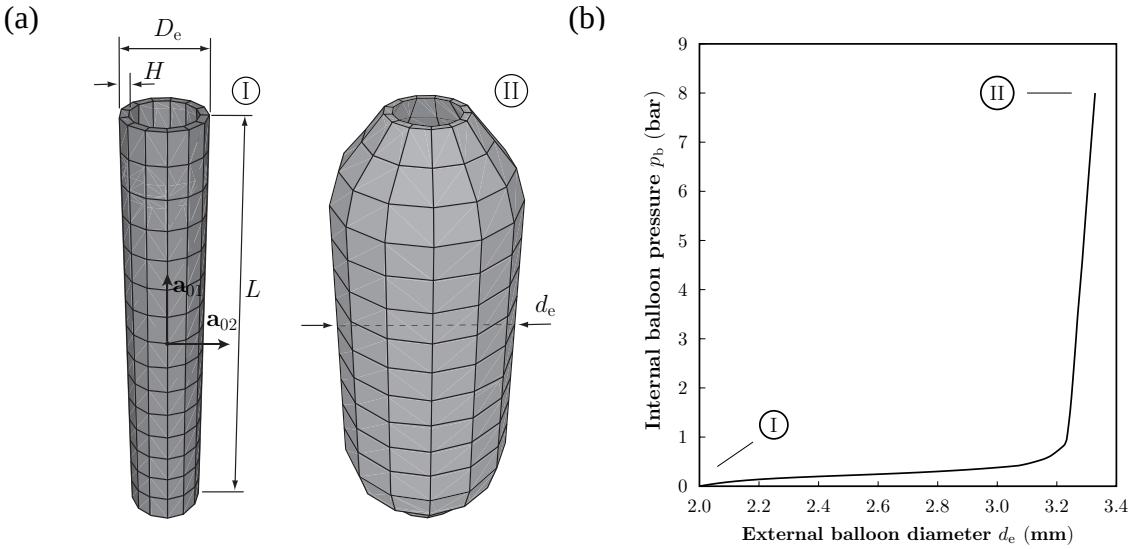

Figure 2.11: Finite element simulation of the dilation of a Grüntzig-type balloon catheter: (a) geometry and computational mesh of the undeformed (I) and deformed (II) configurations of the balloon; (b) applied internal balloon pressure p_b versus external balloon diameter d_e. Initially, the balloon expands fast and only a low internal pressure is needed for its deformation. As the pressure exceeds approximately 1 bar, the balloon stiffens and deforms only slightly.

An additive split of the isochoric strain-energy function $\overline{\Psi}$ is suggested. Hence, $\overline{\Psi}$ consists of a part $\overline{\Psi}_{\text{iso}}$ associated with isotropic deformations of the matrix material, and a part $\overline{\Psi}_{\text{aniso}}$ associated with anisotropic deformations. The two-term potential can then be written as

$$\overline{\Psi}(\overline{\mathbf{C}}, \mathbf{a}_{01}, \mathbf{a}_{02}) = \overline{\Psi}_{\text{iso}}(\overline{\mathbf{C}}) + \overline{\Psi}_{\text{aniso}}(\overline{\mathbf{C}}, \mathbf{a}_{01}, \mathbf{a}_{02}) \tag{2.18}$$

where $\mathbf{a}_{0i}$, $i = 1,2$, are the reference unit directional vectors which characterize the material axes of the orthotropic model (see Figure 2.11(a)).

By introducing the structure tensors $\mathbf{A}_i$, $i = 1,2$, defined as the tensor products $\mathbf{a}_{0i} \otimes \mathbf{a}_{0i}$, $i = 1,2$, we may write [80]

$$\overline{\Psi}(\overline{\mathbf{C}}, \mathbf{A}_1, \mathbf{A}_2) = \overline{\Psi}_{\text{iso}}(\overline{I}_1) + \overline{\Psi}_{\text{aniso}}(\overline{I}_4, \overline{I}_6), \tag{2.19}$$

with

$$\overline{I}_1 = \text{tr}\overline{\mathbf{C}}, \quad \overline{I}_4 = \overline{\mathbf{C}} : \mathbf{A}_1, \quad \overline{I}_6 = \overline{\mathbf{C}} : \mathbf{A}_2. \tag{2.20}$$

The invariants $\overline{I}_4$ and $\overline{I}_6$ are the squares of the stretches in the directions of $\mathbf{a}_{01}$ and $\mathbf{a}_{02}$, respectively, and have, therefore, a clear physical interpretation. From the above equation it is obvious that anisotropy arises only through $\overline{I}_4$ and $\overline{I}_6$.

The isotropic response of the matrix material is determined through a neo-Hookean model of the form $\overline{\Psi}_{\text{iso}} = \mu(\overline{I}_1 - 3)/2$, where $\mu > 0$ is a stress-like material parameter. For the

description of the anisotropic part of the strain-energy function, the following equation is proposed

$$\overline{\Psi}_{\text{aniso}}(\overline{I}_4, \overline{I}_6) = \sum_{i=4,6} \frac{d_{1,i}}{n} (\overline{I}_i - d_{2,i})^n. \tag{2.21}$$

The parameters n and $d_{2,i}$, $i = 4, 6$, are dimensionless, while $d_{1,i}$, $i = 4, 6$, have dimensions of stress. The stiffness in each direction is described by $d_{1,i}$, while $d_{2,i}$ defines the initial point of storage of strain energy, or in other words the initiation of the balloon's stiffening behavior.

In the present simulation, the chosen values for the three parameters mentioned above, do not derive from a fitting algorithm of experimentally observed pressure-diameter responses of Grüntzig-type balloon catheters. The values are chosen with respect (i) to the typically observed behavior of balloon catheters, and (ii) to the requirements of the problem in hand. Balloon catheters are axially stiff in their reference configuration, which can be accounted for by choosing a value $d_{2,4} = 1$. The operational diameter of the balloon catheter should be taken into account. The fully expanded diameter of the balloon is chosen equal to the diameter of the healthy part of the artery, hence approximately 3.5 mm. That implies a desired total circumferential stretch of 1.7, and, consequently, leads to $d_{2,6} = 2.25$ (activation of circumferential stiffening at a stretch of 1.5). For both directions, the values $d_1 = 500$ and $n = 3$ are chosen, and for the neo-Hookean model the value $\mu = 100\,\text{N/mm}^2$ is used.

The results of a finite element analysis of the dilation of a balloon catheter, based on the model and the parameters given above, are depicted in Figure 2.11. The reference and the deformed configuration, and the applied internal balloon pressure versus the external balloon diameter are given. As can be seen in Figure 2.11(a), with the exception of the boundaries, the inflated balloon has a similar cylindrical shape as the balloon in its initial configuration, which is close to the behavior of Grüntzig-type balloon catheters. In Figure 2.11(b), it is shown that during inflation the external balloon diameter d_e increases rapidly at the beginning, and then, between balloon pressures $p_b = 1$ and $p_b = 6\,\text{bar}$, the balloon expands only slightly with inflation pressure, exposing a strongly nonlinear behavior. These results qualitatively agree with the experimental study published in [133]. Note that this peculiar mechanical response could not be obtained by means of isotropic material models.

Contact interactions

In the numerical modeling of stenting three surfaces may come into contact and have to be specified as contact pairs. The involved pairs are: (i) stent-balloon, (ii) stent-artery and (iii) artery-balloon. In all three cases, the first body is considered as the contractor body and the second as the target. Following the node-to-surface approach, the contractor surfaces are described by contractor points, which are the nodes of the finite element mesh located on the contacting surface. The target surfaces are discretized by means of the uniform cubic B-spline surfaces, as described in Section 2.3.

Although the contact approach could be extended to capture frictional behavior, the simulation is carried out without friction since reliable coefficients describing the frictional behavior between the intimal surface and the medical devices are not yet available.

Finite element discretization

One of the important aspects of simulating balloon angioplasty with stenting is the discretization of the involved geometric models of the artery, the balloon and the stent. Especially in that case where multiple contact problems are considered, fine meshes could lead to computationally expensive and prohibiting computations. Nevertheless, the chosen number of elements and nodes should always lead to numerically stable and reliable solutions. As mentioned in the Section 2.3, cubic B-splines depend upon structured surface grids of 4×4 nodes. This requirement leads to the discretization of every target surface by means of structured hexahedral elements.

As can be seen from Figure 2.9, the morphology of the investigated arterial specimen is complex. The artery is heavily sclerotic (small lumen) and for this reason, the thickness and the curvature of the arterial wall varies significantly along the axis of the artery. It is, therefore, clear that the generation of a computational mesh consisting exclusively of hexahedral elements is a challenging task. The mesh generation toolkit CUBIT [172] addresses the problem successfully. The obtained mesh consists of 4215 eight-node isoparametric hexahedral elements.

The generation of the computational meshes for the balloon and the stent requires less amount of effort since their geometry do not present the same complexity. The design of the stent, implies the use of two-node 3D frame elements. The mesh in this case is generated automatically through the algorithm mentioned previously, that also provides the stent's overall 3D geometry model. The parameters defining the number of nodes of each strut are given in Figure 2.10(b). The mesh of the stent consists of 525 nodes, each one has six degrees of freedom. The geometric model of the balloon catheter, as in the case of the artery, is discretized by means of 195 eight-node isoparametric hexahedral elements.

Boundary conditions

The geometry of the three bodies refers to a Cartesian coordinate system, as shown in Figure 2.9(a). In order to avoid rigid-body motions and to construct a good-conditioned system of equations, appropriate boundary conditions have to be applied. The boundary conditions chosen in this case are as following: (i) the end faces of the balloon and the artery are bounded in all three directions; (ii) the y- and z-displacements of a node of the stent located on its middle plane are fixed, allowing the radial expansion of the stent but not its rigid motion.

Loading procedure

In order to simulate the physiological state of the artery, a displacement-controlled axial pre-stretch of 1.2 is applied at all nodes located on the end faces of the artery. At the end of this loading, the displacement boundary conditions are replaced by equivalent reaction forces. The mean arterial pressure of 100 mmHg (13.3KPa) is not taken into consideration in the simulation since the loads deriving from the contact interaction of the three bodies are much higher (as shown in the next section).

In a clinical situation, the artery, the stent and the balloon catheter will deform during the insertion process, especially for the tortuous lumen investigated. However, the simulation of this process is associated with high computational cost. Hence, we have chosen a strategy where the undeformed balloon catheter and stent are placed in the lumen with an overlap. Then, in a few load steps, the penalty parameter, which enforces the contact constraint for all contact pairs, is gradually increased from zero to a desired value of 0.5 N/mm. This strategy aligns the balloon and the stent with the arterial inner surface in a numerically efficient way.

Next, the expansion of the balloon-stent-artery system is simulated. This is done by deformation dependent pressure loads, which are applied on the inner surface of the balloon. As the inner pressure increases, the balloon catheter comes into contact with the stent and after a further pressure increase both medical devices come in contact with the artery leading to the desired increase of the internal diameter of the arterial wall. Finally, after full expansion of the balloon at an inner pressure of approximately 8 bar, the pressure loads are gradually removed, and only the stent remains in contact with the artery.

Results

In this section the numerical outcome of the angioplasty simulation with stenting is presented. We introduce specific indicators with the aim to quantify the changes in the mechanical environment and the lumen area of the artery. In addition, a comparison between the two stent designs is provided, emphasizing their merits, advantages and disadvantages and providing the basis for parametric analysis and assessment of different stents. The presented results provide evidence of the ability and effectiveness of the developed computational tools to treat challenging 3D contact problems such as the 3D simulation of balloon angioplasty with stenting.

A meaningful measure characterizing the success rate of the discussed medical treatment, is the change of the lumen area during and after balloon angioplasty with stenting. This measure we denote as **L**umen **G**ain and is expressed through the factor LG, which was introduced in [86], and defined as

$$LG = \frac{A_{\mathrm{l,cur}}}{A_{\mathrm{l,ref}}} - 1, \tag{2.22}$$

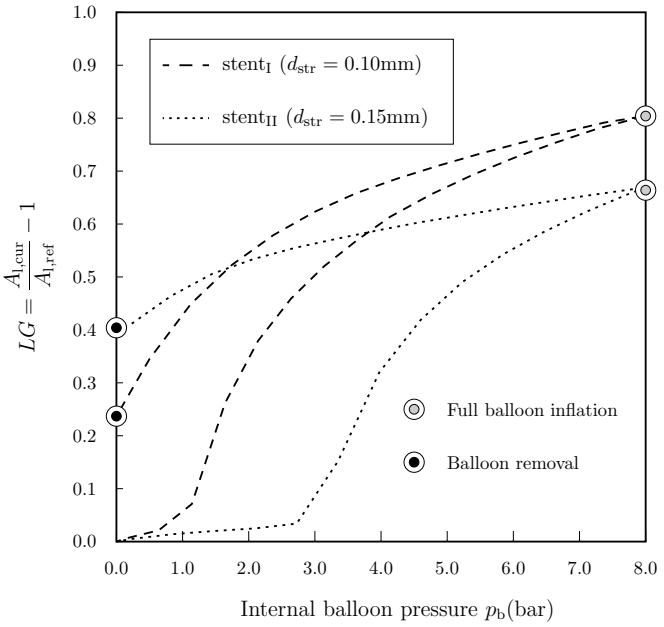

Figure 2.12: **L**umen **G**ain factor (*LG*) versus internal balloon pressure p_{b} at the most stenotic section of the arterial wall, at Section *A-A* (compare with Figure 2.9). The two curves indicate the change of *LG* along the inflation and deflation paths of the balloon for both stent designs (stent$_{\mathrm{I}}$ and stent$_{\mathrm{II}}$).

where $A_{\mathrm{l,ref}}$ is the area of the smallest cross-section of the inner arterial wall before stenting, and $A_{\mathrm{l,cur}}$ is the related current area of the cross section at the same location.

Figure 2.12 shows the change of *LG* at $z = 17.5\,\mathrm{mm}$ (location of the narrowest lumen area, see Section *A-A* in Figure 2.9), with respect to the internal balloon pressure p_{b}. The inflation and deflation paths when both stents (stent$_{\mathrm{I}}$ and stent$_{\mathrm{II}}$) are used, are illustrated by dashed lines of different intensity. As can be seen from Figure 2.12, stent$_{\mathrm{I}}$ leads to $LG = 0.81$ when the balloon is fully inflated ($p_{\mathrm{b}} = 8\,\mathrm{bar}$), and to $LG = 0.24$ when the balloon is removed ($p_{\mathrm{b}} = 0\,\mathrm{bar}$). Likewise, when the simulation is performed with stent$_{\mathrm{II}}$, the values $LG = 0.67$ and $LG = 0.40$ are obtained. These results clearly point out that at the end of the balloon inflation, stent$_{\mathrm{I}}$ is wider expanded, providing a higher *LG* value. Nevertheless, as the balloon is gradually deflated and finally removed, stent$_{\mathrm{II}}$ with thicker struts leads to an almost 70% wider lumen in comparison to stent$_{\mathrm{I}}$, indicating a more successful outcome of the treatment, as far as the lumen area is concerned. The edges in the *LG*-p_{b} curves at the points p_{b} =1.2 and 2.8 bar for stent$_{\mathrm{I}}$ and stent$_{\mathrm{II}}$, respectively, correspond to the elastic limit of the two stents.

Similar results can be seen in Figure 2.13, where the lumen area A_{l} is plotted along the *z*-axis (the balloon catheter and the stent is located between $z = 13.4\,\mathrm{mm}$ and $z = 21.4\,\mathrm{mm}$). The three curves in each plot refer to the reference lumen area, the lumen area at full balloon inflation ($p_{\mathrm{b}} = 8\,\mathrm{bar}$) and after balloon removal ($p_{\mathrm{b}} = 0\,\mathrm{bar}$). The total lumen gain at the end of the procedure is represented by the grey area. An immediate comparison

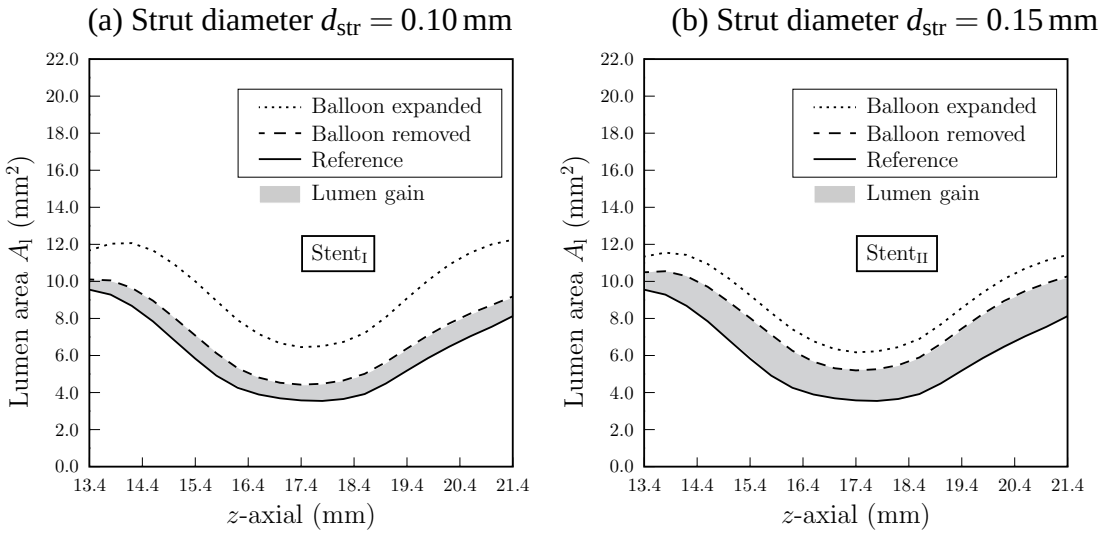

Figure 2.13: Lumen area A_l at the reference configuration, after full balloon expansion and after balloon removal plotted along the z-axis (see Figure 2.9) where the balloon and the stent is located. The results obtained for the two different stents (stent$_I$ and stent$_{II}$) are depicted in (a) and (b), respectively.

between the two figures indicates that both stents provide a successful outcome, but stent$_I$ leads to a smaller lumen area throughout the stenotic part of the femoral artery under investigation. Comparable results linking the stent strut thickness and the lumen gain are also reported in the numerical study [86]. Finally, from Figure 2.13 one can derive the conclusion that the profile of the inner arterial wall remains almost unaltered throughout the procedure.

One of the most important drawbacks of angioplasty is the vascular damage caused by the stent struts. As documented in [101], elevated pressures around the struts may lead to growth of the artery tissue and to a decreased success rate of the angioplasty treatment due to restenosis. In addition, References [111, 181] conclude that permanent, non-physiological strains, generated in the arterial wall during and after the expansion of the stent, may also lead to cellular proliferation, and finally to restenosis. All the above imply that the optimization of stenting and the stent design is not a one parameter problem (for example, maximization of lumen area). Therefore, additional indicators, which allow the quantification of the changes in the mechanical environment of the artery, should be introduced. Taking the above into consideration, a deeper insight of the generated pressure and strain fields of the arterial wall can be achieved.

Figures 2.14 and 2.15 depict the numerical results of the performed simulations in form of the contact pressure and the strain distribution, respectively. In particular, Figure 2.14 illustrates the contact pressure p_c which acts on the stenotic inner arterial wall for both cases, stent$_I$ and stent$_{II}$ after complete deflation and removal of the balloon catheter ($p_b = 0\,bar$). The contact pressure is computed for each finite element facet $\mathbf{q}_j$ of the inner

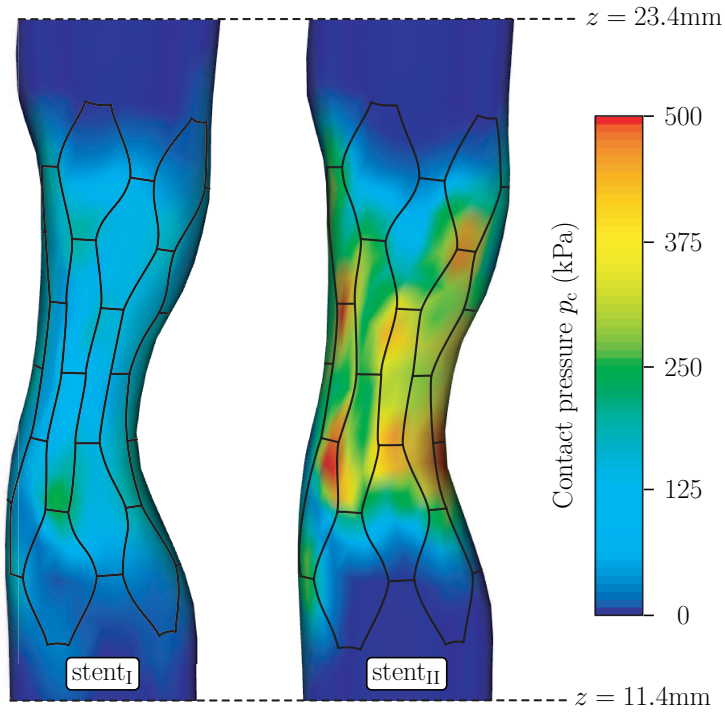

Figure 2.14: Distribution of the contact pressure p_c acting on the stenotic inner arterial wall through the stent struts after removal of the balloon, for both cases stent$_{\mathrm{I}}$ and stent$_{\mathrm{II}}$.

surface of the artery through

$$p_{c,j} = \frac{1}{4}\frac{\sum_{i=1}^{4} F_{i,j}}{A_j}, \tag{2.23}$$

where $F_{i,j}$ denote the reaction forces at the four nodes of each facet $\mathbf{q}_j$, and A_j is the area of the facet. Figure 2.14 indicates, as expected, that the generated contact pressure in the case of the stiffer stent$_{\mathrm{II}}$ is approximately two times higher compared to stent$_{\mathrm{I}}$, while the pressure field retains almost the same pattern. Interestingly, the position of the highest pressure is located around the horizontally positioned struts of the stents.

Another possible information that could be provided by the performed numerical simulations, and that possibly characterizes the short- and long-term mechanical changes in the arterial wall, are the stresses within the stenotic arterial wall. In this study, however, the tissue is modeled as a homogeneous and isotropic material (see Section 3.1). This simplification, does not allow a physical interpretation of the stresses. A more reliable and informative measure is the strain.

Figure 2.15 shows the distribution of the principal Euler-Almansi strains, say e_1, e_2, e_3, at the current configuration of the most stenotic section of the femoral artery ($z = 17.5$ mm), at (a) full expansion of the angioplasty balloon and (b) after removal. The results for both stent$_{\mathrm{I}}$ and stent$_{\mathrm{II}}$ are graphically illustrated. The strains reported at full balloon inflation

depict the short-term changes in the mechanical environment of the artery due to stenting, while the strains after removal of the balloon indicate the more important (for the outcome of the medical procedure) long-term evolution of the loading field.

Since the circumferential direction is the main loading direction in balloon angioplasty with stenting (due to the radial expansion of the balloon and stent), it can be concluded that the principal axis 1 (where the highest strains are reported — 40%) is the circumferential direction. The axial displacement loads applied at the end faces of the artery, representing the physical pre-stretch of the artery tissue (as documented in Section 2.5.2), leads to approximately 10% axial stretch of the middle, highly curved part of the arterial wall. This value is comparable to the maximum computed value of the principal strain e_2, as depicted in Figure 2.15(a). Hence, it can be assumed that the principal direction 2 is the axial direction. It should be mentioned, that the curved geometry of the artery is responsible for the presence of tensile and compressive axial loads in the same section. Finally, we may conclude that the principal axis 3 is mainly located along the radial direction.

As mentioned previously, the thinner stent_I is expanded further than stent_II since stent_II is stiffer. Therefore, when the angioplasty balloon is fully inflated, the computed circumferential strains are approximately 10% higher at the inner border of the arterial wall, when stent_I is used.

Exactly the opposite is the case after balloon deflation (Figure 2.15(b)), where 10% higher circumferential strains are computed for the case of stent_II. That leads to the conclusion that the non-physiological loading applied with stent_II has a more severe effect on the mechanical environment of the artery after the end of the procedure. On the other hand, with stent_II a wider lumen area is achieved, as can be seen in Figure 2.15(b). For the principal strains e_2 similar conclusions can be drawn, even though the differences in induced axial strains when stent_I or stent_II is used are not as profound as in the circumferential direction. Note that the tensile and compressive zones are almost concentrically distributed after balloon deflation. Finally, the principal strain field e_3 preserves almost the same pattern, with the distinct difference that the removal of the balloon leads to higher negative radial strains around the inner arterial wall.

2.6 Discussion and conclusion

Physical modeling and computer simulation of balloon angioplasty with stenting is an up-to-date research topic in computational biomechanics. Computational tools such as the finite element method have the potential to provide engineers and clinicians with patient-specific analysis to optimize medical devices such as stents and ballooon catheters in order to improve the clinical outcome.

Today, computer simulation of stent procedures is still a demanding task due to the complex material behavior of the involved components, and more importantly, due to the 3D contact interaction of the balloon, the stent and the arterial wall. Commonly, the contact

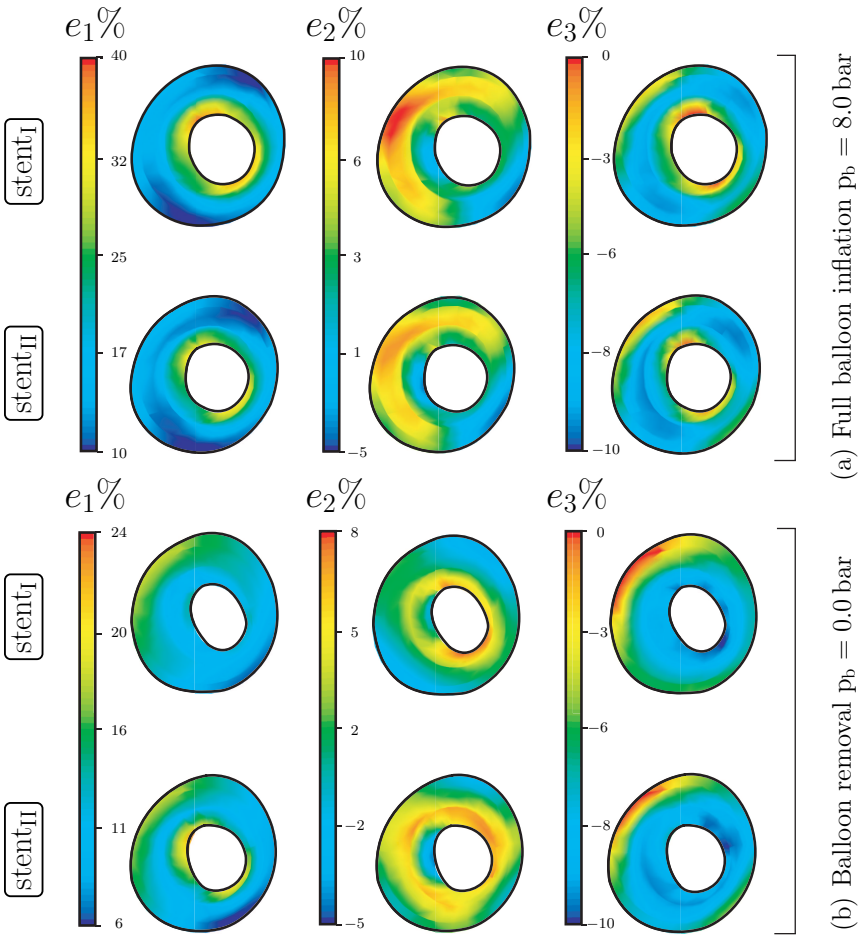

Figure 2.15: Comparison of the induced Euler-Almansi principal strain fields due to stenting (stent$_{\mathrm{I}}$ and stent$_{\mathrm{II}}$) at the deformed configuration of the most stenotic section of the arterial wall ($z = 17.5\,\mathrm{mm}$). The strains are plotted at two characteristic stages of the procedure, (a) at full balloon inflation ($p_{\mathrm{b}} = 8.0\,\mathrm{bar}$), and (b) after balloon removal ($p_{\mathrm{b}} = 0\,\mathrm{bar}$).

surfaces are described by planar facets that may lead to non-physical oscillations of contact forces and, consequently, to an influence of the rate of convergence within a nonlinear solution scheme. Hence, there is a need for more efficient and robust contact algorithms, based on higher order surface parameterizations.

The present work proposes a new 3D contact scheme that is based on C^2-continuous parameterizations, more specifically on uniform cubic B-splines. Detailed guidelines are provided for the implementation of the scheme into the open-source program FEAP [171]. The contact algorithm was successfully applied to a classical problem in contact mechanics, involving finite deformation and large sliding, and to treat the interactions that occur during the balloon-stent inflation in an atherosclerotic artery. The proposed computational

model of stenting represents an advanced approach capable of gaining more insight into the interventional treatment of atherosclerotic arteries.

Among the contributions of the work is the use of cubic B-splines with a novel polynomial function. This parametrization technique, which we called modified cubic B-splines, retains C^2-continuity. It enables the interpolation of the superficial nodes of the contacting bodies without any approximation or fitting. Thus, more accurate representations of geometries can be acquired. Moreover, the modified cubic B-splines do not require any additional computational effort. However, the new parametrization approach reveals also a drawback. In the case that the model includes abrupt curvature changes within short distances, the modified cubic B-splines generate undesirable undulations between the finite element (control) nodes. Nevertheless, the surface always remain smooth and no convergence problems occur during the numerical analyses.

Several sophisticated numerical tools including the MATHEMATICA package ACEGEN are used in order to compute contact contributions to the finite element arrays. Such tools provide differentiated (and optimized) expressions by means of stochastic evaluations. In addition, a technique is proposed in order to limit the computational cost of finding the contact partner elements for a particular slave point and to identify the contact point in terms of the surface coordinates.

For the computer simulation of the stent procedure a human high-grade stenotic femoral artery was considered for which a complete set of geometric and mechanical data was available. Its geometric model was reconstructed from hrMRI images, while the mechanical response of the artery wall, considered to be homogeneous, was described by an isotropic hyperelastic model able to capture the nonlinear effect of artery tissues within the finite strain domain. In addition, the model considered the axial *in situ* pre-stretch of the artery. Besides the homogeneity and isotropy assumptions, the arterial model did not address vascular injuries which may occur during stent inflation. The mechanical response of the balloon catheter was described by an orthotropic model which is (almost) non-compliant in the axial direction. The model enables very soft responses in the circumferential direction at low internal pressures, while exposing a stiffening effect at higher pressure values. The initially folded shape of the balloon was not considered. Hence, there is a need for model refinements, in particular when clinical issues are addressed.

Finally, two stent configurations (stent_I, stent_II) with the same geometry but with different strut thicknesses were considered to evaluate the individual lumen gain LG and the contact forces exposed on the intimal wall along with the mechanical strains in the artery. The numerical results exhibited a larger lumen gain in the case of the thicker stent_II but also higher contact pressures and higher circumferential and axial strains when compared to the values obtained with stent_I. This finding suggests that even though stent_II leads to a wider lumen, it is not necessarily the optimal solution, because mechanical changes in the artery wall might be responsible for the development of cell proliferation, restenosis and failure of the procedure. This also points to the multi-parametric nature of stent optimization procedures.

Undoubtedly, there is room for refinements in future studies. Uniform and modified cubic B-splines have inherent drawbacks (structured control mesh requirements, non-accurate model representations and localized undulations) that could be refined with more advanced parametrization techniques. On the constitutive modeling side, the heterogeneity of diseased vessel walls should be considered, as, for example, in [86]. The experimentally identified anisotropic behavior of artery tissues due to collagen reinforcement should be modeled by (more) advanced strain-energy functions, as presented in [80, 84, 63]. Despite the mentioned limitations, the proposed contact algorithm has the ability to address realistic 3D problems in biomechanics, where finite deformations and arbitrarily curved geometries are involved. A thorough biomechanical simulation on such a basis (patient-specific model, three-body contact) could serve as a foundation for realistic risk assessment and for designing intervention.

3 A NUMERICAL MODEL TO STUDY THE INTERACTION OF VASCULAR STENTS WITH HUMAN ATHEROSCLEROTIC LESIONS

Abstract—A methodology is proposed that identifies optimal stent devices for specific clinical criteria. It enables to predict the effect of stent designs on the mechanical environment of stenotic arteries. In particular, we present a numerical study which is based on the interaction of a vascular stent with a patient-specific, atherosclerotic human iliac lesion of type V. The stress evolution in four different tissue components during and after stenting is investigated. The geometric model of the artery is obtained through MRI, while anisotropic material models are applied to describe the behavior of tissues at finite strains. In order to model the observed fissuring and dissection of the plaque under dilation, the undeformed configuration of the arterial wall incorporates two initial tears. The 3D balloon-stent-artery interaction problem is modeled by means of a contact algorithm, which is based on a C^2-continuous surface parametrization, hence avoiding numerical instabilities of standard facet-based techniques. In the simulations three different stent designs are studied. The performance of each stent is characterized by scalar quantities relating to stress changes in the artery, contact forces and changes in lumen area after stenting. The study concludes by suggesting two optimal stent designs for two different clinically relevant parameters.

Keywords—atherosclerosis; balloon angioplasty; contact; finite element method; mechanical stress; modeling; MRI; stent

3.1 Introduction

Balloon angioplasty with stenting is a well established and effective vascular reconstructive procedure aiming to reduce the severity of atherosclerotic stenosis, one of the most frequent form of cardiovascular diseases. Its popularity arises due to its less invasive nature (compared to surgical alternatives) and its better clinical outcome (compared to balloon angioplasty without stenting[156, 75]).

Despite the constantly increasing success rate of stenting through technological progresses in stent design and drug coatings on the stents' surface[18], the procedure can still fail because of in-stent restenosis which occurs in 30-60% of patients with complex lesions [50]. Restenosis is a mechanobiological process characterized by stress-induced growth, such as neointimal hyperplasia. In more detail, the focal vascular trauma imposed by the struts of the stent, the stress and strain environments around the expanded stent, and the existence of a foreign material in the injured artery may trigger molecular mechanisms,

leading to inflammation, granulation and extracellular matrix production [181, 184, 153]. These processes may lead to reclosure of the blood vessel, which results in the need for further interventions.

Balloon angioplasty with stenting is a procedure of mainly mechanical characteristics. It is, therefore, understandable that its outcome depends on the design parameters defining the mechanics of the stent such as the material and the geometry of stent cells and struts. This is supported by recent clinical studies [97, 135], which identified the stents' geometric characteristics as one of the major elements for reducing or increasing the risk of restenosis. Towards this direction, numerical tools such as the finite element method have been recently applied in order to investigate the biomechanical implications of vascular stenting and to provide optimal configurations of medical devices.

A literature survey on the recently published numerical attempts to model atherosclerotic lesions revealed that, still in the majority of computational models developed in recent years, the non-diseased arterial wall and the plaque are frequently modeled as a homogeneous and single-layer structure [125, 106, 13]. In addition, several models assume the arterial tissue to be isotropic, which do not reflect the experimentally observed cylindrically orthotropic behavior of non-diseased[183, 1, 195, 152, 151, 77, 84] and diseased[83, 85] vascular tissues. It seems also that only a few studies have considered three-dimensional (3D) geometries [87, 86, 100]. Although simplified approaches have contributed to the current level of understanding of angioplasty mechanics, there is a need to model the actual 3D morphology and the related mechanics in a more realistic way and on a patient-specific basis. To the best of the authors' knowledge, the study by Liang et al.[114] was the first to incorporate the balloon in a simulation considering a stent, however, simplified, cylindrical geometries were considered. A detailed approach seems to be the one documented by Holzapfel et al.[86], where the accounted arterial geometry consisted of eight different tissue models, obtained through high-resolution magnetic resonance imaging (hrMRI), while anisotropic material models were applied to describe the behavior of tissues at finite strains. As in the previously mentioned attempts, the contact interaction of the balloon catheter was not modeled. In addition, the used finite element meshes and the geometric representation of the arterial wall were not particularly fine.

The present work is a step towards improving the numerical modeling of balloon angioplasty with stenting by taking the interaction of vascular stents with human atherosclerotic lesions into account. Three-dimensional morphological data of a type V atherosclerotic lesion[162] of an iliac artery are considered. The arterial wall is modeled as a non-homogeneous solid, consisting of four different tissue components. The applied constitutive models are able to capture the nonlinear, anisotropic behavior of arterial tissues. A vascular stent, received from a stent-producing company, is parametrized. In addition, two modified geometric designs are generated. A cylindrically orthotropic model is used in order to describe the anisotropic behavior of balloon catheters under internal pressure load. Balloon angioplasty with stenting is numerically performed by solving the balloon-stent-artery interaction as a 3D contact problem. For this purpose, a C^2-continuous surface description is applied, which prevents numerical instabilities arising from non-smooth body

discretization [165, 100]. The proposed computational model also attempts to provide a deeper insight into the dominating effect of plaque fissuring and dissection during stenting [21, 117, 109]. This is performed by introducing two (small) initial cracks near the edges of the plaque.

The study results in the identification of changes in the mechanical environment of the artery during and after stenting, when the three different stent designs are used. Particular emphasis is placed on the generated stress fields of the four arterial tissues. The performance of the different stents is quantified by means of three scalar indicators[86]. These indicators characterize the lumen gain and the arterial injury imposed by the stents. Therefore, they may be helpful in finding the optimal stent design for the particular stenosis and for specific optimization criteria.

3.2 Geometric and material modeling

This section provides the geometric and material modeling aspects of the vessel wall and the involved medical devices, i.e. the balloon catheter and the stent. The section starts by the description of the 3D arterial model based on image data, and introduces the adopted continuum formulation, which is able to incorporate the nonlinearity and anisotropy inherent in human tissues. Next, account of a stent model, based on a currently used product, is given and finally a cylindrically orthotropic material model is presented in order to describe the deformation of angioplasty balloons under internal pressure.

3.2.1 Arterial model

In the present numerical study, a detailed geometric and physical model of an atherosclerotic-prone human external iliac artery (65 yrs, female) is considered. The regarded lesion is of type V, according to the classification proposed by Stary [162]. This type of stenosis is characterized by prominent new fibrous connective tissue and a lipid core. The 3D geometry of the arterial wall architecture was traced by means of hrMRI and reconstructed by non-uniform rational B-splines (NURBS), as can be seen in Figure 3.1(I). A detailed description of the procedure and the associated histological analyses, required to identify the underlying tissue types, is provided in the references [8, 85]. The identification of the 3D tissue structure is regarded as an important aspect of the documented attempt, and it is a necessary prerequisite of meaningful simulations of balloon angioplasty with stenting. According to the classification proposed by Holzapfel et al. [85], seven different tissue types are identified in the atherosclerotic arterial wall: adventitia (A), non-diseased media (M-nos), non-diseased intima (I-nos), fibrous cap (I-fc), fibrous intima at the medial border (I-fm), lipid pool (I-lp), and fibrous media (M-f). For the purpose of this study, M-nos and M-f are combined to one tissue component referred to as ‘media’ (M), and I-nos, I-fc and I-fm are combined to another component referred to as ‘intima’ (I). The consideration of all seven arterial tissues would require detailed information about the anisotropy of

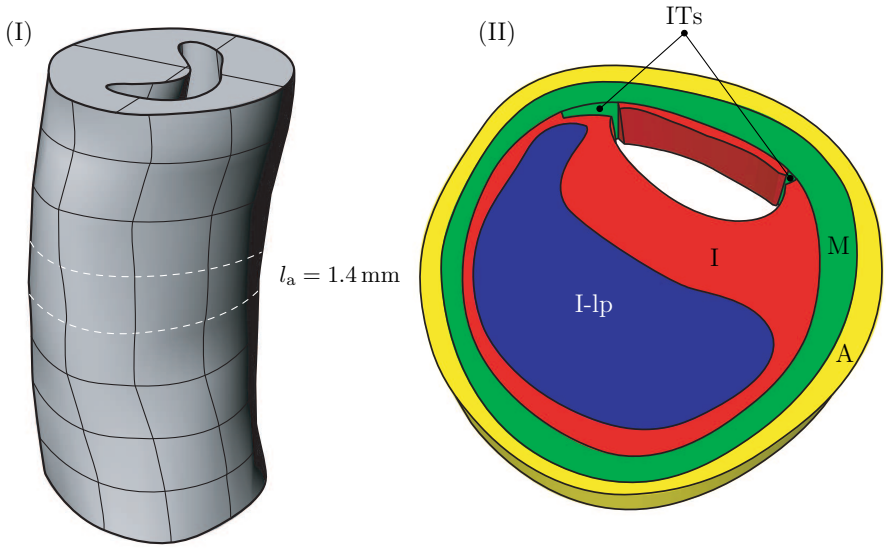

Figure 3.1: (I) 3D geometric model of a stenotic human iliac artery obtained from hrMRI and reconstructed by means of NURBS. (II) Extracted arterial slice with length $l_a = 1.4\,\mathrm{mm}$, composed by four arterial tissues: adventitia (A), media (M), intima (I) and lipid pool (I-lp). The introduced initial tears (ITs) are also indicated.

each individual tissue, as discussed later in this section. From the complete arterial wall a section with length $l_a = 1.4\,\mathrm{mm}$ (which is also the smallest cell length of the stent) is considered, which incorporates four tissue types (see Figure 3.1).

Balloon angioplasty and stenting frequently lead to fissuring and dissection of the atherosclerotic plaque [21], which is thought to be one of the main mechanisms of lumen gain obtained through this procedure. A reliable prediction of the stress field of the stented arterial wall requires the incorporation of these effects. However, the present work does not investigate the fissuring and dissection from a fracture mechanics point of view, as performed recently by, for example, Gasser and Holzapfel [62]. Instead two initial tears (ITs) are introduced into the intima. A similar approach is published by Gasser and Holzapfel [61]. The initial cracks are placed at the edges of the plaque (the plaque shoulder) because experimental studies indicate these locations as the most prominent ones to plaque rupture [117, 109]. The arterial slice described above is depicted in Figure 3.1(II).

The choice of the constitutive response used for the involved tissue components is of fundamental importance for the reliable prediction of the evolution of stresses and strains during stenting. For the determination of the passive, quasi-static mechanical properties of the individual tissue components, mechanical tests were performed on a computer-controlled, screw-driven, high-precision tensile machine. Rectangular stripe samples with axial and circumferential orientations were excised and stretched far beyond their physiological loading domain in order to capture the range of deformations induced by the stent. The lipid pool did not allow tensile testing due to its fluid-like consistency. A detailed description of the performed mechanical tests is documented in the study [83].

Tissue	μ (kPa)	k_1 (kPa)	k_2 (-)	α ($^\circ$)
Adventitia (A)	1.75	65.6	61.8	$\pm$49.0
Media (M)	15.0	4.0	2.3	$\pm$7.0
Intima (I)	78.9	23.7	26.3	0.0
Lipid Pool (I-lp)	0.1	0.0	–	–

Table 3.1: Material and structural parameters of different tissue types, describing the anisotropic response of an atherosclerotic iliac lesion of type V. Data taken from Holzapfel et al.[87]

Arterial tissues are anisotropic, heterogeneous, highly deformable, (nearly) incompressible and show a pseudo-elastic behavior [91]. Following the work [80], it is assumed that each tissue component is reinforced by two families of collagen fibers embedded in an isotropic ground matrix. This reinforcement renders the material properties anisotropic. The fibers' (mean) preferred directions are represented by two unit vectors, say $\mathbf{a}_{01}$ and $\mathbf{a}_{02}$. The isochoric part $\overline{\Psi}$ of the strain-energy stored in the non-collageneous and collageneous components is given by[80]

$$\overline{\Psi} = \overline{\Psi}(\overline{I}_1, \overline{I}_4, \overline{I}_6) = \mu(\overline{I}_1 - 3) + \frac{k_1}{2k_2} \sum_{i=4,6} \left\{ \exp\left[k_2(\overline{I}_i - 1)^2\right] - 1 \right\}, \tag{3.1}$$

where $\overline{I}_1 = \mathrm{tr}\overline{\mathbf{C}}$ is the first invariant of the modified Cauchy-Green tensor $\overline{\mathbf{C}} = J^{-2/3}\mathbf{C}$ [76], and $\overline{I}_4 = \overline{\mathbf{C}} : \mathbf{a}_{01} \otimes \mathbf{a}_{01}$ and $\overline{I}_6 = \overline{\mathbf{C}} : \mathbf{a}_{02} \otimes \mathbf{a}_{02}$ are two invariants. The material parameters μ and k_1 have dimensions of stress, while k_2 is a dimensionless parameter. The first part of Equation (3.1) models the contribution of the non-collageneous ground matrix, while the second part, characterizes the energy stored in the collagen fibers.

The strain-energy described in Equation (3.1) is used for each of the four tissue components, but with a different set (μ, k_1, k_2) of material parameters, and different direction vectors ($\mathbf{a}_{01}$ and $\mathbf{a}_{02}$) associated with the structure. Up to now, there are unfortunately no data available in the literature, concerning the collagen structure of stenotic iliac arteries. In the present approach, the structural data $\mathbf{a}_{01}$ and $\mathbf{a}_{02}$ are treated phenomenologically and are estimated from the mechanical tests described previously. In addition, the components of the collagen fibers' direction vectors in the radial direction are neglected, allowing thus the description of $\mathbf{a}_{01}$ and $\mathbf{a}_{02}$ by an angle α, defined between the fiber reinforcement and the circumferential direction of the individual layer. The least-square fitting of the constitutive model to the anisotropic data reported in the reference [87] leads to the determination of the three involved material parameters (μ, k_1, k_2) and the structural parameter α. The obtained values are summarized in Table 3.1.

Stent configurations	s_t (mm)	l_{st} (mm)
S_1 (control stent)	0.14	$\pi D/15$
S_2 (thinner struts)	0.10	$\pi D/15$
S_3 (fewer struts)	0.14	$\pi D/7$

Table 3.2: Values of the geometric parameters of the three different stent designs used in the simulations of balloon angioplasty with stenting. The value of the diameter D is given in Figure 3.2.

3.2.2 Stent models

First we considered an EXPRESS VASCULAR LD stent with delivery system (guide wire and introducer sheath) obtained from BOSTON SCIENTIFIC SVERIGE AB. The detailed shape and dimensions of the undeformed configuration of the stent, shown in Figure 3.2(I), were studied using an Olympus reflected-light microscope with an attached digital camera.

The 3D computer model of the stent (Figure 3.2(II)) is generated by means of a parametrization algorithm. Parametric design is a useful technique in engineering when products are tailored fit to specific needs or when optimization is used to generate the optimal product design. In the present work, the developed program, aids to the fast generation of different configurations of the provided stent. The algorithm makes use of a series of design parameters, describing the stent's morphology and dimensions. These parameters are depicted in Figure 3.2(II). In addition, the parametrization algorithm is able to provide the finite element mesh of the individual parametrized stent. In the simulations described below, three stent designs are taken into consideration. The first is the obtained stent from BOSTON SCIENTIFIC SVERIGE AB (control stent, labeled as S_1, with specific dimensions shown in Figure 3.2(III)), while the two other designs derive from variations of the parameters defining the width of the struts (s_t) and the wave length of the stent's cell (l_{st}), see Table 3.2. The first variation of the control stent, labeled as S_2, has thinner struts (more compliant structure), while the second variation labeled as S_3, has approximately half of the struts of the control stent (stiffer structure). Since only a slice of the vessel wall is studied, only one cell of the stent is considered.

According to the acquired data, the EXPRESS VASCULAR LD stent is made of stainless steel (316L). The material's elastic regime is described by a neo-Hookean model, while its inelastic response is described by a von Mises-Hill plasticity model with linear hardening. The Young's modulus is $E = 201\,\text{GPa}$ and the Poisson's ratio is $\nu = 0.3$. The yield stress σ_y is chosen equal to 300 MPa and the hardening modulus H_{iso} is equal to 2 GPa.

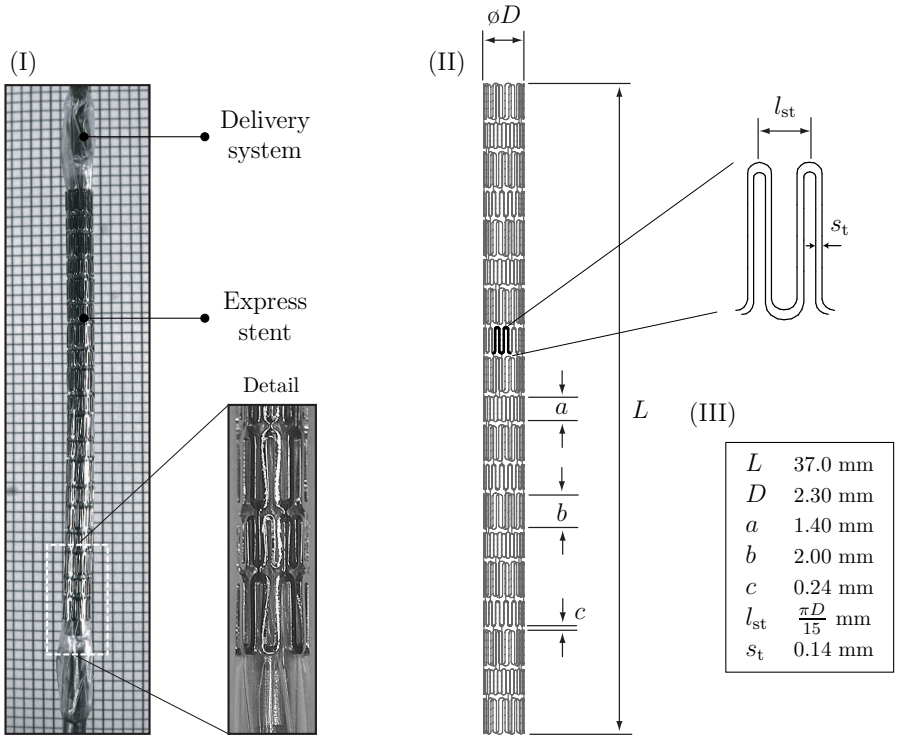

Figure 3.2: (I) Photograph of the undeformed configuration of the pre-mounted EXPRESS VASCULAR LD stent and detailed view of the stent's sinusoidal-structured cells. (II) 3D geometric model of the stent, obtained by a parametrization algorithm that makes use of the shown design parameters. (III) Dimensions of the obtained stent.

3.2.3 Balloon catheter model

Although the initial form of balloon catheters is S- or Z-shaped, the undeformed configuration of the balloon is modeled as a circular cylinder. The outer diameter of the cylindrical balloon is $D_{b,o} = 2.2\,\text{mm}$, the thickness $H_b = 0.2\,\text{mm}$ and the length $l_b = 2.0\,\text{mm}$.

The inflation of balloon catheters is characterized by complex kinematics. Initially, the unfolding of the balloon takes place under low internal pressure. Further increase of the pressure, leads to a continuously increasing diameter, while the catheter retains axially its cylindrical shape. After a specific load, depending on the balloon's mechanical and geometric properties, the balloon exposes rapidly a nonlinear, stiffening behavior. In order to account for the described effects, a cylindrically orthotropic model, based on fiber-reinforced materials' theory, was developed [100]. Briefly, two material axes with different mechanical properties are introduced, oriented in the axial and circumferential directions. Circumferentially, the balloon is very soft initially but particularly stiff after a predefined stretch limit, provided by the stent manufacturer. In the longitudinal direction the balloon is assumed to be already stiff at its reference direction, hence the axial stretch limit is about 1. The introduction of this artificial material allows the imitation of the typical characteristics of balloon catheters [100]. Note that this peculiar mechanical response

could not be obtained by means of isotropic material models.

3.3 Numerical simulations

This section summarizes the developed finite element model of balloon angioplasty with stenting, including the modeling of the contact interactions between the balloon, the stent and the arterial wall. The generation of the computational grid is thoroughly described, and the chosen boundary conditions along with the loading procedure are given. Finally, three indicators able to characterize the stent-artery interaction are discussed in detail.

3.3.1 Contact modeling

For the finite element simulation of contact problems concerning finite deformation, large sliding and arbitrarily curved contact surfaces, standard facet-based contact algorithms may lead to numerical problems. In particular, oscillation of contact forces, non-realistic pressure jumps and finally loss of quadratic convergence are observed, which arise from the sliding of nodes over facets' boundaries, where jumps of the normal vector are experienced [187]. Therefore, the 3D numerical modeling of contact interactions during balloon angioplasty with stenting requires an advanced and robust contact approach. To address the problem mentioned above, and to successfully simulate the contact interactions between the medical devices and the arterial wall, the algorithm based on C^2-continuous uniform cubic B-spline surfaces documented in the reference[100] and implemented into the multipurpose finite element analysis program FEAP[171], is adopted.

In more detail, the involved contact pairs in the simulation are: (i) stent-balloon, (ii) stent-artery and (iii) balloon-artery. The first body in all pairs is considered as the contractor (slave) body, while the second as the target (master) body. Following the node-to-surface contact approach, the surfaces of the contractors are described by their superficial finite element nodes $\mathbf{x}^{\mathrm{s}}$. The target surfaces are described by cubic B-spline surfaces $\mathbf{S}^{\mathrm{m}}$.

A uniform cubic B-spline is obtained by taking a bidirectional mesh of 4×4 control points $\mathbf{P}_{i,j}$, $i,j=1,\ldots,4$, and the products of the univariate cubic basis functions[138]

$$\left.\begin{aligned} B_1(t) &= (1-3t+3t^2-t^3)/6,\\ B_2(t) &= (4-6t^2+3t^3)/6,\\ B_3(t) &= (1+3t+3t^2-3t^3)/6,\\ B_4(t) &= t^3/6. \end{aligned}\right\} \tag{3.2}$$

Thus, the mathematical representation of the uniform cubic B-spline surfaces is

$$\mathbf{S}(u,v)=\sum_{i=1}^{4}\sum_{j=1}^{4}B_i(u)B_j(v)\mathbf{P}_{i,j},\quad 0\le u,v\le 1, \tag{3.3}$$

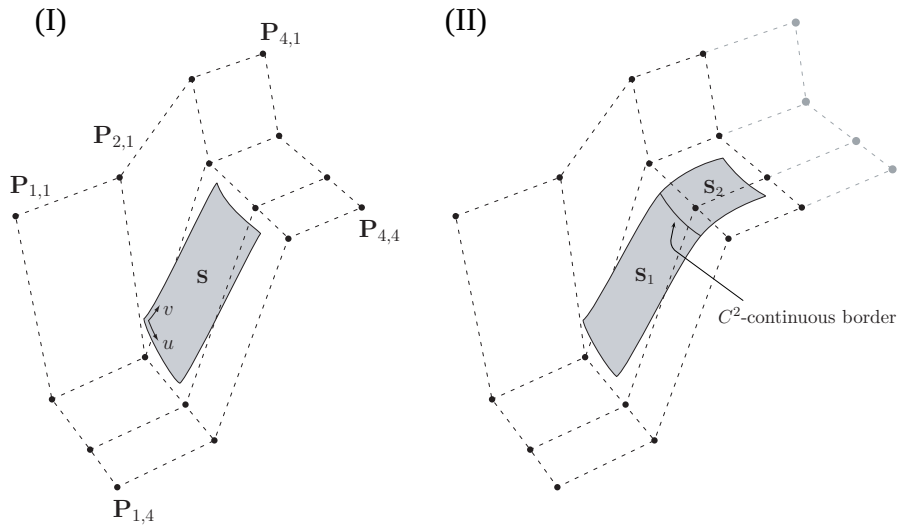

Figure 3.3: (I) A 4×4 mesh with control points $\mathbf{P}_{i,j}$, $i,j = 1,\ldots,4$, and its corresponding uniform cubic B-spline surface. (II) Two overlapping control meshes and two adjacent B-spline surfaces with C^2-continuous borders.

where u and v are convective coordinates, and the parameter t in Equation (3.2) stands for either u or v. For illustrative reasons, Figure 4.7 is given to show the geometrical situation. In Figure 4.7(I) an example of a 4×4 control mesh and its corresponding uniform cubic B-spline surfaces is shown (plotted in MATHEMATICA[185]). In Figure 4.7(II) two overlapping control polyhedrons and two adjacent uniform cubic B-spline surfaces ($\mathbf{S}_1$ and $\mathbf{S}_2$) are illustrated. The C^2-continuous border between the two surfaces is also indicated.

In the presented method, the required structured meshes of control points (noted above as $\mathbf{P}_{i,j}$) for the parametrization of the contact surfaces are generated by the finite element nodes located on the target surfaces. This approach yields a robust interface between the smooth surface and the continuum body. Following the penalty method as the regularization technique for the inequality variational principle of the contact conditions [107, 186], a gap function g_{N} is defined for each contact pair as

$$g_{\mathrm{N}} = (\mathbf{x}^{\mathrm{s}} - \mathbf{x}^{\mathrm{m}\star}) \cdot \mathbf{n}^{\mathrm{m}\star}, \tag{3.4}$$

where $\mathbf{x}^{\mathrm{m}\star}$ is the orthogonal projection of the contractor node $\mathbf{x}^{\mathrm{s}}$ on the target surface $\mathbf{S}^{\mathrm{m}}$, and $\mathbf{n}^{\mathrm{m}\star}$ is the outward unit normal vector at $\mathbf{x}^{\mathrm{m}\star}$. Here $\mathbf{x}^{\mathrm{m}\star}$ is the solution of a minimum distance problem, which leads to a local Newton iteration for the present problem. From Figure 4.7(II) it is obvious that as a contractor node slides over the boundaries of the B-spline target surfaces (e.g., from $\mathbf{S}_1$ to $\mathbf{S}_2$), the normal vector $\mathbf{n}^{\mathrm{m}\star}$ changes smoothly. This is not the case, when first-order facets are used to represent the target surfaces.

The gap function g_{N} defines the state of contact, and together with the penalty stiffness it

quantifies the contact contribution $\delta W_{\text{ext,c}}$ to the external virtual work, which is given by

$$\delta W_{\text{ext,c}} = \int_{\Gamma_c^s} t_N \delta g_N \mathrm{d}\Gamma_c^s, \tag{3.5}$$

where t_N is the normal contact force and Γ_c^s the contact surface boundary. The residual vector and the stiffness matrix for the finite element implementation of the model are computed by applying the MATHEMATICA package ACEGEN [102]. To this end, several novel techniques such as automatic differentiation and stochastic evaluation of formulas are used. For a detailed description of the developed contact algorithm, the reader is referred to the work by Kiousis et al.[100]

It is worth mentioning, that the employed formulation allows the incorporation of frictional contact. Nevertheless, the simulations are carried out without friction since reliable coefficients describing the frictional behavior between the intimal surface, the balloon catheter and the stent are not yet available.

3.3.2 Finite element discretizations

The 3D geometric models of the four arterial tissues are separately discretized by application of the commercial mesh generation toolkit CUBIT [172]. Approximately 3500 eight-node hexahedral elements are generated in total, and the mixed finite element formulation, as implemented in FEAP, is applied. This approach provides an efficient and proper description of the incompressible deformation of arterial tissues. The meshes are generated with matching nodes on the tissue interfaces, and hence no special algorithmic treatment is required to link them. The generated mesh of the intima also satisfies the requirement of the discussed contact algorithm, i.e. structured quadrilateral facets on the contact surface. The same type of volume elements is chosen for the discretization of the balloon catheter, where 288 elements are generated. Finally, the structure of the stent implies the use of two-node, large displacement, large rotation 3D frame elements [92]. The choice of frame elements over hexahedral elements also leads to less computationally expensive simulations, an important aspect when complex contact problems are to be analyzed.

3.3.3 Boundary conditions

Experience obtained through experimental investigations showed that, in contrast to healthy arteries, highly stenotic human vessels show very little or no axial *in situ* pre-stretch, approximately equal to 1 (a value of 1.03 is reported in reference[83]). Hence, no axial forces or displacements are applied to the artery. The top and bottom faces of the considered artery section are fixed in the axial direction (plane strain condition). The load-free configuration of the arterial wall (shown in Figure 3.1(II)) is also considered stress free, and hence residual strains (stresses) are neglected. Even though the algorithmic concept

for the incorporation of residual stresses exists [168], the lack of experimental data in atherosclerotic lesions makes their consideration not possible in this work. Next, a small value of stiffness is given to each node of the artery. This restricts the rigid motion of the artery. To obtain an almost concentric expansion of the balloon catheter, its nodes located on two orthogonal axial planes are bounded in the circumferential direction. As far as the stent is concerned, the axial displacements are fixed for all the nodes on its midplane, thus, restricting its rigid motion.

3.3.4 Loading procedure

The reference diameter of the chosen catheter and stent is bigger than the diameter of the lumen of the stenotic vessel under investigation. Hence, the undeformed balloon and stent are placed in the lumen with penetration. Next, the penalty parameter which enforces the contact constraint is gradually increased in a few load steps. Thus, the penetration is reduced and the contact between the medical devices and the inner arterial wall is established in a numerically stable way. The expansion of the balloon catheter follows. This is performed by follower pressure loads which are applied on the inner surface of the balloon. As the balloon expands and comes into contact with the stent and the artery. Further increase of the inner balloon pressure leads to the expansion of the three bodies. When the outer diameter of the balloon reaches a desired value, the balloon contact penalty parameter is gradually decreased, simulating the balloon catheter's deflation, and only the plastically deformed stent remains in contact with the inner surface of the vessel.

3.3.5 Indicators for the outcome of angioplasty

Local stress distributions within the specimen during balloon angioplasty and stenting are undoubtedly an important measure to illustrate the changes in the mechanical environment of the vessel wall caused by a particular stent. Nevertheless, if criteria are based on a set of scalar quantities and linked to mechanical measures such as contact forces and stresses, then they could provide a faster and more comprehensive and reliable judgment of the stent-stenosis interaction. The idea to introduce scalar indicators, characterizing the mechanical field of the arterial wall and the lumen change after stenting, was initially proposed in the reference [86], while also applied in [13, 100]. In order to compare the three different stent designs, the same approach is adopted here.

The first introduced indicator characterizes the contact force applied on the intimal surface from the stent's struts. This is an important measure, since elevated contact pressure in the vicinity of the stent struts may lead to injury of the endothelial and medial smooth muscle cells, which may increase the neointimal hyperplasia formation [101]. The indicator of the normalized contact forces at the intimal surface caused by the stent struts is denoted by D_1, and expressed as

$$D_1 = \sum_{i=1}^{n_s} \frac{F_{i,\text{post}}}{l_c}, \tag{3.6}$$

where n_s is the total number of nodes of the stent cell and $F_{i,\text{post}}$ is the norm of the contact force at each stent node after stenting, given by

$$F_{i,\text{post}} = \left(\sum_{j=1}^{3} f_j^2 \right)^{1/2}, \tag{3.7}$$

where f_j are the reaction force components at the node i, and l_c is the total length of the considered stent cell. The indicator D_1 can also be used as a measure for prolapse, hence as a measure for the deflection of tissue between the struts. Prolapse, depends strongly on the artery's (material) composition, the contact forces and the spacing between the stent struts, thus it can be linked to D_1. In addition, prolapse provides an important insight on the effectiveness of stenting since clinical studies relate it with the appearance of restenosis [94].

As aforementioned, a critical factor that drives restenosis is the long-term change of stresses within the arterial wall after the performance of the interventional treatment. High stresses induced by the stent may be responsible for the triggering of growth mechanisms and finally may lead to restenosis [184]. Therefore, a second indicator D_2 is used, able to quantify stress changes in the arterial wall. This indicator is defined as[86]

$$D_2 = \frac{\sum_{i=1}^{n_v} \Delta\sigma_i \Omega_i}{\sum_{i=1}^{n_v} \sigma_{i,\text{MAP}} \Omega_i}, \quad \Delta\sigma_i = \sigma_{i,\text{post}} - \sigma_{i,\text{MAP}}. \tag{3.8}$$

In the above equation, n_v denotes the number of the arterial volume elements and Ω_i the volume of the element i, which is used as a weighting factor. Next, $\sigma_{i,\text{post}}$ and $\sigma_{i,\text{MAP}}$ are the maximum (principal Cauchy) stress in the element i after stenting and under mean arterial pressure, respectively.

The last indicator, denoted by LG (**L**umen **G**ain), corresponds to the lumen change due to stenting. The lumen gain LG is defined as[86]

$$LG = \frac{A_{\text{post}}}{A_{\text{MAP}}} - 1, \tag{3.9}$$

where A_{MAP} is the smallest inner cross-section of the artery before angioplasty and stenting, and A_{post} is the cross-section at the same location as A_{MAP} after angioplasty and stenting.

3.4 Results

In the following section, the most illustrious results of the performed numerical simulations are provided. In particular, the stenting induced stress fields of the arterial tissues

are studied and the performance of the considered stent designs is analyzed using scalar indicators.

3.4.1 Predicted stress fields

The first of the performed simulations concerns the atherosclerotic lesion under internal pressure load. The chosen load is the mean arterial pressure, i.e. taken to be $p_{\mathrm{MAP}} = 13.3\,\mathrm{kPa}$. Note that in this case no initial tears are incorporated since tissue dissection and fissuring are considered to take place at loadings which occur during balloon angioplasty. The stress field in this case is illustrated in Figure 3.4(I). The maximum (principal Cauchy) stresses are given in kPa and are shown for the intima, media and adventitia. As can be seen in Figure 3.4(I), the innermost layer of the lesion is the main load carrier of the structure. This is analogous to inflated thick-wall tubes, where the stress concentration is located at the inner part of the wall. The deformed state, as shown in Figure 3.4(I), is regarded as the pre-stenting reference state, indicated by $(\bullet)_{\mathrm{MAP}}$.

Next, the (small) initial cracks at the intima are considered and the deformed configuration and stress distribution in the arterial tissues under the same loading conditions are studied (Figure 3.4(II)). As previously mentioned, the role of the tears is to incorporate fissuring and dissection of the arterial tissues, which occur during angioplasty interventions [21, 117, 109]. The above simulation aims to model the procedure of balloon angioplasty without stenting. The evolution of the crack tips due to the internal pressure is visible in Figure 3.4(II).

The following step is concerned with the numerical modeling of stenting with reference to the undeformed configuration of the stenotic lesion including the two initial tears. The three different stent designs, as introduced within the section 'Stent models', are used for this purpose. Figures 3.4(III) and 3.4(IV) show the deformed shapes and the resulting stress fields at full balloon inflation and after deflation of the balloon catheter, respectively. Thereby the model of the 'original' (control) EXPRESS VASCULAR LD stent is used. In all cases the balloon is inflated until its outer diameter reaches the value $d_{\mathrm{b,o}} = 4.5\,\mathrm{mm}$, which corresponds to an approximate balloon internal pressure of $p_{\mathrm{b}} = 8\,\mathrm{bar}$. Then, the balloon is removed and only the stent remains in contact with the arterial wall. The slightly smaller lumen area, as shown in Figure 3.4(IV), with respect to Figure 3.4(III), reveals the recoil of the elastoplastic stent. As can be seen in the Figures 3.4(II-IV), the tear of the intima and its dissection from the media, lead to a different stress field (when compared to the condition depicted in Figure 3.4(I)). In the case of balloon angioplasty without and with stenting, the intact intima continues to carry the main part of the load, but the stresses in the adventitia and media increase during and after stenting (especially behind and at the tips of the dissections). In particular, a value of approximately 500 kPa is obtained at both tips at full balloon inflation (Figure 3.4(III)). According to Holzapfel et al. [85], human atherosclerotic plaques of iliac arteries rupture at a stress level similar to that computed here, which additionally justifies the incorporation of the (small) initial cracks. It is interesting to observe that in the diseased part of the intima a stress-shield in form of an arc

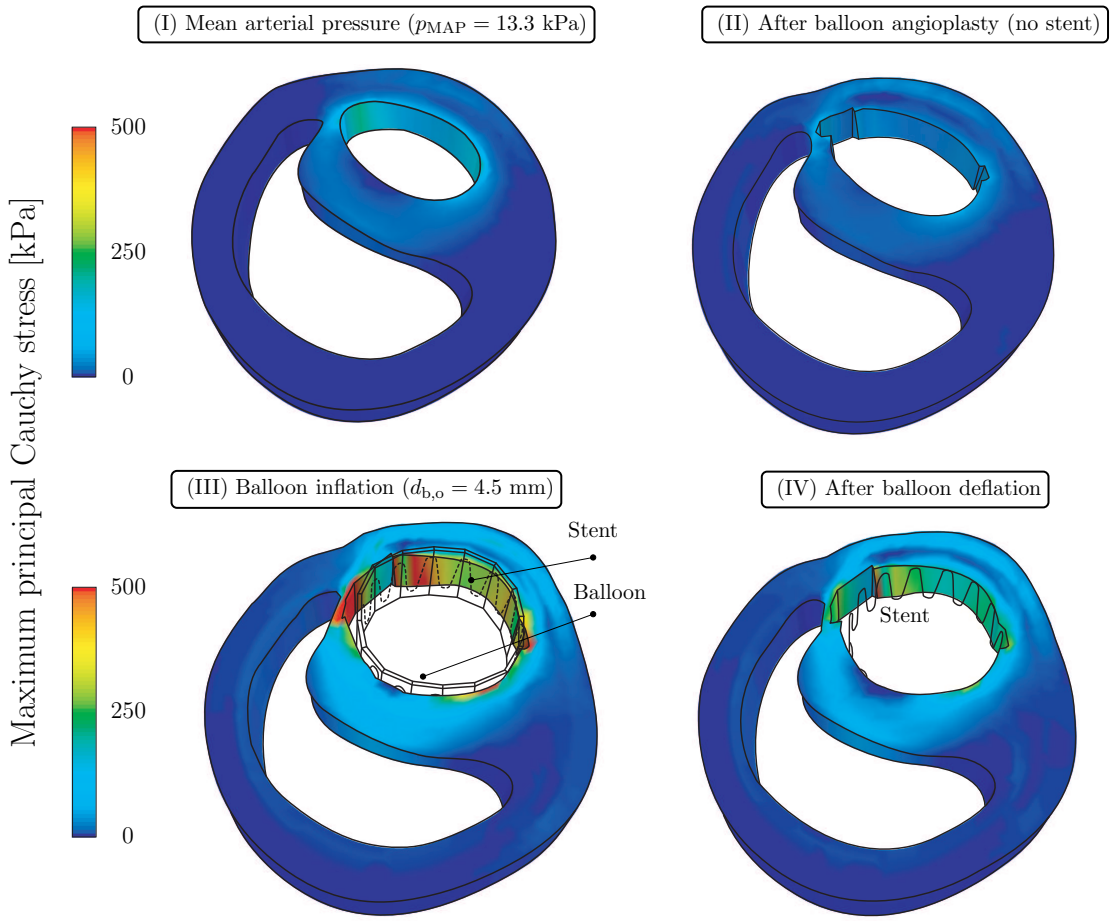

Figure 3.4: Deformed configuration and distribution of the maximum (principal Cauchy) stresses in the arterial tissues (intima, media, adventitia) of an atherosclerotic human iliac artery at different load states: (I) mean arterial pressure ($p_{\mathrm{MAP}} = 13.3\,\mathrm{kPa}$), no initial tears present; (II) balloon angioplasty without stenting; (III) balloon and stent inflation (up to $d_{\mathrm{b,o}} = 4.5\,\mathrm{mm}$); (IV) after deflation of the balloon catheter (only the stent remains in contact with the arterial wall). The lipid pool is not shown.

is present. The acquired results also point out that the lipid pool is under a low compressive hydrostatic pressure. The obtained deformed shapes and stress fields, as illustrated in Figure 3.4(IV), qualitatively and quantitatively agree with the outcome of a recent study [62], where plaque fissuring and dissection during angioplasty were modeled by means of a fracture propagation algorithm based on cohesive zones. However, therein, no stent is used and the analysis does not address contact interactions. Note that for all considered cases the highest stresses were obtained at the introduced crack tip.

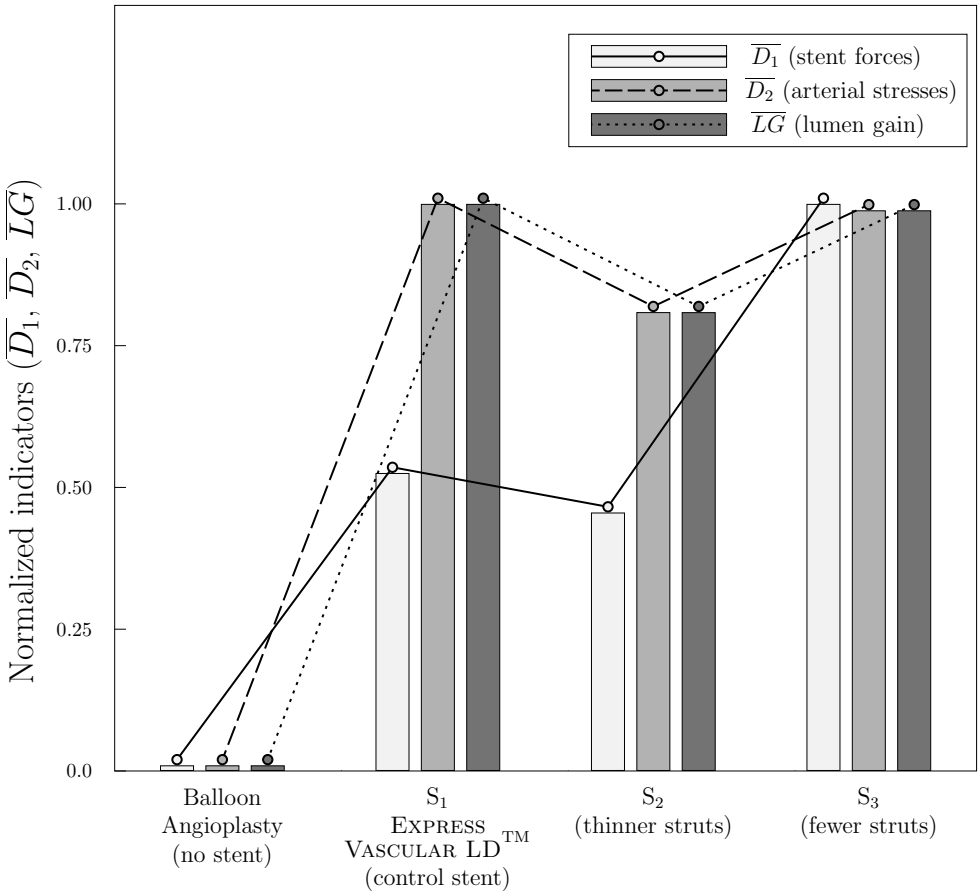

Figure 3.5: Normalized values of the indicators D_1, D_2, LG obtained from the performed simulations. The indicators characterize the stent contact forces, the induced arterial stresses and the gain of lumen area, respectively.

3.4.2 Comparison of different stent designs

At the end of the performed simulations of balloon angioplasty without and with stenting using the three stent designs, the aforementioned indicators D_1, D_2, LG are computed for each case. The obtained values are then normalized (from 0 to 1) according to

$$\overline{\text{ind}} = \frac{\text{ind} - \text{ind}_{\text{min}}}{\text{ind}_{\text{max}} - \text{ind}_{\text{min}}}, \tag{3.10}$$

where 'ind' stands for the indicator D_1, D_2, LG. The quantities ind_{max} and ind_{min} refer to the maximum and minimum values of the related indicator with respect to the four cases, i.e. 'balloon angioplasty (no stent)', 'control stent S_1', 'stent with thinner struts S_2' and 'stent with fewer struts S_3'. From Equation (3.10), it is obvious that $\overline{\text{ind}} = 0$ corresponds to the minimum value of the indicator ind and $\overline{\text{ind}} = 1$ to the maximum value. The normalized indicators $\overline{D_1}$, $\overline{D_2}$, $\overline{LG}$ for each simulation are plotted in Figure 3.5.

As expected, the lowest lumen gain is obtained for the case of balloon angioplasty, where no scaffold is present to keep the elastic artery open ($LG = 18\%$ due to the tears which weaken the structure). Obviously, for this case $D_1 = 0$ since no stent is present. The maximum values for LG are acquired when the control stent S_1 ($LG = 48\%$) and the stent with the fewer struts S_3 ($LG = 47\%$) are used. These two stent designs also lead to the highest values for the indicator D_2, which characterizes (arterial) stress changes. Generally, Figure 3.5 reveals a strong correlation between the indicators LG and D_2. In other words, the induced stresses in the arterial tissues highly depend on the final dilated state of the artery. Among the three stents, the thinner and more compliant stent S_2 results to the lowest values for all three indicators ($LG = 42\%$). A comparison between the stents S_1 and S_2 indicates that by reducing the thickness of the struts by 40%, the achieved lumen gain (LG), the contact forces (D_1) and the (arterial) stress changes (D_2) reduce by approximately 25%. Remarkably, as can be seen in Figure 3.5, stent S_3 shows the highest $\overline{D_1}$ value, hence it generates the highest contact forces on the intimal surface, while at the same time, exhibits comparable values for the indicators $\overline{D_2}$ and $\overline{LG}$ (1% difference) to the control stent S_1, as previously mentioned. This arises from the geometric characteristics of stent S_3, since a stent with fewer struts on its periphery is structurally stiffer than a stent with more struts and the same thickness. In the case of S_3 a bigger prolapse value is also expected due to the larger distance between the struts.

It is clear that the above indicators stand for competing interests. An optimal treatment or stent design should, from a clinical point of view, lead to sufficiently enlarged lumen area (large LG values). At the same time, it should not induce unnecessary arterial trauma, or in other words, should minimize the changes in stresses of the arterial wall and should not apply high contact forces on the intimal surface (small D_1 and D_2 values). The importance of each indicator for an optimization procedure depends on the specific patient and the related patient history.

The results of the simulations performed in this work suggest that the control stent S_1 leads to the most promising results in terms of lumen gain. The same LG can also be accomplished by the use of stent S_3. However, S_3 results in more significant changes in the mechanical environment of the arterial wall expressed through D_1. Consequently, S_3 produces more local damage of the intimal surface due to contact forces, for the same outcome. In the case where a stent design that minimizes arterial damage is more preferable over a stent that maximizes lumen gain, the thinner and more compliant stent S_2 is the most appropriate device among the other two. Stent S_2 leads to lower values of the indicators D_1 and D_2. Accepting that these scalar measures are linked to arterial tissue damage one may assume that stent S_2 is, consequently, less prone to restenosis. This result is comparable with the outcome of clinical studies [97, 135], which identified that thinner struts elicit less angiographic restenosis than thicker struts.

3.5 Discussion and conclusion

A detailed computational model of the arterial wall, the medical devices and their contact interaction is of pressing need and of outmost importance for a deeper understanding of the vessel response under supra-physiological loading as occurring during and after stent placement. The availability of a comprehensive model is also important for the optimization of stent structures, and, therefore, of the interventional procedure which often fails due to biological reactions such as restenosis.

In the present work a methodology was proposed that identifies 'optimal' stent devices. In particular, we presented a numerical framework able to identify the changes in the mechanical environment of atherosclerotic human lesions that occur due to the interaction with vascular stents. We started by discussing the different important modeling aspects of balloon angioplasty with stenting. We analyzed a stenotic iliac artery and modeled it as a solid continuum composed of four types of tissues (adventitia, media, intima, lipid pool). Despite taking into consideration the inhomogeneity of atherosclerotic lesions, several of the identified arterial tissues with different mechanical properties were combined. In a refined attempt the atherosclerotic patient-specific lesion should be analyzed by using more tissue types. The nonlinear elastic response of each tissue was described by a neo-Hookean material relating to the non-collageneous matrix, in addition to an anisotropic free-energy function, which described the response of the collagen fibers [80]. The different sets of material and structural parameters for each tissue were identified by means of *in vitro* uniaxial tensile tests [87]. Residual stresses were not incorporated into the model due to the lack of experimental data on atherosclerotic human iliac arteries. In order to account for the important inelastic effects of the artery at finite deformations such as plaque fissuring and dissipation, two initial tears were introduced into its load-free configuration at locations prone to crack initiation. In addition, the nonlinear, anisotropic mechanical response of the balloon catheter was described by a cylindrically orthotropic model, originally introduced by Kiousis et al.[100] From an industrial partner, the EXPRESS VASCULAR LD iliac stent was acquired and a software tool was developed that allowed the generation of the computer model based on a number of geometric parameters. By application of the same parametrization tool, two more stent designs were obtained, one with thinner struts and one with fewer struts.

The interaction between the medical devices (balloon and stent) and the inner arterial wall was solved as a 3D contact problem. To this end, the robust contact approach documented in the reference[100] was adopted. Each target surface was described by means of C^2-continuous uniform cubic B-spline surfaces, thus avoiding jumps of the normal vectors that would occur during sliding of contacting nodes over linear facet-based discretized surfaces. The nonlinearities arising from the contact interactions and the selected material models lead to computationally expensive simulations. Therefore, in this study only a 3D section of the arterial wall and a stent cell were considered. In order to keep the computational costs as low as possible the smallest cell length ($l_a = 1.4\,\text{mm}$) was used.

One simulation of balloon angioplasty without stent and three simulations of stenting with the aforementioned different stent designs were performed. All computations showed that the incorporation of the tears at the intima led to a different (principal Cauchy) stress environment in the stenosis. In particular, in that case, the mechanical load was carried by the intima, the non-diseased media and the adventitia. However, the highest stresses were reported at the vicinity of the tears, hence the induced trauma due to stenting remained localized at the dissection site rather than spreading over the lesion, which is in accordance with the recent study [62]. It should be noted that the used boundary conditions of the two planar arterial faces affect the stresses in the axial direction. However, after artery dilation the axial stresses are considerably smaller than the circumferential or radial ones, and, therefore, do not particularly influence the study's conclusions. In addition, the artery pressure load during and after stenting was not taken into account since the stresses induced by the stent struts are considered to be much higher than those due to blood pressure. However, in order to study the mechanics of the artery after angioplasty more carefully a refined model should consider the blood pressure.

Next, scalar indicators were defined that allow a judgment on the performance of the used stents and of their interactions with the specific atherosclerotic lesion. These indicators (D_1, D_2 LG) are measures of the contact forces applied from the stent to the intimal surface, of the changes of the mechanical stresses in the individual tissues and of the achieved lumen gain. The results revealed a strong correlation between the lumen gain and the induced stress level. Among the different stent configurations, S_1 and S_3 showed comparable values of the indicators D_2 and LG. Nevertheless, the stent S_3 led to higher values of the contact forces (D_1), being thus possibly a less favorable option for clinicians than the control stent S_1. Finally, the described method indicated that a choice for the most appropriate stent strongly depends on the optimization criterion. In the case that less vascular trauma was regarded as more important than higher lumen area, the performed simulations suggested stent S_2 with the thinner struts as the optimal stent for the lesion under investigation.

Refinements on the geometric and constitutive models have to be considered in future studies. In particular, a larger-scale model should be studied, considering a representative unit length ($a+b+c$) of the stent (see Figure 3.2) or the stent as a whole, and the complete 3D morphology of the artery. A computational analysis on such a basis would lead to local stress concentrations in the non-diseased intima at the stent edges [87], depending on the lesion-morphology and the utilized stent type. In addition, there is plenty of room for introducing other scalar indicators, which characterize the mechanical field of the arterial wall, for example, stress and damage-based indicators. Apart from the mentioned limitations, the proposed physical and numerical models have the ability to provide clear markers for the patient-specific choice of the optimal stent configuration and should be considered as a further step towards computer aided stenting.

4 EXPERIMENTAL STUDIES AND NUMERICAL ANALYSIS OF THE INFLATION AND INTERACTION OF VASCULAR BALLOON CATHETER-STENT SYSTEMS

Abstract—Balloon angioplasty with stenting is a well-established interventional procedure to treat stenotic arteries. Despite recent advances such as drug eluting stents, clinical studies suggest that stent design is linked to vascular injury. Additionally, dilation of the medical devices may trigger pathological responses such as growth and migration of vascular smooth cells, and may be a potent stimulus for neointimal hyperplasia. The purpose of this study is to experimentally investigate the mechanical characteristics of the transient expansion of six commercially available balloon-expandable stent systems, and to develop a robust finite element model based on the obtained experimental results. To reproduce the inflation of stent systems as in clinical practice, a pneumatic-hydraulic experimental setup is built, able to record loads and deformations. Characteristic pressure-diameter diagrams for the balloon-expandable stents and the detached balloons are experimentally obtained. Additionally, typical measures such as the burst opening pressure, the maximum dog-boning and foreshortening, and the elastic recoil are determined. The adopted constitutive models account for the elastoplastic deformation of the stent, and for the nonlinear and anisotropic behavior of the balloon. The employed contact algorithm, based on a C^2-continuous surface parametrization, efficiently simulates the interaction of the balloon and stent. The computational model is able to successfully capture the experimentally-observed deformation mechanisms. Overall, the numerical results are in satisfactory agreement with experimental data.

Keywords—stent; balloon catheter; expansion; constitutive modeling; contact; experiment; finite element method

4.1 Introduction

The latest medical statistics reveal that one out of three Americans has one or more types of cardiovascular disease (CVD) [189]. Similarly, CVDs cause nearly half of all deaths in Europe [137]. CVDs are mostly related to common arterial disorders such as atherosclerosis, which, due to the deposition of fatty substances on arterial walls, reduce the lumen area and decrease the blood flow and the transport of oxygen and nutrients to the organs. An effective and widely-used remedy to treat occluded arteries is balloon angioplasty with stenting. The minimally-invasive nature of this procedure and its remarkably high initial success rate [156, 75] have made balloon angioplasty an attractive therapeutic method. In addition, recently introduced technology to release drugs locally via polymeric-coated

stents has proven remarkably safe and effective in preventing neointima formation, and has reduced short-term rates of restenosis [34, 50, 129, 166, 93].

Nevertheless, the overexpansion of the lesions during angioplasty still induces mechanical injury, which triggers pathological responses such as neointimal hyperplasia [43, 48]. These responses are key factor in in-stent restenosis [19, 73, 131, 103], the most important long-term limitation of stent implantation. It is important to note that the mechanical injury to the vessels is not eliminated by drug-eluting stents.

Balloon angioplasty and stenting is a mechanical solution to a clinical problem. Hence, one may claim that the imposed vascular injury and the resulting restenosis depend on the stent design (structure and material) and the deployment technique, and consequently on the way the medical devices interact with the lesion. Indeed, several clinical studies show the effect of device-dependent factors such as the stent design [145, 101, 122, 167] and deployment technique [74, 101] on tissue proliferation and restenosis. In addition, the review article by Morton et al. [128] summarizes a series of trials and comparative studies which strongly demonstrate that arterial trauma is a function of stent structure and dimensions, i.e., mechanics.

The delicate balance between maximum final stent diameter and minimal arterial trauma, and the elimination of restenosis, has motivated intensive research efforts in the bioengineering community. A majority of studies focus on understanding the mechanical behavior and the optimal clinical function of the balloon-stent system. A few experimental studies [144, 12, 134, 41] provide comparisons of different stents based on physical and mechanical properties such as hoop strength, structural integrity, recoil and flexibility. Two other papers [16, 133] deal with the dilation behavior of balloon-expandable coronary stents and the characteristic nonlinear behavior of the stenting system under internal pressure.

In addition to experimental investigations a large number of finite element approaches exist. The majority of published numerical models focus on the stent's deformation characteristics during expansion [42, 45, 191], and discuss the localized stress regions in the stent structure [25, 40]. Several studies discuss particular features of the behavior of stents such as dog-boning and foreshortening [124, 38]. The documented results are of particular interest as they may be linked to neointima formation. For example, the non-uniform expansion (dog-boning) of the stent is one cause for the injured areas around the stent edges, and the excessive axial contraction of the stent (foreshortening) affects the device positioning and injures the thin endothelial layer.

To our knowledge, very few numerical studies aim to further validate their results with experimental data. The paper by Brauer et al. [16] combines experimental data with numerical analysis, though the agreement is rather poor. The computational study by Migliavacca et al. [126] analyzes the radial expansion and the recoil of coronary stents. The areas of plastic stent deformation are matched to experimental data obtained from scanning electron microscopy. In the numerical model however, the balloon is not considered. A promising study by De Beule et al. [39] documents a numerical model for the dilation of a coronary balloon-stent system, wherein the actual folded shape of the balloon and the

initial crimping of the stent on the catheter are considered. For the balloon, an elastic material model is used. The authors claim strong correlation with the manufacturer's data, and identify that the crimping procedure prior to the stent's expansion has a minor influence on the overall stent behavior. The detailed investigation by Wang et al. [182] focuses on the transitory non-uniform expansion (dog-boning) and foreshortening of six stent models. The balloon is considered to be cylindrical, and it is modeled as an isotropic, linear elastic material. The results indicate that dog-boning depends on the geometry of the stent's distal cells and on the over-length of the balloon. The authors also formulate a semi-quantitative comparison between measurements and simulation; a good match is shown.

The above mentioned studies provide a useful benchmark for the identification and characterization of the balloon-stent expansion characteristics. However, there is still a need for more advanced and efficient models that incorporate the highly nonlinear behavior of the individual components of the system, and the complexity of their contact interaction. Additionally, the validation of these models with pertinent experimental data is crucial.

The present work is a further step in this direction. We start by seeking an understanding of the complex, nonlinear transient inflation of different, commercially available balloon-expandable stent systems on an experimental basis. Then, based on the obtained data, we present a finite element model that is able to reproduce the characteristic inflation mechanism. To this end, cooperations with the Swedish subsidiaries of three industry-leading stent manufactures (BOSTON SCIENTIFIC, CORDIS, MEDTRONIC) are established and six stents, pre-mounted on balloon catheters, are acquired. As part of the experimental investigations, a pneumatic-hydraulic system is built and the deformations of the catheter-stent systems are recorded. Furthermore, mechanical behaviors such as dog-boning, foreshortening and recoil are analyzed. Next, a numerical framework is developed which considers the nonlinearity and anisotropy of the balloon and the elastoplastic deformation of the stent. Three-dimensional interaction between the catheter and the stent is modeled by means of C^2-continuous surfaces. For one of the stents, detailed numerical results of the balloon-stent dilation modeling are presented in terms of pressure-deformation diagrams.

4.2 Experimental study

The goal is to investigate the deformation mechanisms (change in diameter and length) of six sample balloon-expandable stent systems under operational internal pressure that ranges between 0 and 12 bar (the burst pressure was approximately 15 bar). Inflation tests are performed in order to examine for dog-boning and foreshortening. Another goal is to better understand the mechanical behavior of angioplasty balloons under internal pressure loading. For this purpose the balloon catheters are detached from the catheter-stent system, and characteristic deformations are measured. The experimental data will assist in subsequent numerical modeling.

Company	Product	Material	Stent diameter	Stent length
BOSTON SCIENTIFIC	Express Vascular LD	316L SS	9 mm	37 mm
BOSTON SCIENTIFIC	Express Vascular SD	316L SS	7 mm	15 mm
CORDIS	Palmaz Genesis	316L SS	7 mm	12 mm
CORDIS	Genesis Opti Pro	316L SS	7 mm	59 mm
MEDTRONIC	Bridge Assurant	316L SS	6 mm	20 mm
MEDTRONIC	Racer	Cobalt alloy	4 mm	18 mm

Table 4.1: Product details of six balloon-expandable stents.

We provide details of the stent products under investigation and describe the experimental setup and procedure of the balloon catheter-stent inflation. The deformation mechanisms are presented and a comparison between the performance of the different stents and balloon catheters is provided. Finally, we describe the experimental approach to test angioplasty balloons.

4.2.1 Investigated balloon catheter-stent systems

In cooperation with three stent manufactures, BOSTON SCIENTIFIC, CORDIS and MEDTRONIC, six balloon catheter-stent systems were acquired (see Table 4.1). These stents are designed to target peripheral vascular lesions (located, for example, in the aorta or in the renal or femoral arteries) or the bile duct. Each manufacturer supplied two stent types, premounted on the delivery system (balloon catheter, guide wire, introducer sheath). Each set of two stents had a similar geometric shape but differed in dimensions. Figure 4.1 shows photographs of one stent product from each manufacturer in the fully expanded configuration (for clarity). The images were obtained by use of a CCD camera with a magnifying lens.

As can be seen in Figure 4.1, geometric similarities are present among the three stents, for example, the sinusoidal strut structure. In all stents, three main building blocks are present: *unit*, *segment*, and *link*. A segment consists of several units connected circumferentially, while the axially positioned segments are attached by links, leading to the overall stent structure. The three manufacturers' stents have segments of similar shape but different links. More specifically, the stents from BOSTON SCIENTIFIC and MEDTRONIC have straight-shaped links of different lengths, while the stents from CORDIS have s-shaped links. In addition, the Express Vascular LD and the Express Vascular SD have interchanging segments of different lengths with different numbers of units. This is not the case for the other four stent products. All the stents are made of surgical stainless steel 316L, except the Racer stent, which is made of a cobalt alloy (MP35N).

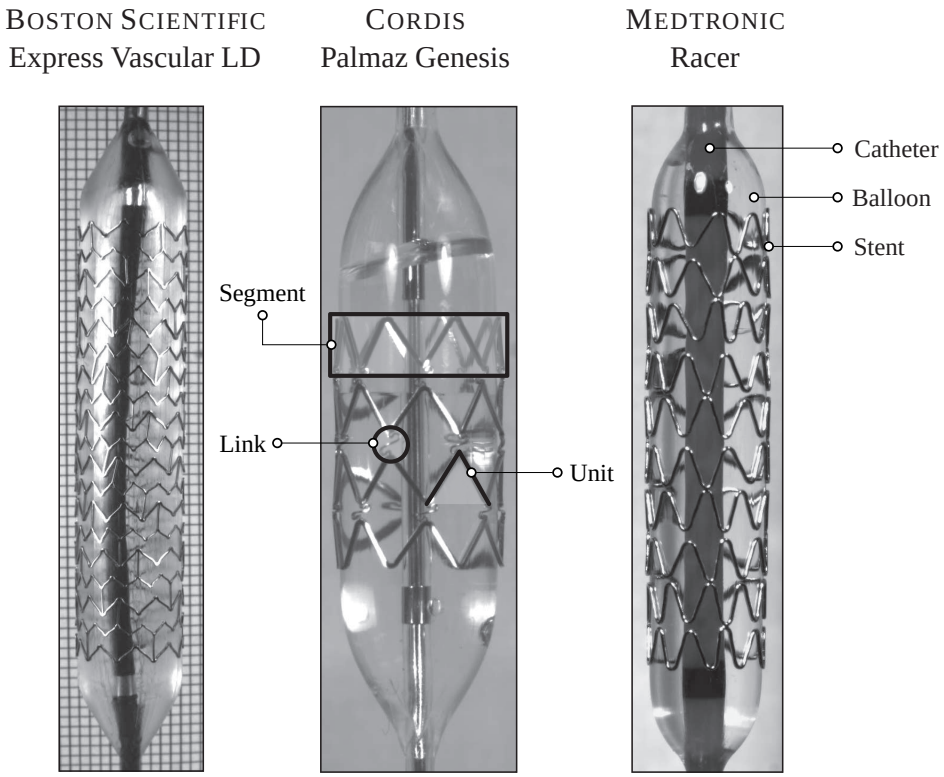

Figure 4.1: Fully inflated configuration of three balloon catheter-stent systems obtained from BOSTON SCIENTIFIC, CORDIS and MEDTRONIC. The parts of the systems (catheter, balloon, stent) and the basic components of the stents (unit, segment, link) are pointed out.

4.2.2 Experimental setup and procedure

The experimental setup accommodates two tasks: (i) the application of a pressure load inside the balloon causing a dilation of the balloon expandable stent, and (ii) the measurement of the load and the related deformation of the catheter-stent system. A schematic representation of the setup is depicted in Figure 4.2. It is a simple, low cost pneumatic-hydraulic system, enhanced by two computer units and a camera.

The first step of the experimental process is concerned with the fixation of the catheter-stent system which is clamped at locations far away from its upper and lower boundaries. This allowed free expansion of the balloon in all three directions (radial, axial, circumferential). In addition the removal of the air from the inflation tube and the balloon catheter is carried out. Sterile water is used as inflation medium and therefore, all air must initially be evacuated from the system. This preparatory task is here performed as in clinical practice. In short, a stopcock along with a syringe are attached to the catheter's inflation port. While the stopcock is open, negative pressure is applied through the syringe. When total vacuum is achieved in the inflation lumen and balloon, the stopcock is closed and the syringe is

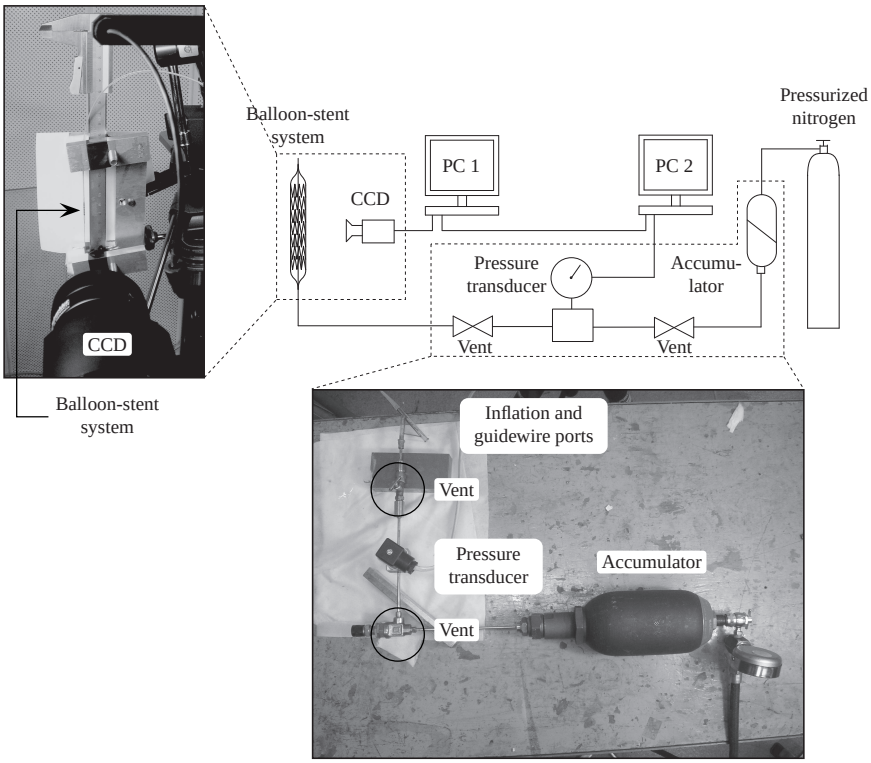

Figure 4.2: Schematic representation of the experimental setup used for the inflation of the balloon-expandable stents and for the recording of the load and deformation. The two photographs show various components of the setup.

removed. The flow of the sterile water into the balloon then takes place and the inflation of the balloon-stent system is initiated.

In order to gradually increase the pressure of the water a compressed gas accumulator is used. One side of the accumulator is connected to a tube containing pressurized nitrogen, while the other chamber of the accumulator contains the hydraulic fluid (sterile water). The two media are separated by an elastic diaphragm. The progressive opening of the regulating vent connected to the gas tube leads to the gradational increase of the water's pressure, constantly measured by a pressure transducer located next to the catheter inflation port. The recording of the transducer is considered equal to the inner balloon pressure, by regarding the hydraulic losses negligible, and is subsequently labeled as p_{b}. The computer unit PC 2 records the input from the pressure transducer (the inflation load) at one second intervals, and simultaneously sends a signal to the computer unit PC 1. Simultaneously, PC 1 triggers a CCD camera equipped with a magnifying lens which takes a photograph of the catheter-stent system under dilation. Three examples of the acquired photographs are given in Figure 4.3, where the deformed configurations of the balloon-stent system at different inner balloon pressures are shown. Image analysis software (Scion Imaging) is employed for a detailed analysis of these data. Information such as the stent's diameter (at different positions, for example, at distal and central segments) and the total length at a specific pressure load is extracted.

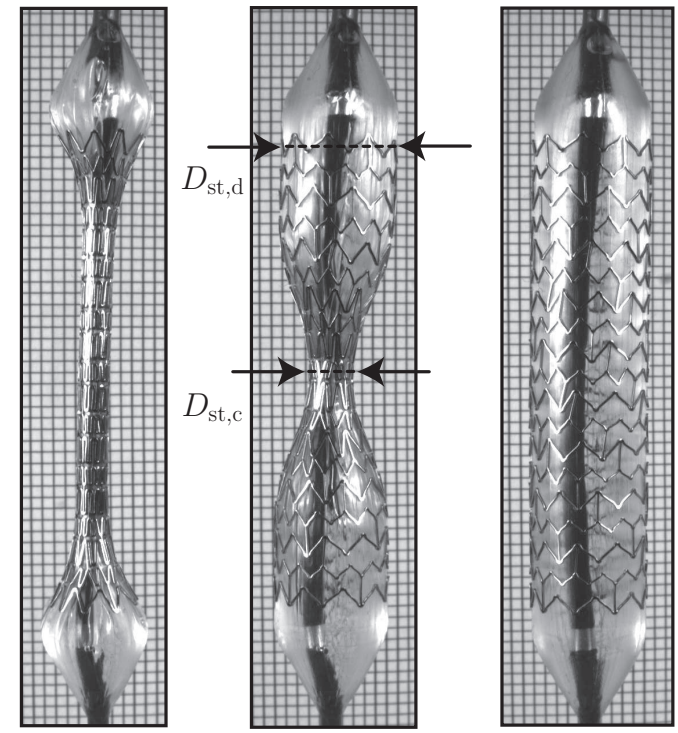

Figure 4.3: Three photographs taken during the inflation of an Express Vascular LD balloon-stent system. The deformed configurations of the balloon-catheter and the stent at three different inner balloon pressures p_{b} are displayed. From these images, and by means of image analysis software, the distal diameter $D_{\mathrm{st,d}}$ and the central diameter $D_{\mathrm{st,c}}$ of the stent were measured in addition to the total length. The dog-boning effect during the inflation of the balloon-expandable stent is clearly visible.

4.2.3 Experimental results

The characteristic pressure-diameter (*p-D*) diagrams (i.e., the change of the stent's diameter with applied pressure load), can be determined for each stent by analyzing the obtained image data. The *p-D* diagrams are a direct and comprehensive source of information concerning the deformation characteristics of the balloon catheter-stent systems. In addition, the diagrams provide an assessment of the different stent products with respect to their mechanical behavior. Figure 4.4 focuses on the Express Vascular LD balloon-stent system. In particular, Figure 4.4(I) shows the gradual change of the inner balloon pressure p_{b} over time t, while Figure 4.4(II) shows the change of the central diameter $D_{\mathrm{st,c}}$ over p_{b} (the $D_{\mathrm{st,c}}$-measure is indicated in Figure 4.3).

The diagrams of Figure 4.4 indicate that the dilation of the Express Vascular LD balloon-stent system can be basically divided into four phases. Initially, as the pressure load starts to act on the inner side of the balloon catheter, the balloon fits closely to the stent. During

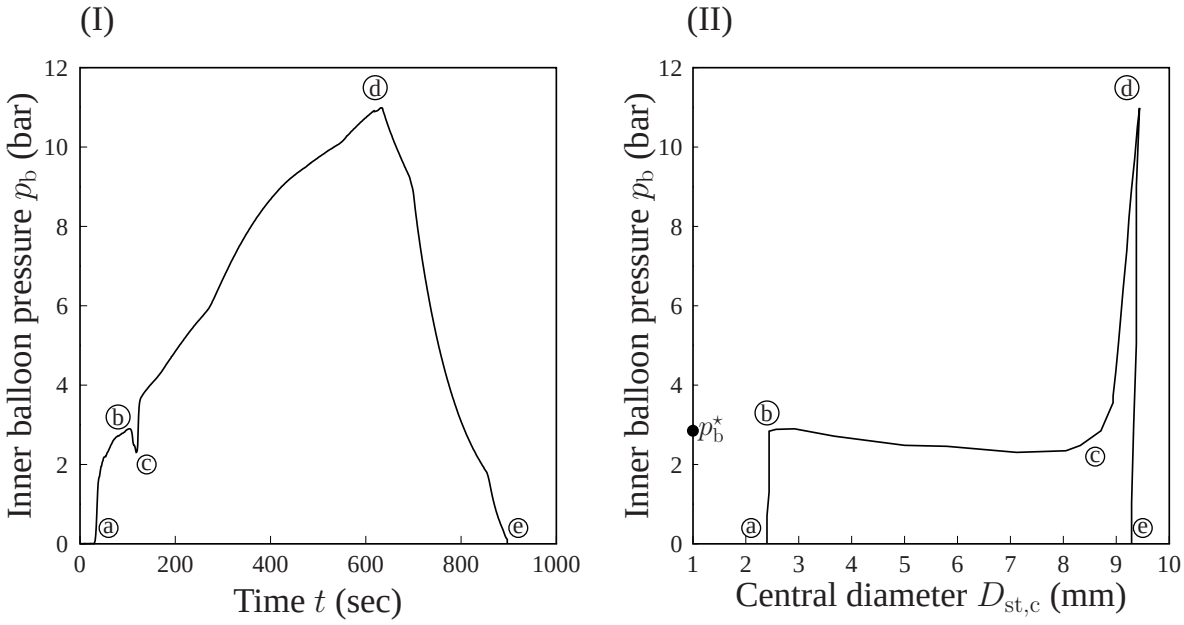

Figure 4.4: Change of the inner balloon pressure p_b over time t during inflation and deflation of an Express LD balloon-stent system (I). Change of the central diameter $D_{st,c}$ of the stent over p_b (II). The deformation mechanism of balloon expandable stents is divided into four stages: ⓐ → ⓑ, balloon fitting and elastic stent deformation; ⓑ → ⓒ, burst opening accompanied with a large dilation rate; ⓒ → ⓓ, circumferential stiffening; ⓓ → ⓔ, load removal and (elastic) recoil.

this phase (ⓐ → ⓑ) the stent deforms elastically and its central diameter $D_{st,c}$ changes only slightly. This is not the case for the distal segments of the stent, where larger deformation is noted at the edges of the stent for the same pressure level ($0 \leqslant p_b \lesssim 3$ bar). This behavior, called dog-boning (or bone effect), is due to a higher compliance at the ends of the stent structure, and is clearly visible in Figure 4.3.

According to Migliavacca et al.[124] dog-boning is defined as the ratio

$$\mathrm{DB} = \frac{D_{st,d} - D_{st,c}}{D_{st,d}} \tag{4.1}$$

(the $D_{st,d}$ is the diameter of the distal segment indicated in Figure 4.3).

When the load reaches a specific limit, say $p_b^\star$ (for the Express LD, $p_b^\star = 2.90$ bar, see Figure 4.4(II)), the stent starts to expand significantly (phase ⓑ → ⓒ), and the stent approaches its nominal diameter in a few seconds. The plateau of Figure 4.4(II) shows this deformation mechanism. The main cause of this rapid expansion, referred to as burst opening, is the initiation of plastic deformation in some stent areas. The slight pressure drop during this phase is a consequence of the burst opening. As expected, when the diameter

of the stent increases, then the volume increases causing a pressure drop. Subsequently, a new phase of deformation takes place (ⓒ → ⓓ), wherein the balloon-expandable stent system stiffens significantly in the circumferential direction. A high pressure increase is recorded against a low stent dilation rate. The main cause of this stiffening behavior is plastic deformation of the stent and, most important, the deformation characteristics of the balloon catheter (as discussed later in the manuscript). Finally, the load is gradually removed (phase ⓓ → ⓔ) and the pressure is reduced to $p_\mathrm{b} = 0\,\mathrm{bar}$. The final diameter of the stent is smaller than its diameter at maximum pressure load. This reduction in size is a result of the stent's elastoplastic deformation and is referred to as *recoil*. The central radial recoil $\mathrm{RE}_\mathrm{c}^\mathrm{rad}$ may be given by the relationship

$$\mathrm{RE}_\mathrm{c}^\mathrm{rad} = \frac{D_{\mathrm{st,c}}^{p_\mathrm{b}^\mathrm{max}} - D_{\mathrm{st,c}}^{p_\mathrm{b}^0}}{D_{\mathrm{st,c}}^{p_\mathrm{b}^\mathrm{max}}}, \tag{4.2}$$

with $D_{\mathrm{st,c}}^{p_\mathrm{b}^\mathrm{max}}$ indicating the diameter of the stent's central segment at maximum pressure and $D_{\mathrm{st,c}}^{p_\mathrm{b}^0}$ is the same diameter after deflation of the balloon. In the case of the Express LD stent, the recoil is approximately 1.5%, and therefore, not readily apparent in Figure 4.4(II).

The mechanical responses of the other five stent products, as can be seen in Figure 4.5, are qualitatively similar to that of the described Express LD system. In particular, Figure 4.5 illustrates the respective changes in the central and distal diameters during the inflation of the six balloon-expandable stent systems. In all cases, the first three deformation phases (ⓐ → ⓑ → ⓒ → ⓓ) are visible. However, in each balloon-stent system a different burst opening pressure is recorded along with a different dilated diameter. A comparison between the distal and central segment clearly evinces the dog-boning effect, indicated by the faster expansion of the stent's edges. More specifically, at the distal segment, in all the cases, the burst opening pressure is approximately half the burst opening pressure of the central segment. A further difference between the central and the distal segment responses concerns the slight pressure drop during the burst opening. In the distal segments, the pressure decreases only just before the stiffening phase, while in the central segment it occurs during its (large) deformation. Note that other studies focusing on coronary stents [16, 182] present similar *p-D* curves to the ones depicted in the left diagrams of Figure 4.5 (for reasons of clarity the unloading paths are not shown).

As was stated in the introduction, two important characteristic mechanisms of stent expansion are dog-boning and foreshortening. Dog-boning is observed in all investigated stents. Based on an Express LD stent, Figure 4.6(I) shows the typical change of the dog-boning DB, according to Equation (4.1), as a function of the inner balloon pressure p_b. The effect becomes clear at a pressure close to the burst opening pressure of the distal segments. When the balloon pressure reaches the value $p_\mathrm{b}^\star \approx 3\,\mathrm{bar}$ (central segment burst opening load) the stent approaches an approximately cylindrical shape and the dog-boning diminishes. At higher pressure loads and after deflation of the balloon catheter, the dog-boning decreases to zero.

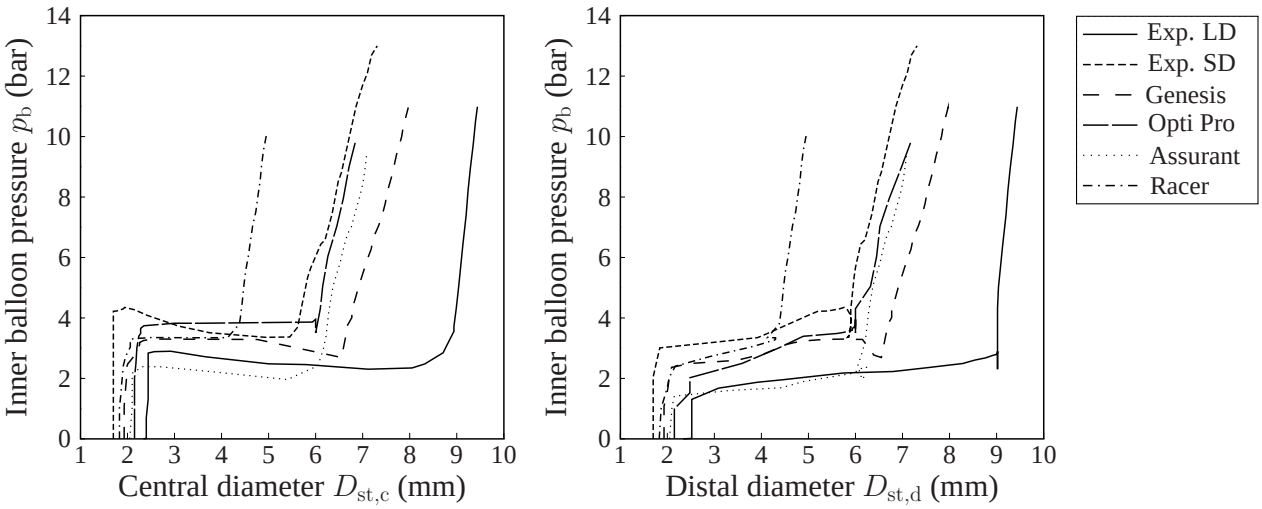

Figure 4.5: Change of the inner balloon pressure p_b versus the central diameter $D_{st,c}$ and the distal diameter $D_{st,d}$ for six balloon-expandable stent systems (compare with Table 4.1). Similar deformation characteristics are identified for all the stent investigated products (three phase expansion), but also noticeable differences, for example, different burst opening loads and final diameters.

The foreshortening mechanism describes the axial contraction of the stent under dilation. Foreshortening may be defined as [124]

$$\mathrm{FS} = \frac{L_{\mathrm{st,defo}} - L_{\mathrm{st,unde}}}{L_{\mathrm{st,defo}}}, \tag{4.3}$$

where $L_{\mathrm{st,defo}}$ and $L_{\mathrm{st,unde}}$ denote the deformed and the undeformed lengths of the stent, respectively. For the case of the Express LD stent, the change of foreshorting FS over inner balloon pressure p_b is depicted in Figure 4.6(II). Due to the cylindrical geometry of the stent and the dog-boning, inflation of the balloon-stent system leads to a decrease in stent length. The shortening reaches its maximum value as the dog-boning reaches its maximum as well (Figures 4.6(I)-(II)), i.e. at the burst opening pressure load of the stent's distal segments. In addition, as the load increases to the stent's operational pressure (≈ 11 bar), the stent elongates from its compressed configuration. Finally, the removal of the pressure load leads to an axial contraction of the stent ($\lambda_z = 0.98$ for the Express LD stent). All stents exhibit negative foreshortening (dilated configuration shorter than the undeformed), except for the Racer stent. A positive value for the foreshortening is noted in this case, meaning that the stent is longer after its circumferential expansion.

In Table 4.2, the burst opening pressure $p_b^\star$, the maximum dog-boning $\mathrm{DB}_{\max}$, the maximum foreshortening $\mathrm{FS}_{\max}$ and the final central radial recoil RE (in percent) are given for each of the six stents. As expected, the Express Vascular LD shows the largest dog-boning due to its larger circumferential stretch relative to the other stents. The Express Vascular SD contracts axially more than any other stent, while, as previously noted, the Racer stent

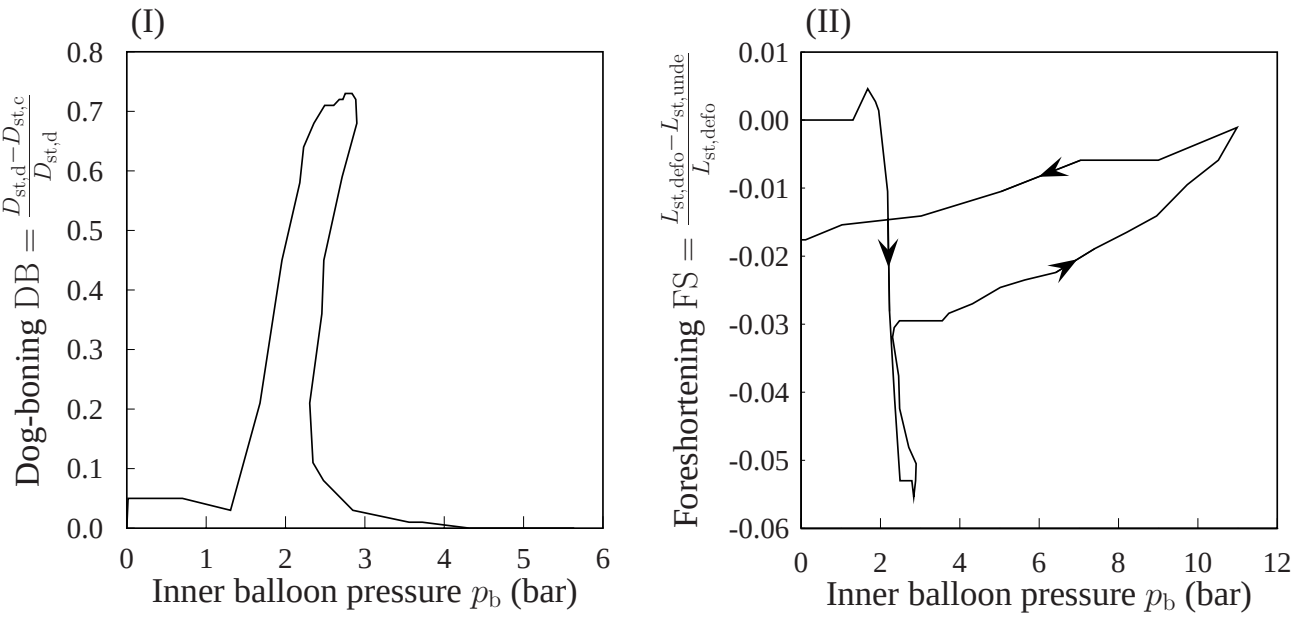

Figure 4.6: Phenomena that occur during the dilation of an Express LD stent: dog-boning DB (I) – the distal diameter $D_{\mathrm{st,d}}$ of the stent expands faster than the central diameter $D_{\mathrm{st,c}}$ until the burst opening of the central segments starts (at $p_{\mathrm{b}}^{\star} = 2.90\,\mathrm{bar}$), and the stent obtains gradually a cylindrical shape; foreshortening FS (II) – during increase of the inner balloon pressure p_{b} the length $L_{\mathrm{st,defo}}$ of the stent initially shrinks. As the stent becomes cylindrical, it elongates, but does not reach its undeformed length $L_{\mathrm{st,unde}}$ in the fully deflated state.

showed the only positive value of foreshortening. In addition, the maximum central radial recoil was measured in the Racer stent when the balloon catheter is removed.

4.2.4 Inflation of balloon catheters

After performing experiments on the complete balloon-stent systems, the balloons are detached from the plastically-deformed, expanded stents, and used for further tests. To perform inflation tests of the detached balloons, the same experimental setup is used. Changes in the length and the diameter of the balloon catheter are recorded during a gradual increase of the inner balloon pressure.

Experimental results reveal a complex deformation mechanism for all six balloon catheters. For example, Figure 4.7 shows the relationship between inner balloon pressure p_{b} and the balloon diameter D_{b} for the balloon catheter obtained from the Bridge Assurant stent system. From this figure, three deformation states of the balloon are evident. Initially, the balloon is folded into an s- or z-shaped form and has an average (reference) diameter $D_{\mathrm{b,I}}$ (state Ⓘ). For this specific balloon catheter $D_{\mathrm{b,I}}$ is assumed to be 2.0 mm. Under low pressures (up to approximately 0.5 bar) the unfolding of the balloon takes place. In this phase, the balloon expands noticeably circumferentially from its initial (complex) configuration, and obtains an almost fully cylindrical shape with diameter $D_{\mathrm{b,II}}$ (state Ⓘ). For the same

Product	$p_b^\star$(bar)	DB_{max} (-)	FS_{max} (-)	RE (%)
Express Vascular LD	2.90	0.73	−0.06	1.5
Express Vascular SD	4.35	0.67	−0.14	1.1
Palmaz Genesis	3.30	0.54	−0.04	3.8
Genesis Opti Pro	3.66	0.62	−0.10	0.1
Bridge Assurant	2.39	0.65	−0.05	4.5
Racer	3.32	0.52	+0.02	5.1

Table 4.2: Experimental results obtained during and after the inflation and deflation of six balloon-expandable stent systems (compare with Table 4.1). The burst opening pressure $p_b^\star$ (in bar) for the central segments of each stent, the maximum values for the dog-boning DB_{max} and the foreshortening FS_{max}, and the elastic recoil RE (in percent) are given.

Bridge Assurant balloon catheter, $D_{b,II}$ is 6.22 mm at state (II). Due to the folded shape of the balloon, its diameter cannot be clearly defined and measured during the phase (I)→ (II). Thus the change of diameter over the pressure load during this phase is not shown in the diagram of Figure 4.7. As the pressure increases to the operational value, small changes are noted in the diameter of the balloon. In other words, after a specific pressure (stretch) limit, the balloon displays a significant circumferential stiffening behavior. At the end of the inflation (state (III)) the diameter of the balloon is $D_{b,III}$ (= 7.57 mm). This diameter also defines the stent's expanded diameter.

A closer examination of the three balloon deformation states ((I), (II), (III)) shows that, despite the prominent circumferential expansion of the balloon, no significant changes take place in the axial direction (see Figure 4.7). Hence, the circumferential compliance of the balloon catheter is higher than that of the axial direction during the inflation procedure. This claim is additionally supported by the curves shown in Figure 4.8, where the inner balloon pressure p_b is plotted against the axial and circumferential stretches λ of the balloon for the phase (II) → (III), at which the balloon is already cylindrical. For the Bridge Assurant balloon catheter it is evident that the stretches in the circumferential direction are higher than in the axial direction, even after the balloon has reached the diameter $D_{b,II}$. The circumferential stretch at state (III) is about 20% higher than that in the axial direction (note that due to the folding mechanism the stretch refers to the whole structure and may not necessarily reflect the stretch in the actual balloon material).

The deformation mechanisms described above are the same for all six balloon catheters, and very similar graphs to the ones in Figures 4.7 and 4.8 are obtained. Nevertheless, each balloon exhibits different diameters $D_{b,II}$ and $D_{b,III}$. For example, for the Bridge Assurant system $D_{b,II} = 6.22$ mm, while for the Express Vascular LD system $D_{b,II} = 8.85$ mm, and for the Palmaz Genesis system $D_{b,II} = 6.35$ mm.

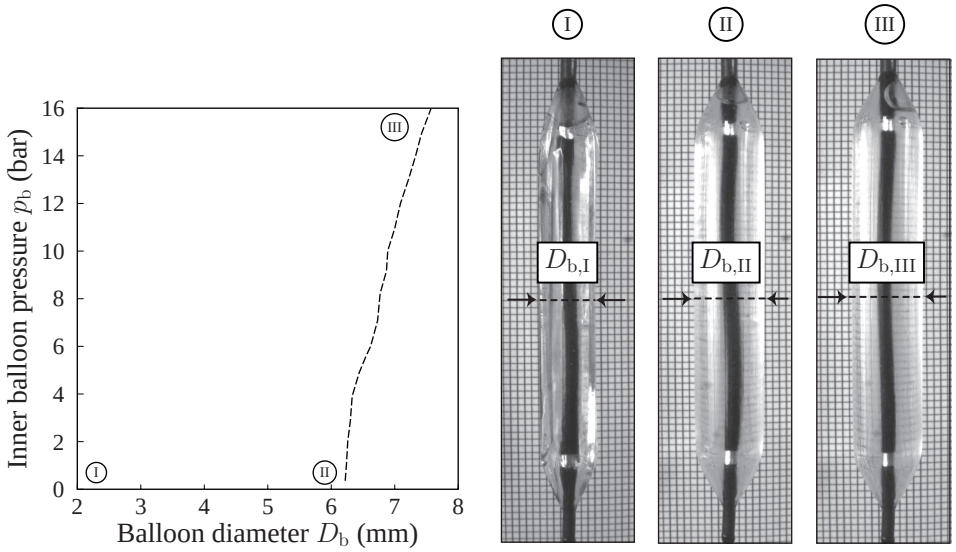

Figure 4.7: Inner balloon pressure p_b versus balloon diameter D_b during the inflation of a balloon catheter used for the Bridge Assurant product, and three photographs of characteristic deformation states of the balloon. Initially, at low pressure load, the folded balloon expands rapidly from its average (reference) diameter $D_{b,I}$ (at 2.0 mm) to a diameter $D_{b,II}$ (at approximately 0.5 bar and 6.22 mm), and obtains an almost fully cylindrical shape (phase Ⓘ → Ⓘⓘ). At the specific diameter $D_{b,II}$, the balloon catheter exposes circumferentially a (relatively linear) stiffening behavior. As the pressure load increases, the balloon slightly continues to expand, up to its final diameter $D_{b,III}$ (phase Ⓘⓘ → Ⓘⓘⓘ).

4.3 Numerical modeling

We present a finite element model for the inflation procedure of balloon catheter-stent systems in more detail and apply the model to analyze the Bridge Assurant system. We outline a parametric algorithm to generate the stent geometry and review a recently proposed cylindrically orthotropic model for the balloon, and an efficient contact algorithm for elastic bodies undergoing large deformations and sliding. The constitutive model for the balloon and the contact algorithm were implemented into the multipurpose Finite Element Analysis Program FEAP[171]. The inputs are material parameters for the balloon material model, and are derived from the inflation experiments described previously. The numerical results are presented in terms of pressure-diameter diagrams, and compared with experimental data.

4.3.1 Stent geometry and material

The six stent geometric models are generated by means of a developed parametrization algorithm. Parametric design is a powerful technique in engineering when numerical optimization is used to generate the ‘optimal’ design of a product. In our case the algorithm

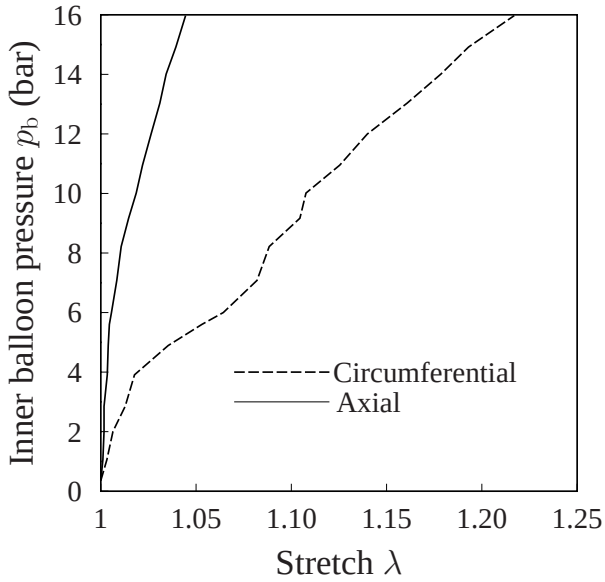

Figure 4.8: Inner balloon pressure p_b over axial and circumferential stretches for a balloon catheter obtained from the Bridge Assurant stent system. The two curves, shown between state ② and ③ (the reference state is state ② where the catheter has obtained an almost fully cylindrical shape), indicate a dominant anisotropic deformation mechanism, which is the same for all six investigated balloon catheters (see Table 4.1).

enables an efficient variation of the stents' configurations and the generation of new stent designs just by varying their geometric structure.

The required input data consists of a set of geometric parameters, which are indicated in Figure 4.9 along with the generated models of the undeformed configurations of three stents. The required geometric parameters are:

(i) number n_u of the units for each segment (could vary among segments of the same stent, as it is the case for the Express stents),

(ii) lengths $l_{u,a}$ and $l_{u,b}$ of the units,

(iii) wave lengths $w_{u,a}$ and $w_{u,b}$ of the units,

(iv) distance $l_{s,c}$ between two consequent segments,

(v) diameter D_{st} and the length L_{st} of the stent.

The output of the parametrization algorithm is the geometric model of the stent and the related finite element mesh. The generated mesh consists of two-node, large displacement and large rotation 3D frame elements [92]. The density of the finite element mesh may be defined by additional user-specified parameters that control the number of nodes in the axial and circular parts of the units, and the number of nodes at the links.

This numerical study focuses particularly on the Bridge Assurant stent system, which is made out of stainless steel 316L. Hence, we adopt a neo-Hookean model for the elastic

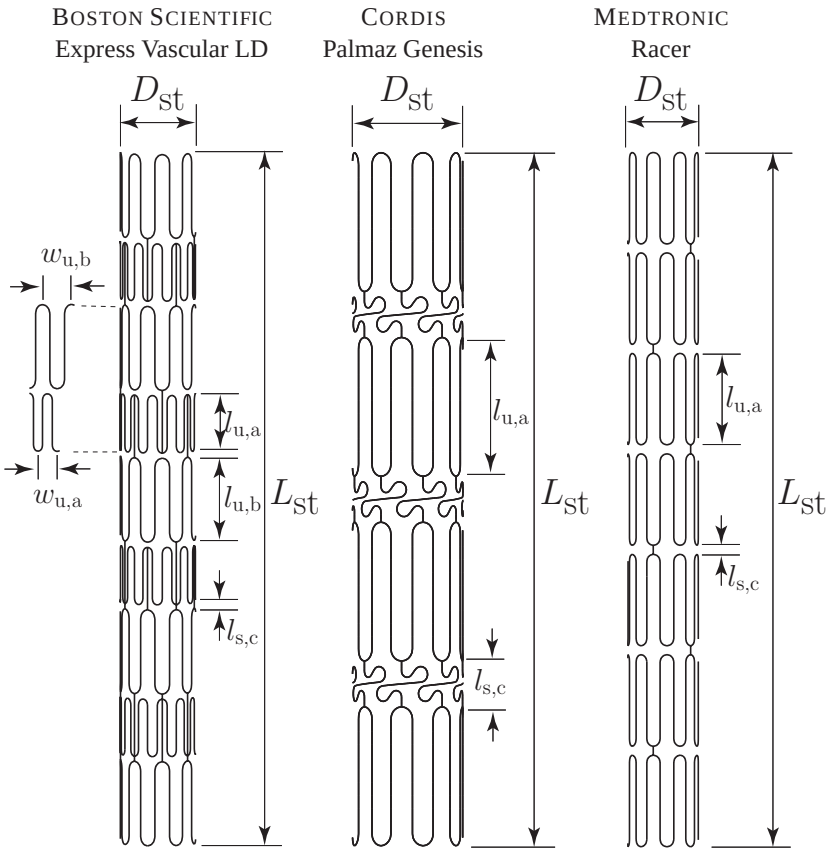

Figure 4.9: Geometric models of the undeformed configurations of three stent products (compare with Table 4.1). The stent geometries are generated by means of a developed parametrization algorithm enabling an efficient variation of the stents' configurations and the generation of new stent designs. The required set of geometric parameters are: the number n_{u}, the lengths $l_{\mathrm{u,a}}$ and $l_{\mathrm{u,b}}$, and the wave lengths $w_{\mathrm{u,a}}$ and $w_{\mathrm{u,b}}$ of the units for each segment, the distance $l_{\mathrm{s,c}}$ between two consequent segments, and the diameter D_{st} and the length L_{st} of the stent.

domain, and the von Mises-Hill plasticity model (J_2 flow theory) with linear hardening for the inelastic domain of the stent material. We choose a Young's modulus $E = 193.0\,\mathrm{GPa}$, a Poisson's ratio $\nu = 0.3$, a yield stress $\sigma_{\mathrm{y}} = 300.0\,\mathrm{MPa}$ and a linear hardening modulus $H_{\mathrm{iso}} = 2.0\,\mathrm{GPa}$ [4].

4.3.2 Balloon geometry and material

The deformation patterns of angioplasty balloons under inner pressure are particularly complex, as is demonstrated by the experimentally observed anisotropic behavior (see Figures 4.7 and 4.8). The balloon's initial folded configuration and the unfolding phase add another degree of complexity to the modeling process. In order to incorporate these

phenomena at least phenomenologically, a cylindrically orthotropic model, as presented in the recent papers by Kiousis et al. [100, 99] is adopted. The model is based on the theory of the mechanics of fibre-reinforced composites, as introduced by Holzapfel et al. [80], and is briefly summarized in the subsequent part of this section.

The folded initial shape of the balloon is not taken into account and the balloon is modeled as a perfect cylinder. The balloon material is assumed to be incompressible and much stiffer axially than circumferentially. According to the experimental data, the mechanical response of the balloon in the circumferential direction is considered to be very soft up to a stretch limit. Beyond this limit the stiffness of the balloon in the circumferential direction increases significantly. In order to capture this peculiar balloon response, two orthogonal material axes are introduced. They are characterized by the unit vectors $\mathbf{a}_{01}$ and $\mathbf{a}_{02}$, which are oriented in the axial and circumferential directions of the undeformed balloon configuration, respectively.

For the balloon material we assume the existence of a strain-energy function defined per unit reference volume, and allow an additive decomposition of that function into volumetric and isochoric parts [76]. While the volumetric contribution is motivated mathematically (described by a penalty function), the isochoric contribution, labeled as $\overline{\Psi}$, is now described in more detail. We assume a separation of $\overline{\Psi}$ into an isotropic part $\overline{\Psi}_{\text{iso}}$, associated with the deformation of the matrix material, and an anisotropic part $\overline{\Psi}_{\text{aniso}}$, which takes care of the anisotropic behavior of the balloon response. The two-term potential may be written as

$$\overline{\Psi}(\overline{\mathbf{C}}, \mathbf{a}_{01}, \mathbf{a}_{02}) = \overline{\Psi}_{\text{iso}}(\overline{\mathbf{C}}) + \overline{\Psi}_{\text{aniso}}(\overline{\mathbf{C}}, \mathbf{a}_{01}, \mathbf{a}_{02}), \tag{4.4}$$

where $\overline{\mathbf{C}} = J^{-2/3}\mathbf{F}^{\mathrm{T}}\mathbf{F}$ is the modified right Cauchy-Green tensor, $J > 0$ is the local volume ratio, and $\mathbf{F}$ is the deformation gradient [76]. By introducing the structure tensors $\mathbf{A}_1 = \mathbf{a}_{01} \otimes \mathbf{a}_{01}$ and $\mathbf{A}_2 = \mathbf{a}_{02} \otimes \mathbf{a}_{02}$, Equation (4.4) may be written in the reduced form [80]

$$\overline{\Psi}(\overline{\mathbf{C}}, \mathbf{A}_1, \mathbf{A}_2) = \overline{\Psi}_{\text{iso}}(\bar{I}_1) + \overline{\Psi}_{\text{aniso}}(\bar{I}_4, \bar{I}_6), \tag{4.5}$$

with the first invariant $\bar{I}_1 = \mathrm{tr}\overline{\mathbf{C}}$ of $\overline{\mathbf{C}}$, and the two invariants $\bar{I}_4 = \overline{\mathbf{C}} : \mathbf{A}_1$ and $\bar{I}_6 = \overline{\mathbf{C}} : \mathbf{A}_2$ of $\overline{\mathbf{C}}$, $\mathbf{A}_1$ and $\overline{\mathbf{C}}$, $\mathbf{A}_2$, respectively. The invariants $\bar{I}_4$ and $\bar{I}_6$ are the squares of the stretches in the directions of $\mathbf{a}_{01}$ and $\mathbf{a}_{02}$, respectively, and therefore have a clear physical interpretation. From the above equation it is obvious that anisotropy arises only due to $\bar{I}_4$ and $\bar{I}_6$.

The isotropic response of the matrix material is determined through a neo-Hookean model of the form $\overline{\Psi}_{\text{iso}} = \mu(\bar{I}_1 - 3)$, where $\mu > 0$ is a stress-like material parameter. The anisotropic contribution $\overline{\Psi}_{\text{aniso}}$ to the strain-energy function is described as [100]

$$\overline{\Psi}_{\text{aniso}}(\bar{I}_4, \bar{I}_6) = \sum_{i=4,6} \frac{d_{1,i}}{n}(\bar{I}_i - d_{2,i})^n. \tag{4.6}$$

The parameters n and $d_{2,i}$, $i = 4, 6$, are dimensionless, while $d_{1,i}$, $i = 4, 6$, have dimensions of stress. With this function, the stiffness in each direction is described by $d_{1,i}$, while $d_{2,i}$ defines the initiation of the balloon's stiffening behavior (axially and circumferentially).

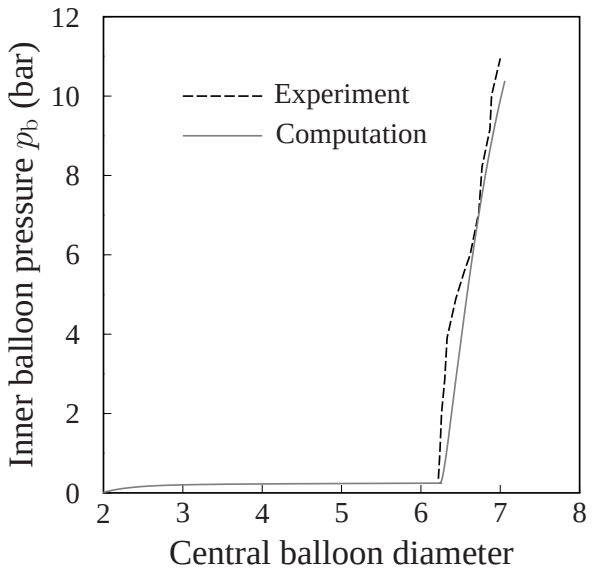

Figure 4.10: Experimental results in comparison with results obtained from a finite element simulation of the dilation process of the Bridge Assurant balloon analyzed with the material model (4.6). Inner balloon pressure p_b versus central balloon diameter. Up to about $p_b = 0.5$ bar the balloon diameter increases considerably and beyond that pressure the balloon stiffens circumferentially. The computational model shows good agreement with the experiments.

To illustrate the accuracy of the described material model, a numerical analysis of the Bridge Assurant balloon catheter is performed and compared with the experimental data. The diameter and length of the balloon in the undeformed configuration are assumed to be 2.0 mm and 20.0 mm, respectively. The balloon is discretized by eight-node hexahedral elements. In order to account for incompressibility a mixed finite element formulation is used. The upper and lower faces of the balloon are fixed in all directions. The expansion of the balloon catheter is performed by a pressure load, which acts at the deformed inner boundary surface of the balloon, and which is deformation dependent. In order to match the characteristic mechanical response, the parameter $d_{2,4}$ is chosen equal to 1. In the case of the Bridge Assurant balloon, the diameter $D_{b,II}$ at state Ⓘ is 6.22 mm, which corresponds to a circumferential stretch of 3.11. The value $d_{2,6}$, describing the initiation of the stiffening in the circumferential direction, is chosen equal to 10, and the exponent in Equation (4.6) is 3. The stiffness in the two material axes of the balloon is defined by the values $d_{1,4} = 1000$ N/mm and $d_{1,6} = 100$ N/mm respectively, while for the isotropic part $\mu = 100$ MPa. Figure 4.10 illustrates the results of the finite element simulation of the dilation process of the Bridge Assurant balloon. The solid curve represents the change of the inner balloon pressure p_b with the central diameter of the balloon. As depicted in Figure 4.10, between load $p_b = 0$ bar and $p_b = 0.5$ bar, the balloon diameter increases considerably. This phase (Ⓘ → Ⓘ) simulates the complex unfolding of the balloon. After this phase, at state II, the balloon stiffens circumferentially. In Figure 4.10 the experimental results are illustrated by a dashed curve. As can be seen, the numerical model captures

qualitatively and quantitatively the experimentally observed deformation mechanism of the balloon catheter.

4.3.3 Contact between the stent and the balloon

The numerical simulation of the interaction of the stent with the balloon is a challenging nonlinear problem in computational mechanics. The main difficulties arise from the nonlinear behavior of the involved bodies, the anisotropy of the balloon catheter, the involved finite deformations and the complex three-dimensional contact interaction of the two medical devices. There is strong evidence that facet-based contact algorithms often lead to numerical problems during simulations where large deformations and bodies with arbitrary geometries are involved [44, 161]. Problems encountered include: oscillation of contact forces, non-realistic pressure jumps, contact cycling and loss of quadratic convergence of the nonlinear solution scheme.

In order to overcome these numerical instabilities the contact algorithm developed and documented in Kiousis et al. [100] is adopted here. In this context, the stent is considered as the contractor and the balloon as the target body. By applying the node-to-surface approach the stent is described through its (finite element) nodes and the balloon by C^2-continuous surfaces. While several parametrization methods have been implemented into contact algorithms [136, 161, 160], the discussed technique makes use of uniform cubic B-splines surfaces [138] mathematically described as

$$\mathbf{S}(u,v) = \sum_{i=1}^{4}\sum_{j=1}^{4} B_i(u)B_j(v)\mathbf{P}_{i,j}, \qquad 0 \leq u,v \leq 1, \tag{4.7}$$

where u and v are convective coordinates, $\mathbf{P}_{i,j}$, $i,j = 1,\ldots,4$ is a structured, bidirectional mesh of 4×4 control points, and $B_k, k = 1,\ldots,4$ are cubic basis functions of the form

$$\begin{aligned} B_1(t) &= (1-3t+3t^2-t^3)/6, \\ B_2(t) &= (4-6t^2+3t^3)/6, \\ B_3(t) &= (1+3t+3t^2-3t^3)/6, \\ B_4(t) &= t^3/6, \end{aligned} \tag{4.8}$$

where t stands for u or v. In the present approach, the control points $\mathbf{P}_{i,j}$ are formed by the superficial element nodes of the target body, i.e., the balloon. The uniform cubic B-splines have useful properties such as C^2-continuity and local support, and the normal vector changes smoothly over the boundaries of surfaces. Therefore, the application of uniform cubic B-splines leads to a robust contact algorithm. For more details on the implementation of the parametrization scheme into a numerical framework (especially into FEAP [171]), the reader is referred to the original work by Kiousis et al. [100].

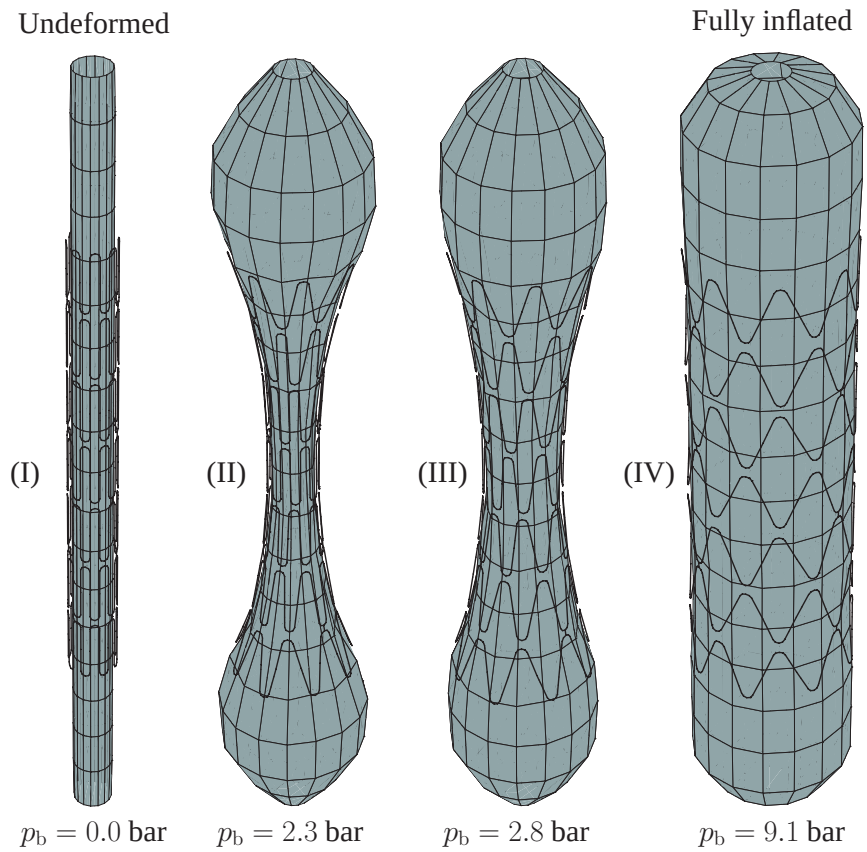

Figure 4.11: Finite element model of the Bridge Assurant balloon catheter-stent system (I). Deformed configurations of the system at different pressure levels (II), (III), (IV) (the upper and lower faces of the balloon are fixed in all directions, and pressure boundary loading is applied at the inner surface of the balloon). The numerical model successfully reproduces the experimentally observed deformation mechanisms, for example, the dog-boning (compare with Figure 4.3).

4.3.4 Finite element model of the balloon catheter-stent system

Figure 4.11(I) shows the finite element model of the Bridge Assurant balloon catheter-stent system. The total number of degrees of freedom is approximately 6000. The upper and lower faces of the balloon are fixed in all directions. To each node of the stent an axial stiffness is added. This restricts axial rigid motion at the nodes and, in addition, incorporates (a phenomenological) friction between the inner side of the stent and the outer surface of the balloon. Friction was not explicitly implemented because a reliable friction coefficient is not yet known. The pressure boundary loading is applied at the inner surface of the balloon. The gradual increase of the inner pressure inflates the balloon, which comes into contact with the stent, and consequently, leads to full expansion of the system. The contact constraint is enforced by the penalty method.

4.3.5 Numerical results of the inflation process

Figures 4.11(II)-(IV) show results of the finite element simulation in terms of the deformed configurations of the Bridge Assurant balloon catheter-stent system at three load levels during inflation process. The computation points out that the distal cells of the stent are more compliant than the central cells, which is in agreement with experimental observation (the edges of the stent expand faster than the central region, i.e., dog-boning, see Figures 4.11(II)-(III)). More specifically, for $p_\mathrm{b} = 2.3\,\mathrm{bar}$ (Figure 4.11(II)) the cell in the central region of the stent is almost unexpanded, since the pressure load has not yet reached the burst opening value, which is at $p_\mathrm{b}^\star = 2.39$ for the Bridge Assurant system (see Table 4.2). Meanwhile, the distal segments have acquired a significantly larger diameter. As the pressure load increases (Figure 4.11(III)), the central segment expands, and at $p_\mathrm{b} = 9.1\,\mathrm{bar}$ (Figure 4.11(IV)) the stent obtains its fully expanded cylindrical shape.

In order to validate the accuracy and efficacy of the employed finite element model and the contact algorithm, we compare the pressure-diameter diagrams obtained from the experiments and the numerical simulation (see Figures 4.12(I) and (II)). Overall, the numerical results (solid curves) are in satisfactory agreement with the experimental data (dashed curve, from Figure 4.5). The computation is able to precisely capture the initial expansion phase ⓐ → ⓑ of the balloon-expandable stent system for both the central and the distal diameter of the system. In addition, the numerical results for the distal diameter of the system during the dilation phase ⓑ → ⓒ agree also quite well with the experimental data. This is not the case for the central diameter because Newton iterations are used to solve the algebraic equations. One possible modification to improve the accuracy of the simulation (according to the experimental results of the central system diameter during dilation phase) is the application of an arc-length method. Thereby, a length of a specified load-displacement path may be provided instead of a pressure load step.

At the final phase ⓒ → ⓓ of the system's inflation, where the balloon stiffens circumferentially, the numerical model demonstrates a slightly stiffer behavior when compared to the experimental data for the region $p_\mathrm{b} \in [5, 10]\,\mathrm{bar}$ (about 7 % difference). A closer review of Figure 4.5 (experimental results) reveals that several balloon-stent systems demonstrate two stiffening regions within the phase ⓒ → ⓓ, which is clearly visible for the Bridge Assurant system in Figure 4.12. It is apparent that at a pressure load of about $p_\mathrm{b} = 5.0\,\mathrm{bar}$, a transition of the balloon-stent's circumferential stiffness takes place and the overall system becomes more compliant. The numerical model, while able to track the initial experimental results, is not able to mimic this transitional zone of the (circumferential) stiffness.

4.4 Summary and conclusion

The present study analyzed the mechanical response of six vascular balloon catheter-stent systems, and of angioplasty balloons detached from the catheter-stent systems, during inflation. The analysis was initially approached from an experimental point of view. Next,

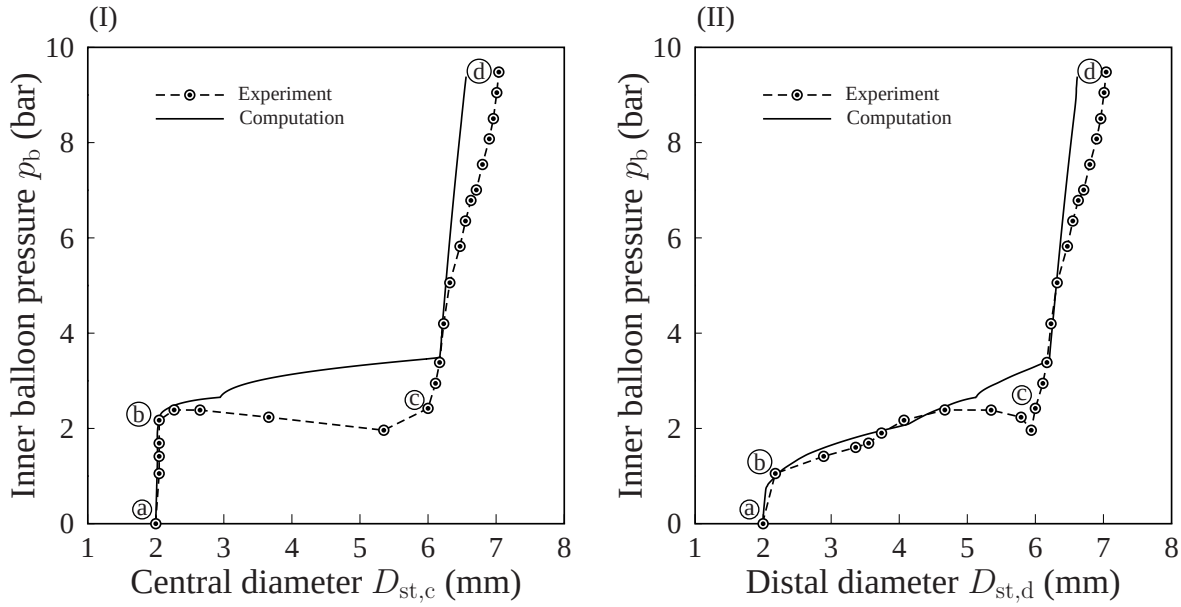

Figure 4.12: Comparison of the experimental and the numerical results for the dilation of the Bridge Assurant balloon-stent system; change of the inner balloon pressure p_b versus the central diameter $D_{st,c}$ (I), and the distal diameter $D_{st,d}$ (II). Overall, the numerical results (solid curves) are in satisfactory agreement with the experimental data (dashed curve, from Figure 4.5).

guided by the experimental data, a finite element framework was developed which is able to reproduce the typical mechanical characteristics of catheter-stent systems.

Cooperations were established with three stent manufacturers, and six current stent products were acquired (product details are summarized in Table 4.1). After recording the stent structures and dimensions, the balloon-stent systems underwent inflation tests. A pneumatic-hydraulic experimental setup was built (Figure 4.2) to apply pressure inside the balloon catheters, while simultaneously recording the loads and deformed states of the balloon-expandable stents during inflation. Postprocessing of the experimentally obtained data and images (shown for example for an Express Vascular LD balloon-stent system in Figure 4.3), made it possible to extract the characteristic pressure-diameter diagrams for each stent (Figures 4.4 and 4.5). These images and diagrams reveal that during inflation of the balloon-stent systems, the overall deformation path can be sub-divided into three characteristic phases, and that phenomena such as dog-boning and foreshortening take place (Figure 4.6). Table 4.2 summarizes additional important information including the burst opening pressure, the maximum dog-boning and foreshortening values, and the elastic recoil.

In order to acquire a more thorough understanding of the mechanical behavior of modern balloon catheters (detached from the stents), the same experimental setup and protocol were used. Findings underline an almost bi-linear and anisotropic deformation mechanism, which is the same for all investigated balloon catheters (Figures 4.7 and 4.8). The

balloons showed significant axial stiffness during the inflation, while in the circumferential direction they were very compliant (unfolding phase) for pressure levels between 0 and approximately 0.5 bar. However, at higher pressure loads pronounced stiffening occurred.

Subsequently, a finite element model for simulating inflation of the balloon and its interaction with the stent was presented, focusing on the the Bridge Assurant stent system. A parametrization algorithm was developed to generate geometric models of the undeformed stent configurations (see Figure 4.9). Deformation of the stent was taken into consideration by an elastoplastic material model. In order to describe the unfolding process of the balloon, and the circumferential stiffening behavior in a phenomenological way, a nonlinear anisotropic model was adopted [98, 99]. The computational model for the balloon was shown to be in good agreement with the experimental results (Figure 4.10). The contact interaction of the two bodies was modeled by means of a contact algorithm based on a uniform cubic B-spline surface parametrization. The penalty method was applied to impose the contact constraint. The finite element model reproduced the experimental data in a robust way (Figure 4.11). Comparative study showed good agreement between the pressure-diameter diagrams generated form the experimental data and the simulation (Figure 4.12). The model successfully captured the mechanics of the balloon-stent system under dilation. However, it should be noted that the pressure drop during the burst opening phase could not be captured by the applied numerical methodology.

The proposed experimental and computational approach demonstrated suitability for better analyzing commercially available vascular balloon catheter-stent systems, and also developing new stent designs. The presented methodology identified stents with maximum values of dog-boning and foreshortening. Even though a direct comparison of these specific products was not feasible (since the stents are of different sizes and target lesions of different diameters and lengths), the computational model can serve as a test bed for new stent geometries. New designs can *a priori* be tested in this numerical platform, and can be evaluated in terms of final expansion diameter, dog-boning or foreshortening. In such a way, the presented model can be a valuable tool for stent manufacturers. In addition, studies of the morphologic changes in lesions during *in vitro* angioplasty using certain imaging modalities and image processing[7] and/or experimentally-validated models for the interaction with a lesion [86, 106, 114, 99] can assist the development of accurate and reliable patient-specific simulations. In this way, more information on arterial damage can be provided in the future.

However, there are still limitations that should be addressed in the near future. The presented study did not consider the interaction of the medical devices with the vascular wall. The balloon-stent systems were not tested in the application environment, i.e., inside an atherosclerotic arterial wall. The design of such an experiment could provide information on the damage induced by the stent struts on the endothelial layer. Such an attempt however exceeds the aims of the current work. Crimping of the stent to the balloon catheter was not simulated, and hence the residual stresses and strains resulting from this procedure were not considered. It is noted, however, that the results of the recent computational study by De Beule et al. [39] show that the crimping procedure has a minor influence on

the overall expansion of the stent. The undeformed configuration of the balloon catheter is considered to be uniform and cylindrical, and its folded shape is not modeled. However, the adopted nonlinear model manages to successfully simulate the unfolding phase of the balloon in a phenomenological way. In addition, the presented computational model did not incorporate microstructural effects of the stent. The average grain size of stainless steel is almost of the same order of magnitude as the stent's strut thickness (approximately $150\,\mu$m). Therefore, a continuum mechanical model may be questionable. Note that the paper by McGarry et al. [120] analyzes micro-scale mechanical phenomena of the stent material behavior using physically based crystal plasticity theory rather than phenomenological plasticity theory.

We hope, despite of the mentioned limitations, that this analysis assists the biomechanics and medical community in future numerical investigations towards optimization of the stenting technique.

5 A METHODOLOGY TO ANALYZE CHANGES IN LIPID CORE AND CALCIFICATION ONTO FIBROUS CAP VULNERABILITY: THE HUMAN ATHEROSCLEROTIC CAROTID BIFURCATION AS AN ILLUSTRATORY EXAMPLE

Abstract— A lipid core that occupies a high proportion of the plaque volume in addition to a thin fibrous cap are predominant indicators of plaque vulnerability. Nowadays, noninvasive imaging modalities can identify such structural components, however, morphological criteria alone cannot reliably identify high-risk plaques. Information such as stresses in the lesion's components seems to be essential. This work presents a methodology able to analyze the effect of changes in the lipid core and calcification on the wall stresses, in particular on the fibrous cap vulnerability. Using high-resolution MRI and histology, a patient-specific 3D geometric model of a human atherosclerotic carotid bifurcation consisting of four tissue components is generated. The adopted constitutive model accounts for the nonlinear and anisotropic tissue behavior incorporating the collagen fiber orientation by means of a novel and robust algorithm. The material parameters are identified from experimental data. A novel stress-based cap vulnerability index is proposed to assess quantitatively the rupture-risk of fibrous caps. Nonlinear finite element analyses identify that the highest stress regions are located at the vicinity of the shoulders of the fibrous cap and in the stiff calcified tissue. A parametric analysis reveals a positive correlation between the increase of lipid core portion and the mechanical stress in the fibrous cap, and hence the risk for cap rupture. The highest values of the vulnerability index, which correlate to more vulnerable caps, are obtained for morphologies for which the lipid cores were severe; heavily loaded fibrous caps were thus detected. The proposed multi-disciplinary methodology is able to investigate quantitatively the mechanical behavior of atherosclerotic plaques in patient-specific stenoses. The introduced vulnerability index may serve as a more quantitative tool for diagnosis, treatment and prevention.

Keywords— artery; calcification; carotid bifurcation; fibrous cap; lipid core; MRI; vulnerability

5.1 Introduction

Atherosclerosis is the main determinant of cardiovascular diseases, the leading cause of cardiovascular morbidity and mortality around the globe [3, 148]. Although luminal narrowing and exaggerated or anomalous vasoconstriction contribute to some of the clinical manifestations of arterial diseases, it is the superimposition of an arterial thrombus over an

underlying ruptured or eroded plaque that is responsible for the vast majority of acute ischemic syndromes such as myocardial infarction or cerebrovascular accident [179, 31, 20]. Therefore, the ability to identify rupture-prone, high-risk plaques and to intervene successfully before acute plaque rupture occurs, has been an elusive goal of clinicians over the last decades.

A series of post-mortem observations in patients with acute ischemic syndromes revealed that predominant features of plaque vulnerability include increased numbers of macrophages, increased expression of tissue factor, reduced number of smooth muscle cells, a lipid core that occupies a high proportion of the overall plaque volume, and a thin fibrous cap (see, e.g., [46, 33, 127]). The rapid development in the area of arterial wall imaging made the detection of the lipid core and the fibrous cap feasible. A review of the invasive and non-invasive imaging modalities is given in [51]. High-resolution magnetic resonance imaging represents the best promise of *in vivo* quantitative characterization of plaque morphology [192, 193, 176], and appears to be a favorable assessment method of fibrous caps and a promising diagnostic strategy.

Plaque rupture is highly complex, multi-factorial, and morphological criteria alone cannot reliably identify high-risk plaques. Early studies based on structural mechanics [143, 116, 23], identified a strong connection between plaque fracture and mechanical loading through blood pressure. It was especially shown that large, eccentric lipid cores impose a mechanical disadvantage to the plaque by redistributing circumferential stress to the shoulders' regions of the plaques; hence to the location where fibrous caps in most cases tend to rupture [17]. These investigations provided strong evidence that acute plaque fracture is linked to plaque composition and to high mechanical stresses which exceed the ultimate tensile strength of the fibrous cap. Thus, it is now accepted that computational mechanics in addition to imaging is necessary for the assessment of the lesions' vulnerability.

Therefore, in recent years more attempts came from the biomechanics community by applying numerical tools in conjunction with imaging modalities such as MRI and IVUS to provide deeper insights on plaque fracture. Several studies support the interrelation between the tissue components' structure and material properties and the overall mechanical environment of the plaque, and especially the fibrous cap responsible for acute cardiovascular events. However, the majority of published efforts have utilized simplified modeling approaches based on two-dimensional model plaques or assumed plane-stress states [143, 116, 23, 110, 89, 10, 194, 113, 178]. The most promising approaches [170, 112] have presented three-dimensional (3D) analyses of plaques based on fluid-structure interaction to identify flow and stress conditions and to computationally assess the fracture risk-factor of structurally different atherosclerotic lesions. In all mentioned studies, though, the arterial tissues were assumed to be isotropic, an assumption that does not reflect the experimentally observed anisotropic behavior of non-diseased [152, 84] and diseased [83, 85] vascular tissues. The aforementioned studies undoubtedly offer notable insights on the mechanics of plaque vulnerability. However, isotropic material models do not yield reliable quantitative results [87], and restrict the biomechanical interpretation of the findings

significantly. Consequently, there is a need for modeling the complex 3D arterial tissue geometry and the related mechanics in a more realistic way.

The main objective of the present study is the development of a combined imaging and computational methodology able to analyze the effect of changes in the lipid core and calcification components on the 3D mechanical environment of an artery in general and on the fibrous cap vulnerability in particular. A human carotid bifurcation with high-grade atherosclerotic plaque serves as a pilot study *ex vivo* to show the power of the presented methodology. A patient-specific geometric model is generated from high-resolution MRI, histological examination and a NURBS surface-fitting technique. The arterial wall is considered to be non-homogeneous consisting of four different tissue components. The adopted constitutive model takes into account the nonlinearity and anisotropy of the fibrous cap and the portion of the non-diseased wall incorporating the collagen fiber orientation by using a novel algorithm. The material parameters are identified from novel experimental data of human carotid bifurcations and from the literature. Different lesion compositions lead to different stress patterns within the lesions, and certain types of plaques are more prone to stress concentrations and eventual rupture than others. For example, large lipid cores are the main determinant of high-risk lesions [32, 60]. Hence, within the present study we investigated the effect of changes in lipid core and calcification on the stress distribution, especially in the fibrous cap, by keeping the cap thickness constant. In particular, we varied the volume ratio of lipid core and calcification in the generated morphological and computational model. Finally, the different models are quantified using a vulnerability index with the potential to better characterize cap vulnerability.

5.2 Biomechanical arterial model

In this section we describe the investigated specimen, the employed imaging technique, the segmentation and the generation of the 3D geometry for the arterial wall. We proceed by introducing the constitutive model and the performed mechanical tests to identify the material parameters.

5.2.1 Specimen

One carotid bifurcation was excised from a human cadaver (male, 76 yr) during autopsy, i.e. donor III in [159]. The artery had an atherosclerotic lesion of type V, according to the classification proposed in [163]. A type V lesion may consist of multiple layers of alternating composition – two or more lipid cores of unequal size, separated from each other by unequal layers of reparative fibromuscular tissue, irregularly stacked one on top of the other. After harvesting, the specimen was stored in a 37°C, calcium-free 0.9% NaCl physiological saline solution (PSS) at 4°C (approx. 4 to 8 hrs) until MR scanning. Use of autopsy material from the human subject was approved by the Ethics Committee, Medical University Graz, Austria.

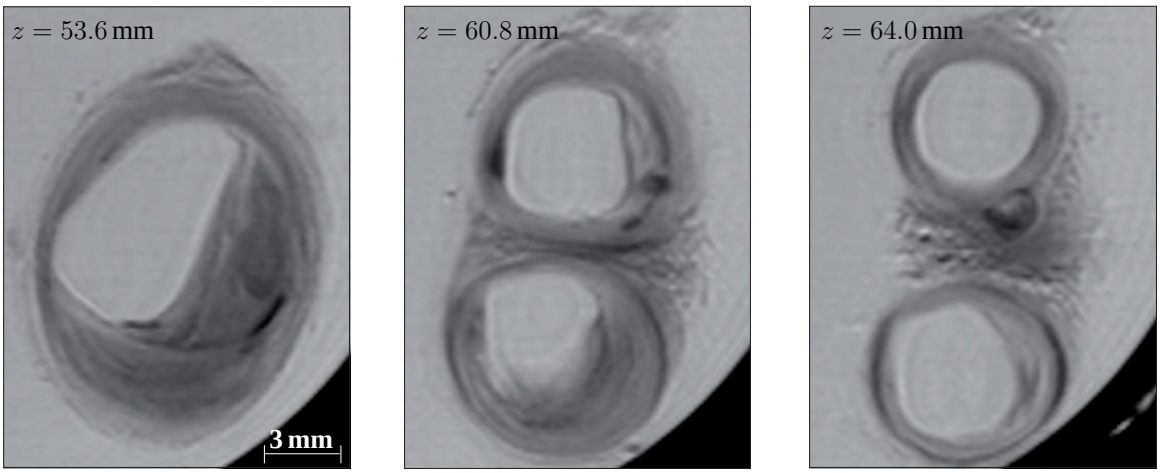

Figure 5.1: Representative T1-weighted MR images (slice thickness 0.8 mm, in plane resolution 0.15 mm) showing different sections of the excised human carotid bifurcation, with *z* referring to the coordinate system, as introduced in Figure 5.2.

5.2.2 Magnetic resonance imaging, geometric model

To identify the 3D geometry of the vessel, high-resolution MRI was used. The artery was scanned on a whole-body MR system at 1.5 T (Philips ACS-NT). Three-dimensional turbo spin echo sequences were applied to achieve high spatial resolution and a sufficient signal-to-noise ratio in an acceptable scan time of 10-15 min. We obtained 45 MRI sections with a slice thickness of 0.8 mm and an in plane resolution of 0.15 mm. Three representative T1-weighted MR images of the carotid bifurcation are shown in Figure 5.1.

Subsequently, we applied an automatic segmentation method with active contours based on a generalized gradient vector flow [8]. With this method we segmented three tissue components: (i) non-diseased wall W-nos[1], (ii) calcification I-c, (iii) lipid core I-lp [87]. The fibrous cap I-fc (fibrotic part at the luminal border) was segmented manually by a pathologist using several histological sections. Finally, based on the segmented MR images, the components' boundaries were described by means of NURB control points [138], and the volumes of the arterial tissues were reconstructed using the commercial software Rhinoceros [123]. The 3D geometric model with two characteristic cross-sections are shown in Figure 5.2.

5.2.3 Constitutive model

Arterial walls are non-homogeneous, anisotropic, highly deformable, nearly incompressible composites and exhibit a pseudoelastic response (see, e.g., [91, 82]). The choice of

[1]The abbreviation 'nos' stands for **n**ot **o**therwise **s**pecified. In the context of the present study it means 'no appreciable disease', or, more precisely 'non-atherosclerotic'.

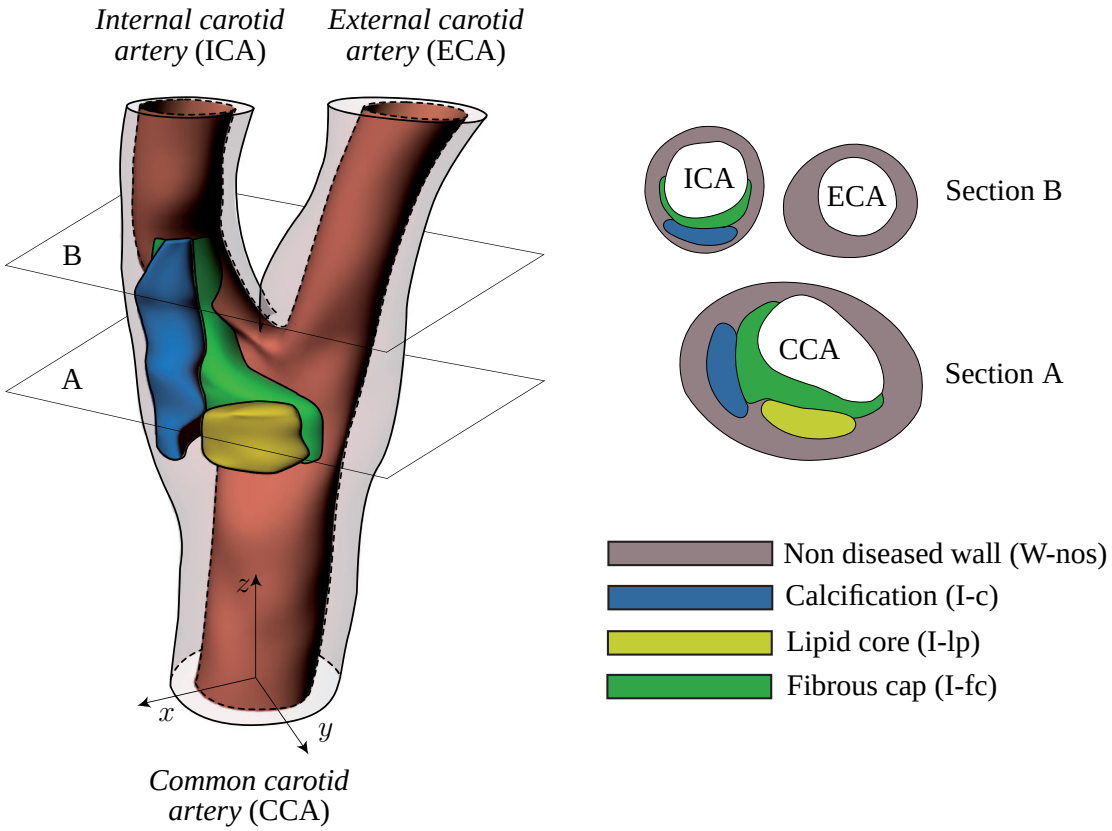

Figure 5.2: 3D geometric model of a stenotic human carotid bifurcation (atherosclerotic lesion of type V [163]) based on *in vitro* MRI (Figure 5.1) reconstructed using NURBS. Four arterial tissues are considered: non-diseased wall (W-nos), calcification (I-c), lipid core (I-lp), fibrous cap (I-fc). Two characteristic cross-sections are shown at axial planes $z = 53.6\,\text{mm}$ (Section A) and $z = 64.0\,\text{mm}$ (Section B).

the constitutive model to describe such a complex behavior is of fundamental importance for the reliable prediction of the stress environment, and the assessment of plaque rupture. We adopt the constitutive model as presented in [86, 84] and review it briefly here.

We postulate the existence of a strain-energy function Ψ and assume the decoupled form $\Psi = U(J) + \overline{\Psi}$, where $J = \det\mathbf{F} > 0$ is the volume ratio and $\mathbf{F}$ is the deformation gradient. The strictly convex function U is responsible for the volumetric elastic response of the material, while the convex function $\overline{\Psi}$ takes care of the isochoric elastic response. Since we treat the individual tissue components like incompressible materials, U takes on the role of a (purely mathematically motivated) penalty function enforcing the incompressibility constraint. We have U chosen to be

$$U(J) = \frac{\kappa}{2}(J-1)^2, \tag{5.1}$$

where κ is the bulk modulus which serves as a user-specified (positive) penalty parameter.

Clearly, with increasing κ the violation of the constraint is reduced. If the restriction on the value $\kappa \to \infty$ is taken, the constraint condition is exactly enforced, and then Ψ represents a functional for an incompressible material with $J = 1$.

The two tissue components W-nos and I-fc are considered as composites reinforced by two families of (collagen) fibers embedded in a non-collagenous groundmatrix assumed to be isotropic. An additive split of the isochoric strain-energy function $\overline{\Psi}$ into an isotropic function $\overline{\Psi}_{\mathrm{g}}$, associated with the non-collagenous groundmatrix, and two anisotropic functions $\overline{\Psi}_{\mathrm{f},i}$, $i = 1,2$, is used as in [80, 79]; thus, $\overline{\Psi}$ may be written as

$$\overline{\Psi} = \overline{\Psi}_{\mathrm{g}} + \sum_{i=1,2} \overline{\Psi}_{\mathrm{f},i}. \tag{5.2}$$

Following [88, 70], the non-collagenous groundmatrix is modeled as an isotropic neo-Hookean material, i.e.

$$\overline{\Psi}_{\mathrm{g}}(\overline{\mathbf{C}}) = \frac{\mu}{2}(\bar{I}_1 - 3), \tag{5.3}$$

where μ is a material parameter, and $\bar{I}_1 = \mathrm{tr}\overline{\mathbf{C}}$ is the first invariant of the modified Cauchy-Green tensor $\overline{\mathbf{C}} = J^{-2/3}\mathbf{F}^{\mathrm{T}}\mathbf{F}$ [76]. Following [86, 84], the second term in (5.2) has the form

$$\overline{\Psi}_{\mathrm{f},i}(\bar{I}_1, \bar{I}_{4,i}) = \frac{k_1}{2k_2}\left\{\exp\left[k_2[(1-\rho)(\bar{I}_1 - 3)^2 + \rho(\bar{I}_{4,i} - 1)^2]\right] - 1\right\}, \qquad i = 1,2, \tag{5.4}$$

where k_1, k_2 are positive material parameters, and $\bar{I}_{4,i}$ are modified invariants defined as $\bar{I}_{4,1} = \mathbf{M} \otimes \mathbf{M}$, $\bar{I}_{4,2} = \mathbf{M}' \otimes \mathbf{M}'$, where $\mathbf{M}$, $\mathbf{M}'$ denote vectors which point in the mean (reference) direction of the two families of collagen fibers. The scalar parameter $\rho \in [0,1]$ can be interpreted as a weighting factor that allows the characterization of a state between isotropic response (equally distributed collagen fibers) and anisotropic response (ideal alignment of collagen fibers). Hence, for $\rho = 1$, Equation (5.4) reduces to

$$\overline{\Psi}_{\mathrm{f},i}(\bar{I}_{4,i}) = \frac{k_1}{2k_2}\left\{\exp\left[k_2(\bar{I}_{4,i} - 1)^2\right] - 1\right\}, \qquad i = 1,2, \tag{5.5}$$

which is according to [80, 81], while for $\rho = 0$, Equation (5.4) becomes

$$\overline{\Psi}_{\mathrm{f}}(\bar{I}_1) = \frac{k_1}{2k_2}\left\{\exp\left[k_2(\bar{I}_1 - 3)^2\right] - 1\right\}, \tag{5.6}$$

which is similar to the function proposed in [36] (100% isotropic distribution). Hence, ρ can be seen as a 'switch' parameter between isotropy and anisotropy describing the 'degree of anisotropy' of the tissue.

The remaining tissue components I-c and I-lp are considered as isotropic materials described by a strain-energy function which is the sum of the functions (5.1) and (5.3).

	Material parameters				
Tissue	μ (kPa)	k_1 (kPa)	k_2 (-)	φ ($^\circ$)	ρ (-)
W-nos, I-fc	43.78	93.63	79.57	17.22	0.70
I-c	$4.50 \cdot 10^{+3}$	-	-	-	-
I-lp	0.10	-	-	-	-

Table 5.1: Material parameters for non-diseased wall (W-nos), fibrous cap (I-fc), calcification (I-c), lipid core (I-lp).

5.2.4 Mechanical tests, related material parameters

In order to determine the parameters of the functions (5.3), (5.4), we performed extension-inflation tests on the described human carotid artery at different axial stretches. The load was applied quasi-statically, while the transmural pressure, axial force, outer diameter and gage length of the arterial specimen were continuously recorded. Details on the experimental setup and the experimental procedure are provided in [152, 159].

We use here experimental data obtained from the related internal carotid artery. The material parameters for W-nos were determined by fitting (5.3), (5.4) to the data using a least squares algorithm (for details see [158]). We assumed that the collagenous components of the tissues were symmetrically disposed with respect to the vertical axis (orthotropic behavior). We neglected the radial component of the vectors $\mathbf{M}$ and $\mathbf{M}'$ thus allowing the definition of the mean directions by the single parameter φ which denotes the angle between the mean collagen fiber directions and the circumferential direction of the artery.

Material parameters for I-fc were assumed to be the same as for W-nos, while the parameters for the calcification I-c were adopted from [85]. Therein it was shown that I-c exhibits very stiff and linear mechanical responses with an average Young's modulus of 12.6 MPa. By assuming a nearly incompressible response we obtain the value $\mu = 4.50$ MPa which enters the function (5.3). The fluid-like consistency of the lipid core I-lp was modeled as a nearly incompressible, very soft neo-Hookean material. The value was taken from [87] to be $\mu = 0.1$ kPa; the same approach was pursued in [86, 99]. The material parameters for the individual tissues are summarized in Table 5.2.4. The ratios of the (penalty) parameters κ, as in (5.1), to the moduli μ for the arterial components were chosen to be roughly equivalent to two to three orders of magnitude.

5.3 Computational model

This section outlines a novel algorithm to generate the collagen fiber directions in arterial walls. It describes the finite element model including the generation of the mesh and the boundary and loading conditions. Next, four models are introduced by varying the volumes of two tissue components. These models serve as a basis for the biomechanical

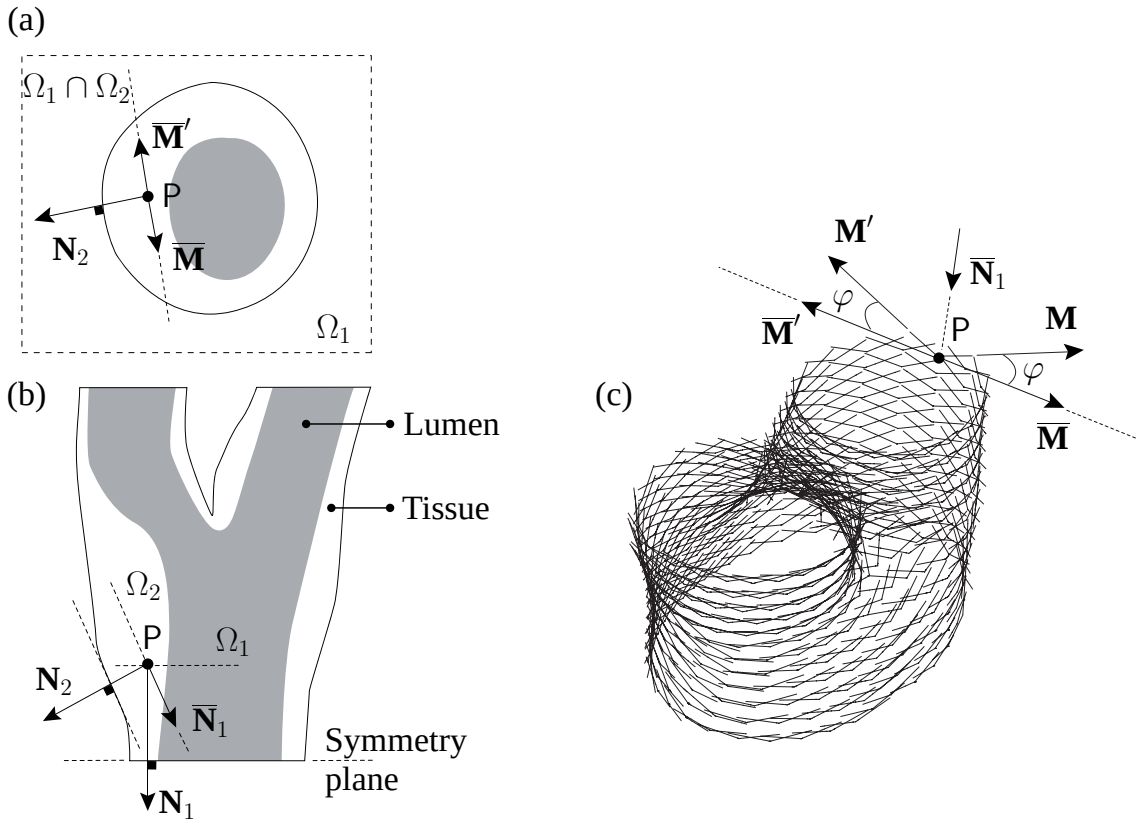

Figure 5.3: Transverse (a) and longitudinal (b) sections of the carotid bifurcation model. Every point P is projected onto its corresponding tangential planes Ω_1 and Ω_2. 3D view of the computed fiber direction vectors $\mathbf{M}$ and $\mathbf{M}'$ at the center of the superficial finite elements of the carotid bifurcation wall (c).

investigation of the relationship between tissue composition and vulnerability. Finally, a (scalar) vulnerability index is introduced to assess the rupture risk of the fibrous cap.

5.3.1 Definition of the fiber directions

The anisotropic constitutive model (5.4) requires the mean preferred directions $\mathbf{M}$, $\mathbf{M}'$ of the collagen fibers in the undeformed configuration as input data. This, however, is not a trivial task when realistic arterial geometries are considered as in the present study. The complex and irregular patient-specific models hinder a straightforward description of the local material axes. Therefore, special numerical strategies are required.

The aim is to identify the fiber directions $\mathbf{M}$, $\mathbf{M}'$ at a typical point P in the tissue. Thereby the angle φ between the collagen fibers (considered arranged in symmetrical spirals) and the circumferential direction is assumed to be known (Table 5.2.4). The algorithm used to generate the collagen fabric in space is based on tangential planes. Figures 5.3(a),(b) show

the respective transverse and longitudinal sections of the bifurcation model in addition to two planes Ω_1, Ω_2 which represent the symmetry plane of the artery and the tangential plane to the surrounding surface, respectively. The corresponding normal vectors at the projections of the point P on Ω_1 and Ω_2 are denoted by $\mathbf{N}_1$ and $\mathbf{N}_2$, respectively. The vector product $\mathbf{N}_2 \times \mathbf{N}_1$ yields the projected fiber vectors $\overline{\mathbf{M}} = -\overline{\mathbf{M}}'$ which are located on the intersection $\Omega_1 \cap \Omega_2$ of the tangential plane (Figure 5.3(a)). Finally, the fiber vectors $\mathbf{M}$, $\mathbf{M}'$ can easily be computed as

$$\mathbf{M} = \cos\varphi\overline{\mathbf{M}} - \sin\varphi\overline{\mathbf{N}}_1, \qquad \mathbf{M}' = \cos\varphi\overline{\mathbf{M}}' - \sin\varphi\overline{\mathbf{N}}_1, \tag{5.7}$$

where $\overline{\mathbf{N}}_1$ is the projection of the normal vector $\mathbf{N}_1$ on the plane Ω_2, as shown in Figure 5.3(b).

The methodology outlined above was applied to the carotid bifurcation in question. The fiber directions were computed at the center of each finite element with the angle φ, as given in Table 5.2.4. Figure 5.3(c) shows the 3D fiber structure of the carotid bifurcation wall represented by the vectors $\mathbf{M}$, $\mathbf{M}'$ for a portion close to the bifurcation. For reasons of clarity, only the direction vectors at the center of the superficial finite elements are plotted. The advantage of the described method is its simplicity in terms of conception and implementation. As it can be seen in Figure 5.3(c), the proposed strategy has the ability to provide solutions for large, arbitrarily curved, patient-specific 3D models.

5.3.2 Finite element model

The 3D geometric model of the carotid bifurcation wall, as shown in Figure 5.2, was generated using the commercially available CUBIT Geometry and Mesh Generation Toolkit [172]. The finite element mesh was generated with matching nodes on the four tissue interfaces, and no algorithmic treatment was required to link them. The mesh consists of approximately 7000 eight-node isoparametric hexahedral elements, which are based on a three-field Hu-Washizu variational formulation [76]. The used mixed $Q1/P0$-elements, as implemented in the multi-purpose finite element analysis program FEAP [171], provide an efficient and proper description of the isochoric deformation of the tissue components.

Experimental investigations (see, e.g., [151, 57, 84]) show that human vessels exhibit an axial *in situ* pre-stretch. Consequently, a displacement-controlled axial stretch of $\lambda_z = 1.05$ was initially applied to all nodes located at the upper face of the arterial wall. Subsequently, all nodes of the upper and lower faces of the bifurcation were fixed in all three directions. Next, a blood pressure of 140 mmHg was applied which was performed by follower (deformation-dependent) pressure loads applied to each facet of the luminal surface.

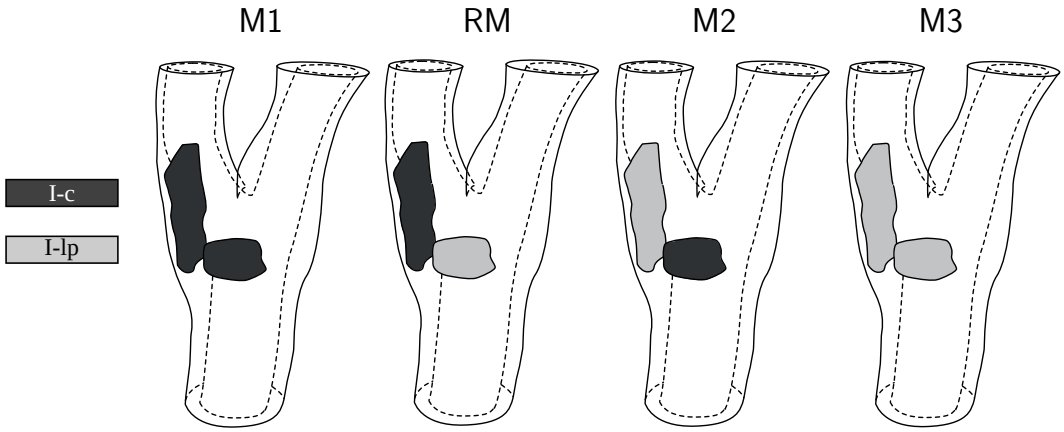

Model	Description	Tissue volume in % $V_{\mathrm{I-lp}}$	$V_{\mathrm{I-c}}$
M1	I-lp modeled as I-c	0	100
RM	Reference model (Figure 5.2)	25	75
M2	Interchange of I-lp with I-c	75	25
M3	I-c modeled as I-lp	100	0

Table 5.2: Four models characterized by variations of the volume $V_{\mathrm{I-lp}}$ (in %) of the lipid core and the volume $V_{\mathrm{I-c}}$ of the calcification. Model RM refers to the **R**eference **M**odel according to Figure 5.2.

5.3.3 Model variation

The quantitative effect of the severity of lipid core I-lp and calcification I-c on the mechanical stress environment and eventually on the stability of the considered carotid bifurcation is studied. Detailed analyses are performed in which the volumes $V_{\mathrm{I-lp}}$ and $V_{\mathrm{I-c}}$ (in percentage) of the respective tissue components serve as parameters. We generate and analyze variations on the acquired reference model (shown in Figure 5.2) by keeping the cap thickness. In this model, which we subsequently call 'RM' (**R**eference **M**odel), the I-lp volume is comprised of 25% while the I-c volume has 75%. A first variation of RM is model M1 in which I-lp is not present ($V_{\mathrm{I-c}} = 100\%$). Model M2 has the ratio $V_{\mathrm{I-lp}} = 75\%$, $V_{\mathrm{I-c}} = 25\%$ of the two involved tissues, while in model M3 I-c is not present ($V_{\mathrm{I-lp}} = 100\%$). Hence, the volumes of I-lp in the models M1, RM, M2, M3 vary from 0% to 100%. Table 5.3.2 summarizes the four investigated models.

5.3.4 Index of cap vulnerability

Here we introduce scalar quantities to serve as vulnerability criteria. The idea to use such indicators goes back to the studies [86, 169, 99] which aim to identify plaque risk and

assess stent design. We propose a novel vulnerability index, subsequently denoted as ξ, to quantify the loaded fibrous cap I-fc. Thus,

$$\xi = w_1 D_1 + w_2 D_2, \tag{5.8}$$

where ξ is a function of the user-defined parameters $w_1, w_2 \in [0,1]$, which are weighting factors with the condition $w_1 + w_2 = 1$, while D_1 and D_2 are stress-dependent scalars subsequently explained.

The scalar D_1 is defined as

$$D_1 = \frac{\max(\sigma^{\mathrm{I-fc}})}{\sigma_{\mathrm{allow}}}, \qquad \sigma_{\mathrm{allow}} = \frac{\sigma_{\mathrm{ult}}^{\mathrm{I-fc}}}{f_{\mathrm{s}}}, \tag{5.9}$$

where $\max(\sigma^{\mathrm{I-fc}})$ denotes the maximum principal Cauchy stress in I-fc, and σ_{allow} denotes an allowable stress that must not exceeded anywhere in the structure of I-fc. In addition, we have introduced the notation f_{s} for the factor of safety with respect to the ultimate stress $\sigma_{\mathrm{ult}}^{\mathrm{I-fc}}$ of I-fc in the circumferential direction. From (5.9) it is clear that for the case $D_1 > 1$ the stress exceeds the allowable stress σ_{allow} at least at one point in I-fc. The scalar D_1 characterizes the *local* stress environment in I-fc, and is, therefore, related to the localized vulnerability status of the tissue.

The scalar D_2 in (5.8) is defined as

$$D_2 = \frac{\sum_{i=1}^{n_{\mathrm{e}}^{\mathrm{I-fc}}} \sigma_i^{\mathrm{I-fc}} \Omega_i^*}{\sum_{i=1}^{n_{\mathrm{e}}^{\mathrm{I-fc}}} \sigma_{\mathrm{allow}} \Omega_i^*} \qquad \text{with} \qquad \Omega_i^* = \begin{cases} \Omega_i & \text{if } \sigma_i^{\mathrm{I-fc}} > \sigma_{\mathrm{allow}}, \\ 0 & \text{otherwise}, \end{cases} \tag{5.10}$$

where $n_{\mathrm{e}}^{\mathrm{I-fc}}$ is the total number of finite elements within the volume of I-fc, and $\sigma_i^{\mathrm{I-fc}}$ denotes the maximum principal Cauchy stress in the finite element i of I-fc. Both stress quantities $\sigma_i^{\mathrm{I-fc}}$ and σ_{allow} are weighted by the volume Ω_i of the finite element i in order to make D_2 mesh independent. The scalar D_2 considers only those finite elements in which the maximum principal stress $\sigma_i^{\mathrm{I-fc}}$ is higher than the allowable stress σ_{allow}. It characterizes the *global* stress environment within I-fc, and is, therefore, related to the overall vulnerability status of the tissue. From the definitions (5.8)–(5.10) one may conclude that lower values of D_1, D_2 (and consequently ξ) are related to more stable caps, while higher values indicate a higher risk of cap rupture.

5.4 Results

Here we present the most illustrative results of the numerical analysis, in particular, we focus on the 3D stress fields of the arterial tissues for the models RM and M2. Next, the

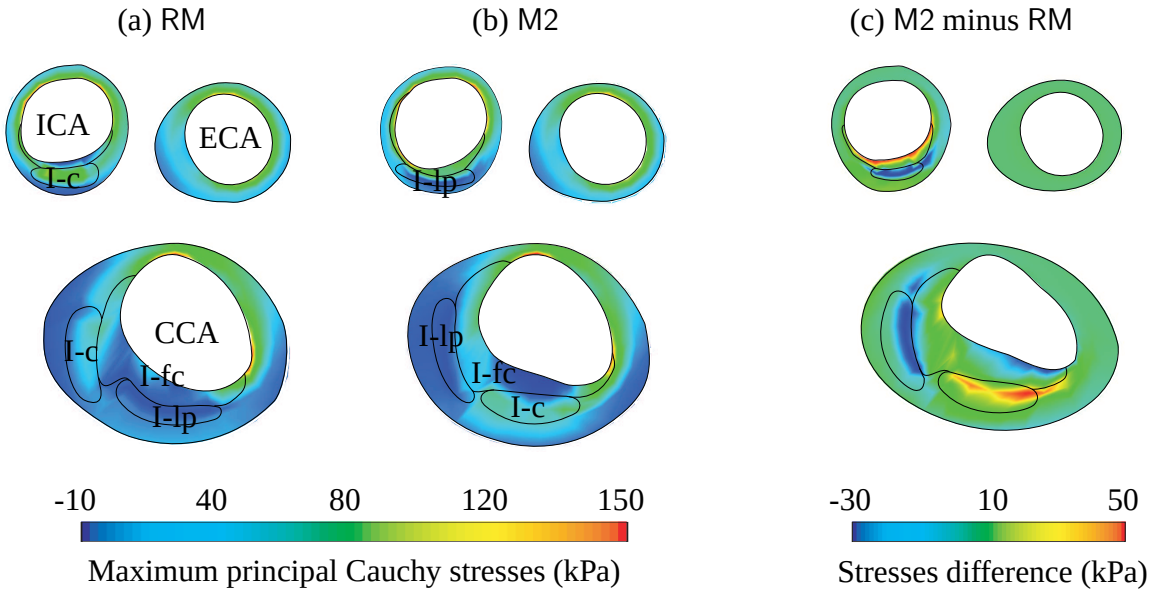

Figure 5.4: Maximum principal Cauchy stress at the deformed configuration of the cross-sections A, at $z = 53.6\,\text{mm}$, and B, at $z = 64.0\,\text{mm}$ (for the geometrical situation see Figure 5.2) for (a) model RM ($V_{\text{I-lp}} = 25\%$, $V_{\text{I-c}} = 75\%$) and (b) model M2 ($V_{\text{I-lp}} = 75\%$, $V_{\text{I-c}} = 25\%$). Stress difference between models M2 and RM at the unloaded configuration of the considered cross-sections (c). For the sake of clearness, the boundaries of fibrous cap, lipid core, and calcification are shown.

stress difference between the two models and the changes in the maximum principal stress for the four models in I-fc are presented. Finally, the changes of the vulnerability index due to morphological variations are documented.

5.4.1 Predicted stress field

Figure 5.4(a) depicts the distribution of the maximum principal Cauchy stress at the deformed configuration of the characteristic cross-sections A and B (Figure 5.2) for model RM. Since the circumferential arterial direction is the main loading direction it can be concluded that one principal axis is close to the circumferential direction. A study of Figure 5.4(a) reveals that the highest stress regions are located at the thinnest part of W-nos, and most importantly, in the vicinity of the shoulders of I-fc. These results correlate well with the intimal tear sites found at necropsy (see, e.g., [17, 31]) and point out that I-lp is under a relatively low compressive hydrostatic pressure, while in the stiff calcified tissue I-c higher stresses are identified. The presented findings are in agreement with other computational studies [170, 194, 113].

In Figure 5.4(b) the results for model M2 are illustrated. In this model for which I-lp and I-c are interchanged (Table 5.3.2), the strain and stress distributions are significantly different.

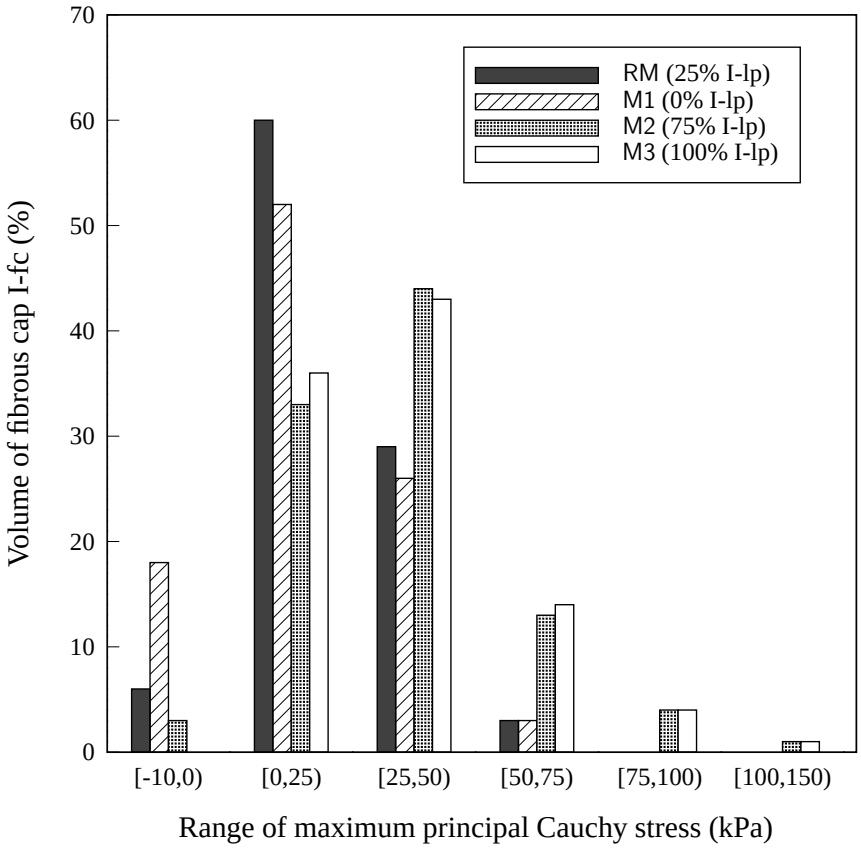

Figure 5.5: Maximum principal Cauchy stress in the fibrous cap I-fc for the four models (Table 5.3.2). The ranges of stress are plotted with respect to the volume of I-fc. As the tissue composition becomes richer in lipid higher stresses are identified in the fibrous cap.

Even though I-c and W-nos bear the main load of the structure, larger areas of maximal stresses are identified in the fibrous cap. This can also be clearly seen in Figure 5.4(c), where the stress difference between the models M2 and RM is plotted with respect to the unloaded configuration of the lesion. It should be noted, that for the internal carotid artery the stresses inside I-fc for model M2 increase by almost 50 kPa when compared to model RM, characterizing thus a more rupture-prone stenosis.

Figure 5.5 illustrates the changes in the maximum principal Cauchy stress for the four models in the fibrous cap, which is the most detrimental tissue to plaque stability. In particular, the ranges of stress are plotted with respect to the volume of I-fc. From the figure it is evident that the models M2 and M3 (75% and 100% I-lp, respectively) lead to higher stresses. A positive correlation between the increase of I-lp portion and the mechanical stress in I-fc is evident.

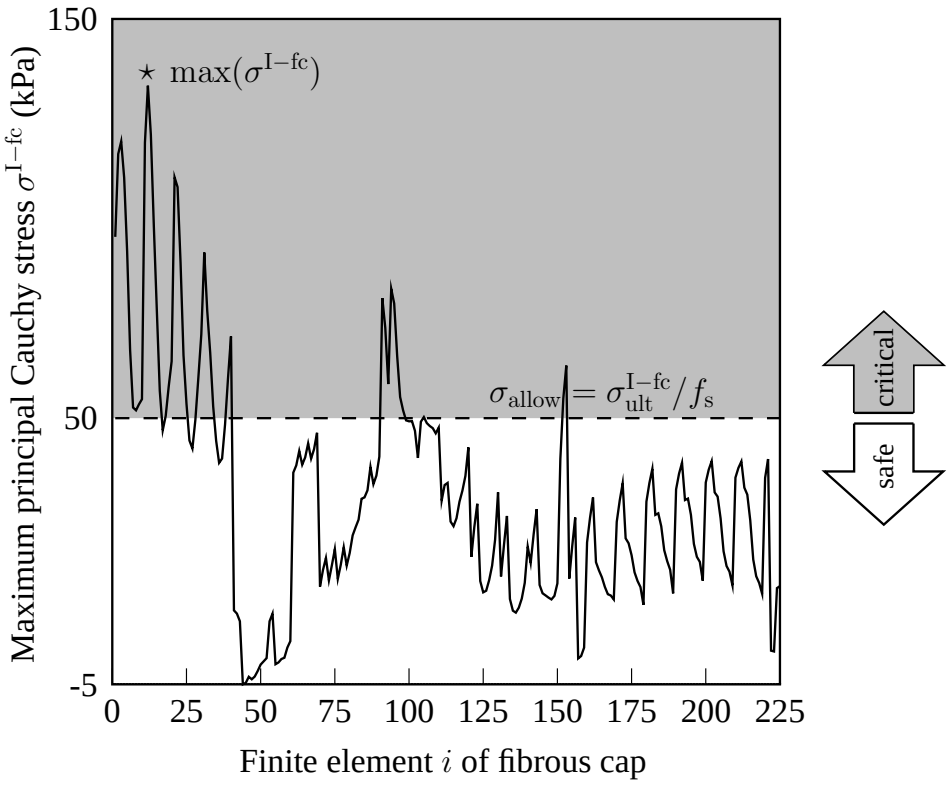

Figure 5.6: Maximum principal Cauchy stress $\sigma^{\mathrm{I-fc}}$ in the finite elements of the fibrous cap I-fc for model M2 (75% I-lp). At several locations the stresses in I-fc exceed the allowable stress $\sigma_{\mathrm{allow}} = 50\,\mathrm{kPa}$. For scalar D_1, i.e. Equation (5.9), the maximum stress $\max(\sigma^{\mathrm{I-fc}})$ at $i = 12$ (symbol $\star$) is relevant, while for scalar D_2, i.e. Equation (5.10), every finite element in which the stress is above σ_{allow} is considered.

5.4.2 Predicted fibrous cap vulnerability

According to an experimental study on nine human high-grade stenotic arteries [85], the fibrous cap along the circumferential direction exhibits the lowest fracture stress of all intimal tissues investigated, with a value of $\sigma^{\mathrm{I-fc}}_{\mathrm{ult}} = 254.8 \pm 79.8\,\mathrm{kPa}$. Hence, for the present study we used 250 kPa and a value of 5 for the safety factor f_{s}, which gives an allowable stress σ_{allow} of 50 kPa.

Figure 5.6 depicts the distribution of the maximum principal Cauchy stress $\sigma^{\mathrm{I-fc}}$ in the finite elements of I-fc for model M2 (75% I-lp). As can be seen, the maximum principal stress is higher than the allowable stress σ_{allow} for several finite elements (compare also with Figure 5.5). The stress level at those elements is, therefore, considered to be critical, while the stress level at the other elements is considered to be safe. For the computation of the scalar D_1, the maximum stress $\max(\sigma^{\mathrm{I-fc}})$ at $i = 12$, indicated by the symbol $\star$, is relevant, while every finite element in which the stress is above σ_{allow} contributes to the component D_2.

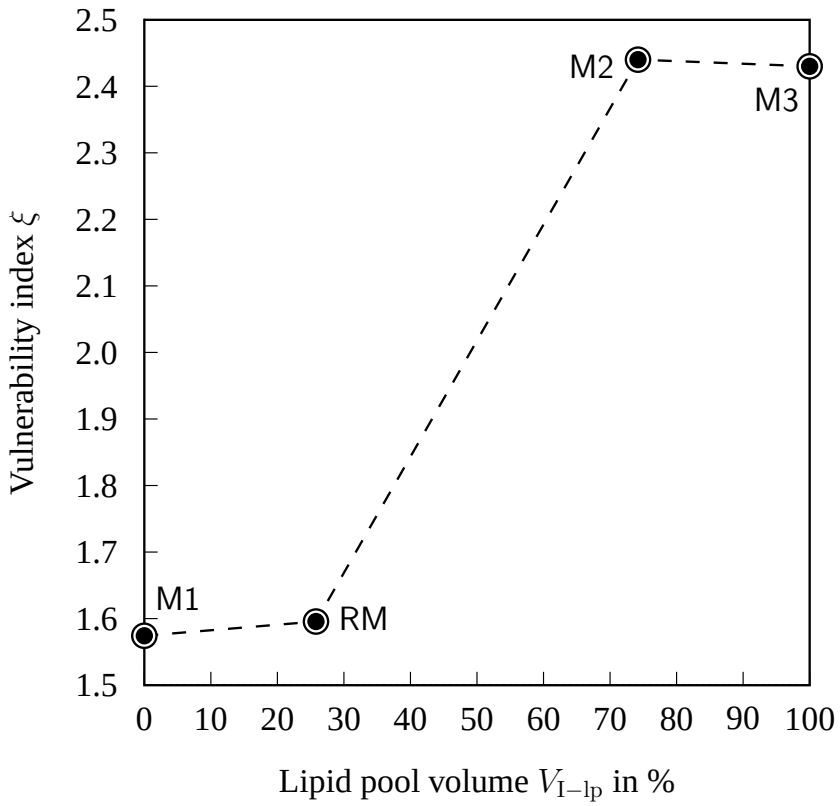

Figure 5.7: Vulnerability index ξ, i.e. Equation (5.8), for the four models (Table 5.3.2) with $w_1 = w_2 = 0.5$. Model M1 has no lipid core while $V_{\mathrm{I-lp}} = 100\%$ in model M3. For models M2, M3 the vulnerability index is more than 50% higher in comparison to reference model RM.

In order to compare the rupture risk of the four lesion morphologies (RM, M1, M2, M3), the vulnerability index ξ, as defined in (5.8), is computed by assuming equal weighting factors ($w_1 = w_2 = 0.5$). The results are illustrated in Figure 5.7 from which it is evident that $\xi > 1$ for all models. With the selected safety factor, the morphologies of all four cases are considered to be vulnerable. The smallest vulnerability index ($\xi = 1.57$) is obtained for model M1 for which no I-lp is present. For the reference model RM a slightly higher value ξ is computed. However, when the lesion consists of a higher amount of lipid, then the vulnerability index ξ increases considerably (by more than 50%). The lesion composed only by I-lp, i.e. model M3, leads to comparable results to model M2. A heavily loaded fibrous cap is thus detected, and, consequently, a higher risk for cap rupture is identified.

5.5 Discussion and conclusion

Vulnerable plaque morphology is usually described by gross pathology and intravascular ultrasound. However, morphological criteria alone cannot reliably explain vulnerability

which involves factors such as inflammatory processes, geometry, composition and wall stresses that occur due to certain loading and boundary conditions, just to mention a few [54]. The last three aspects require biomechanical studies.

Based on the above arguments, we developed a multi-disciplinary methodology for the quantification of the tissue-specific micro-mechanical environment of atherosclerotic plaques by combining MR imaging with established mechanical analysis tools. In order to show the methodology, a carotid bifurcation with a high-grade stenosis excised from a human cadaver served as a basis (for MR images see Figure 5.1). We generated a highly-resolved 3D geometric model (Figure 5.2) using segmentation methods for which both MR and histological images were considered. We segmented four tissues, i.e. non-diseased wall W-nos, fibrous cap I-fc, lipid core I-lp, calcification I-c, and described the nonlinear elastic response of each tissue by a strain-energy function. The material parameters were determined from related extension-inflation tests [159, 158] and from the literature (Table 5.2.4). Note that we have not identified the structural arrangement of collagen, and hence the angle φ was used as a phenomenological parameter. Nevertheless, a structural analysis of collagen using methods such as polarized light microscopy should be used to obtain related structural parameters; for a recent survey comparing different methods see [78].

A novel numerical algorithm based on tangential planes was employed to allow the otherwise laborious computation of the local material axes in the case of large 3D, arbitrarily curved, patient-specific geometric models (Figure 5.3). The related algorithm was first described in [96] focussing on finite element studies of inhomogeneities within the intervertebral disc. To the authors' knowledge, this method has not yet been applied to patient-specific models of arterial tissues. The algorithm provided a robust and fast generation of the 3D collagen fabric; non-uniqueness of the generated fiber directions was not detected even for such a complex geometrical setting of a multi-layered bifurcation. In [62], the problem of identifying local material axes is solved by mapping the undeformed configuration Ω_o of the artery to an eccentric thick-walled tube with configuration $\overline{\Omega}_o$, in which the (local) radial, circumferential and axial directions can be defined in a straightforward way. A pull-back operation with the rotation tensor provides then the material axes in the initial configuration. Even though this technique seems to address the problem sufficiently, it is demanding and the definition of the configuration $\overline{\Omega}_o$ has an influence on the prediction of the material axes.

In addition to the generated patient-specific geometric model, three variations of the bifurcation's composition were introduced (Table 5.3.2). Thereby, we focussed on the variation of the I-lp and I-c volumes by keeping the cap thickness constant. The numerical analysis was performed by considering a blood pressure of 140 mmHg, which is an elevated pressure load. According to [24] systolic blood pressure of more than 140 mmHg is a much more important cardiovascular disease risk factor than diastolic blood pressure in persons older than 50 years. In addition, data from observational and trial studies suggest that high blood pressure is a main contributor to the profile of atherothrombotic patients [56, 14, 132].

The computational analysis of the four models revealed that changes of the volume portion of I-lp lead to significantly different stress distributions in the stenosis. In particular, we identified a correlation between a lipid-rich stenosis and a severely mechanically loaded I-fc prone to rupture (Figures 5.4, 5.5). Finally, we proposed scalar quantities that are related to the local and global stress environment in I-fc serving as cap vulnerability criteria (Figures 5.6, 5.7). The introduced vulnerability index ξ considers a safety factor f_s which is defined with respect to the ultimate stress of I-fc. Note that there are several ways in which factors of safety can be defined. Higher values of ξ suggest a higher risk of cap rupture. The index ξ provides a more efficient and objective rupture-risk assessment of atherosclerotic plaques. Such a vulnerability index has the potential to bridge the gap between the medical and engineering community and may serve as a more quantitative tool for diagnosis, treatment and prevention.

Despite some novelties and increased complexities of the used geometric and material models there is room for improvements. The multi-layered structure of W-nos was modeled as one homogeneous material, and the material properties of I-fc was assumed to behave similar to the homogenized wall material. Tissue-specific mechanical properties of sclerotic human carotid arteries would improve modeling. In addition, due to the lack of experimental data and computational complexities, residual stresses were not considered in the healthy portion of the bifurcation. Based on the authors' experience there are no (or at least very minor) residual stresses present in the diseased portion of the bifurcation such as the fibrous cap. Consequently, a diseased arterial ring does not spring open when cut in a radial direction within the diseased potion. We did not consider pulsatile blood pressure and fluid-structure interaction models such as presented in [119, 170], which may strengthen the computational findings of our approach. The present analysis is limited to the *in vitro* assessment of rupture-prone plaques. During the last years the ability of *in vivo* carotid MR imaging has been significantly improved (see, e.g., [175, 157, 71, 147]). 3-Tesla MR scanners are finding their way to the clinical arena, and the development of computerized plaque characterization methods to deal with a large amount of high-resolution multi-contrast data is ongoing. The extension of the proposed methodology to *in vivo* implementation is, therefore, feasible.

In the present study a model of a human carotid bifurcation served as a (test) basis for the developed computational platform. The methodology can also be applied to other arteries such as coronary arteries to evaluate the rupture risk. One may argue that the results of the presented method-oriented study were highly individual and not representative for atherosclerotic lesions in general. However, the prospect of the documented attempt is the individual diagnosis and assessment of rupture-prone plaques. Moreover, the above discussion suggests that even the study of a single lesion model can stimulate novel ideas and provide intriguing insights, which are of general significance for the issue of plaque stability. One should further take into consideration that patient-specific computational analyses have considerable advantages over conventional large clinical trials. For example, they are less expensive and time-consuming, they are harmless to patients and allow control and systematic variations of all essential parameters.

The combination of MR image data, computerized plaque segmentation and nonlinear finite element analysis, as performed in the present study, constitutes a powerful platform able to investigate quantitatively the biomechanical behavior of atherosclerotic plaques in patient-specific stenoses. This cannot be performed by entirely morphological approaches. In light of the presented results, the authors feel that the proposed methodology may be of interest to several branches of clinical medicine dealing with vessel diagnosis and therapy including radiology, cardiology and cardiovascular medicine. The outcome of the current study may serve *in vivo* patient studies in future.

REFERENCES

[1] H. Abè, K. Hayashi, and M. Sato, editors. *Data Book on Mechanical Properties of Living Cells, Tissues, and Organs*. Springer-Verlag, New York, 1996.

[2] M. Al-Dojayli and S. A. Meguid. Accurate modeling of contact using cubic splines. *Finite Elem. Anal. Des.*, 38:337–352, 2002.

[3] St. Allender, P. Scarborough, V. Peto, M. Rayner, J. Leal, R. Luengo-Fernandez, and A. Gray. *European Cardiovascular Disease Statistics, 2008 Edition*. Department of Public Health, University of Oxford, 2008. `http://www.heartstats.org/uploads/documents%5Cproof30NOV2007.pdf`.

[4] American Society for Metals International Handbook Committee. *Metals Handbook*. ASM International, Ohio, 1999.

[5] L. H. Arroyo and R. T. Lee. Mechanisms of plaque rupture: mechanical and biologic interactions. *Cardiovasc. Res.*, 41:369–375, 1999.

[6] G. A. Ateshian. A B–spline least–squares surface–fitting method for articular surfaces of diarthrodial joints. *J. Biomech. Eng.*, 115:366–373, 1993.

[7] M. Auer, R. Stollberger, P. Regitnig, F. Ebner, and G. A. Holzapfel. A methodology to study the morphologic changes in lesions during *in vitro* angioplasty using MRI and image processing. *Med. Image Anal.* in press.

[8] M. Auer, R. Stollberger, P. Regitnig, F. Ebner, and G. A. Holzapfel. 3-D reconstruction of tissue components for atherosclerotic human arteries based on high–resolution MRI. *IEEE T. Med. Imaging*, 25:345–357, 2006.

[9] F. Auricchio, M. Di Loreto, and E. Sacco. Finite–element analysis of a stenotic revascularization through a stent insertion. *Comput. Meth. Biomech. Biomed. Eng.*, 4:249–264, 2001.

[10] R. A. Baldewsing, C. L. de Korte, J. A. Schaar, F. Mastik, and A. F. van der Steen. Finite element modeling and intravascular ultrasound elastography of vulnerable plaques: parameter variation. *Ultrasonics*, 42:723–729, 2004.

[11] A. J. Bank, A. Versluis, S. M. Dodge, and W. H. Douglas. Ahterosclerotic plaque rupture: a fatigue process? *Med. Hypotheses*, 55:480–484, 2000.

[12] P. Barragan, R. Rieu, V. Garitey, P. O. Roquebert, J. Sainsous, M. Silvestri, and G. Bayet. Elastic recoil of coronary stents: a comparative analysis. *Catheter Cardiovasc. Interv.*, 50:112–119, 2000.

[13] J. Bedoya, C. A. Meyer, L. H. Timmins, M. R. Moreno, and J. E. Moore Jr. Effects of stent design parameters on normal artery wall mechanics. *J. Biomech. Eng.*, 128:757–765, 2006.

[14] D. L. Bhatt, P. G. Steg, E. M. Ohman, A. T. Hirsch, Y. Ikeda, J. L. Mas, S. Goto, C. S. Liau, A. J. Richard, J. Röther, P. W. Wilson, and REACH Registry Investigators. International prevalence, recognition, and treatment of cardiovascular risk factors in outpatients with atherothrombosis. *J. Am. Med. Assoc.*, 295:180–189, 2006.

[15] W. Böhm, G. Farin, and J. Kahmann. A survey of curve and surface methods in CAGD. *Comput. Aided Geom. Design*, 1:1–60, 1984.

[16] H. Brauer, J. Stolpmann, H. Hallmann, R. Erbel, and A. Fischer. Measurement and numerical simulation of the dilatation behaviour of coronary stents. *Mat.-wiss. u. Werkstofftechn.*, 30:876–885, 1999.

[17] A. P. Burke, A. Farb, G. T. Malcom, Y. H. Liang, J. Smialek, and R. Virmani. Coronary risk factors and plaque morphology in men with coronary disease who died suddenly. *N. Engl. J. Med.*, 18:1276–1284, 1997.

[18] H. M. Burton and W. L. Hunter. Drug-eluting stents: A multidisciplinary success story. *Adv. Drug Deliv. Rev.*, 58:350–357, 2006.

[19] J. P. Carrozza, R. E. Kuntz, M. J. Levine, R. M. Pomerantz, R. F. Fishman, M. Mansour, C. M. Gibson, C. C. Senerchia, D. J. Diver, and R. D. Safian et al. Angiographic and clinical outcome of intracoronary stenting: immediate and long-term results from a large single-center experience. *J. Am. Coll. Cardiol.*, 20:328–337, 1992.

[20] W. Casscells, M. Naghavi, and J. T. Willerson. Vulnerable atherosclerotic plaque: a multifocal disease. *Circulation*, 107:2072–2075, 2003.

[21] W. R. Castaneda-Zuniga, A. Formanek, M. Tadavarthy, Z. Vlodaver, J. E. Edwards, C. Zollikofer, and K. Amplatz. The mechanism of balloon angioplasty. *Radiology*, 135:565–571, 1980.

[22] E. Catmull and J. Clark. Recursively generated B-spline surfaces on arbitrary topological meshes. *Comput. Aided Design*, 10:350–355, 1978.

[23] G. C. Cheng, H. M. Loree, R. D. Kamm, M. C. Fishbein, and R. T. Lee. Distribution of circumferential stress in ruptured and stable atherosclerotic lesions: A structural analysis with histopathological correlation. *Circulation*, 87:1179–1187, 1993.

[24] A. V. Chobanian, G. L. Bakris, H. R. Black, W. C. Cushman, L. A. Green, J. L. Izzo, D. W. Jones, B. J. Materson, S. Oparil, J. T. Wright, and E. J. Roccella. The seventh report of the joint national committee on prevention, detection, evaluation and treatment of high blood pressure. *J. Am. Med. Assoc.*, 289:2560–2572, 2003.

[25] S. N. David Chua, B. J. Mac Donald, and M. S. J. Hashmi. Finite element simulation of stent and balloon interaction. *J. Mat. Proc. Techn.*, 143–144:591–597, 2003.

[26] F. Cirak and M. Ortiz. Fully C^1-conforming subdivision elements for finite deformation thin-shell analysis. *Int. J. Numer. Meth. Eng.*, 51:813–833, 2001.

[27] R. H. Cox. Passive mechanics and connective tissue composition of canine arteries. *Am. J. Physiol.*, 234:H533–H541, 1978.

[28] R. H. Cox and D. K. Detweiler. Arterial wall properties and dietary atherosclerosis in the racing greyhound. *Am. J. Physiol.*, 236:H790–H797, 1979.

[29] T. Dalrymple. An analytical overlay technique for describing deformable contact surfaces. In *CD–ROM Proceedings of the European Congress on Computational Methods in Applied Sciences and Engineering, ECCM 1999*, W. Wunderlich (Ed), München, 1999. Institut für Statik.

[30] M. J. Davies. *Atlas of Coronary Artery Disease*. Lippincott-Raven, Philadelphia, 1998.

[31] M. J. Davies. The pathophysiology of acute coronary syndromes. *Heart*, 83:361–366, 2000.

[32] M. J. Davies. Going from immutable to mutable atherosclerotic plaques. *Am. J. Cardiol.*, 88 (Supl):2F–9F, 2001.

[33] M. J. Davies, P. D. Richardson, N. Woolf, D. R. Katz, and J. Mann. Risk of thrombosis in human atherosclerotic plaques: role of extracellular lipid, macrophage, and smooth muscle cell content. *Br. Heart J.*, 69:377–381, 1993.

[34] M. Degertekin, E. Regar, K. Tanabe, P. C. Smits, W. J. van der Giessen, S. G. Carlier, P. de Feyter, J. Vos, D. P. Foley, J. M. Ligthart, J. J. Popma, and P. W. Serruys. Sirolimus-eluting stent for treatment of complex in-stent restenosis: the first clinical experience. *J. Am. Coll. Cardiol.*, 41:184–189, 2003.

[35] A. Delfino, N. Stergiopulos, J. E. Moore Jr., and J.-J. Meister. Residual strain effects on the stress field in a thick wall finite element model of the human carotid bifurcation. *J. Biomech.*, 30:777–786, 1997.

[36] H. Demiray. A note on the elasticity of soft biological tissues. *J. Biomech.*, 5:309–311, 1972.

[37] Y. Y. Dhaher, S. L. Delp, and W. Z. Rymer. The use of basis function in modelling joint articular surfaces: application to the knee joint. *J. Biomech.*, 33:901–907, 2000.

[38] M. De Beule, R. Van Impe, B. Verhegghe, P. Segers, and P. Verdonck. Finite element analysis and stent design: Reduction of dogboning. *Technol. Health Care*, 14:233–241, 2006.

[39] M. De Beule, P. Mortier, R. Van Impe, B. Verhegghe, P. Segers, and P. Verdonck. Plasticity in the mechanical behaviour of cardiovascular stents during stent preparation (crimping) and placement (expansion). *Key Eng. Mater.*, 340–341:847–852, 2007.

[40] E. W. Donnelly, M. S. Bruzzi, T. Connolley, and P. E. McHugh. Finite element comparison of performance related characteristics of balloon expandable stents. *Comput. Meth. Biomech. Biomed. Eng.*, 10:103–110, 2007.

[41] S. H. Duda, J. Wiskirchen, G. Tepe, M. Bitzer, T. W. Kaulich, D. Stoeckel, and C. D. Claussen. Physical properties of endovascular stents: An experimental comparison. *J. Vasc. Interv. Radiol.*, 11:645–654, 2000.

[42] C. Dumoulin and B. Cochelin. Mechanical behaviour modelling of balloon-expandable stents. *J. Biomech.*, 33:1461–1470, 2000.

[43] E. R. Edelman and C. R. Rogers. Pathobiologic responses to stenting. *Am. J. Cardiol.*, 81:4E–6E, 1998.

[44] N. El-Abbasi, S. A. Meguid, and A. Czekanski. On the modelling of smooth contact surfaces using cubic splines. *Int. J. Numer. Meth. Eng.*, 50:953–967, 2001.

[45] F. Etave, G. Finet, M. Boivin, J. C. Boyer, G. Rioufol, and G. Thollet. Mechanical properties of coronary stents determined by using finite element analysis. *J. Biomech.*, 34:1065–75, 2001.

[46] E. Falk. Morphologic features of unstable atherothrombotic plaques underlying acute coronary syndromes. *Am. J. Cardiol.*, 63:114E–120E, 1989.

[47] E. Falk. Why do plaques rupture? *Circulation*, 86:30–42, 1992.

[48] A. Farb, G. Sangiorgi, A. J. Carter, V. M. Walley, W. D. Edwards, R. S. Schwartz, and R. Virmani. Pathology of acute and chronic coronary stenting in humans. *Circulation*, 99:44–52, 1999.

[49] G. Farin. *Curves and Surfaces for Computer-Aided Geometric Design*. Academic Press, San Diego, 1990.

[50] R. Fattori and T. Piva. Drug-eluting stents in vascular intervention. *Lancet*, 361:247–249, 2003.

[51] Z. A. Fayad and V. Fuster. Clinical imaging of the high-risk or vulnerable atherosclerotic plaque. *Circ. Res.*, 89:305–316, 2001.

[52] Z. A. Fayad, V. Fuster, J. T. Fallon, T. Jayasundera, S. G. Worthley, G. Helft, J. G. Aguinaldo, J. J. Badimon, and S. K. Sharma. Noninvasive *in vivo* human coronary artery lumen and wall imaging using black-blood magnetic resonance imaging. *Circulation*, 102:506–510, 2000.

[53] Z. A. Fayad, V. Fuster, K. Nikolaou, and C. Becker. Computed tomography and magnetic resonance imaging for noninvasive coronary angiography and plaque imaging: Current and potential future concepts. *Circulation*, 106:2026–2034, 2002.

[54] G. Finet, J. Ohayon, G. Rioufol, S. Lefloch, P. Tracqui, O. Dubreuil, and A. Tabib. Morphological and biomechanical aspects of vulnerable coronary plaque. 100:547–553, 2007.

[55] T. J. Fogarty, A. Chin, P. M. Shoor, G. L. Blair, and J. J. Zimmerman. Adjunctive intraoperative arterial dilation. *Arch. Surg.*, 116:1391–1398, 1981.

[56] S. S. Franklin, M. G. Larson, S. A. Khan, N. D. Wong, E. P. Leip, W. B. Kannel, and D. Levy. Does the relation of blood pressure to coronary heart disease risk change with aging?: the framingham hear study. *Circulation*, 103:1245–1249, 2001.

[57] P. Fridez, M. Zulliger, F. Bobard, G. Montorzi, H. Miyazaki, K. Hayashi, and N. Stergiopulos. Geometrical, functional, and histomorphometric adaptation of rat carotid artery in induced hypertension. *J. Biomech.*, 36:671–680, 2003.

[58] V. Fuster, L. Badimon, J. J. Badimon, and J. H. Chesebro. The pathogenesis of coronary artery disease and the acute coronary syndromes. *N. Engl. J. Med.*, 326:310–316, 1992.

[59] V. Fuster, J. T. Fallon, and Y. Nemerson. Coronary thrombosis. *Lancet*, 348:Suppl 1:s7–10, 1996.

[60] V. Fuster, P. R. Moreno, Z. A. Fayad, R. Corti, and J. J. Badimon. Atherothrombosis and high–risk plaque: Part I: evolving concepts. *J. Am. Coll. Cardiol.*, 46:937–954, 2005.

[61] T. C. Gasser and G. A. Holzapfel. Physical and numerical modeling of dissection propagation in arteries caused by balloon angioplasty. In M. H. Hamza (ed.), editor, *Proceedings of the 3rd IASTED International Conference on Biomechanics*, pages 229–233, Anaheim, 2005. ACTA Press.

[62] T. C. Gasser and G. A. Holzapfel. Modeling plaque fissuring and dissection during balloon angioplasty intervention. *Ann. Biomed. Eng.*, 35:711–723, 2007.

[63] T. C. Gasser, R. W. Ogden, and G. A. Holzapfel. Hyperelastic modelling of arterial layers with distributed collagen fibre orientations. *J. R. Soc. Interface*, 3:15–35, 2006.

[64] S. D. Gertz and W. C. Roberts. Hemodynamic shear force in rupture of coronary arterial atherosclerotic plaques. *Am. J. Cardiol.*, pages 1368–1372, 1990.

[65] S. Glagov. Intimal hyperplasia, vascular modeling, and the restenosis problem. *Circulation*, 89:2888–2891, 1994.

[66] S. Glagov and C. K. Zarins. Is intimal hyperplasia an adaptive response or a pathological process? observations on the nature of nonatherosclerotic intimal thickening. *J. Vasc. Surg.*, 10:571–573, 1989.

[67] R. Glowinski, J. L. Lions, and R. Trémolierès. *Numerical Analysis of Variational Inequalities*. North-Holland Publishing Company, Amsterdam, 1981.

[68] M. B. Gravins and G. S. Roubin. Histopathologic phenomena at the site of percutaneous transluminal coronary angioplasty. *Human Pathology*, 20:477–485, 1989.

[69] A. Grüntzig and D. A. Kumpe. Technique of percutaneous transluminal angioplasty with Grüntzig balloon catheter. *Am. J. Radiol.*, 132:547–552, 1979.

[70] N. Gundiah, M. B. Ratcliffe, and L. A. Pruitt. Determination of strain energy function for arterial elastin: Experiments using histology and mechanical tests. *J. Biomech.*, 40:586–594, 2007.

[71] T. S. Hatsukami, R. Ross, and C. Yuan. Visualization of fibrous cap thickness and rupture in human atherosclerotic carotid plaque in-vivo with high resolution magnetic resonance imaging. *Circulation*, 102:959–964, 2000.

[72] S. Hirokawa, T. Ueki, and A. Ohtsuki. A new approach for surface fitting method of articular joint surfaces. *J. Biomech.*, 37:1551–1559, 2004.

[73] R. Hoffmann, G. S. Mintz, G. R. Dussaillant, J. J. Popma, A. D. Pichard, L. F. Satler, K. M. Kent, J. Griffin, and M. B. Leon. Patterns and mechanisms of in-stent restenosis. A serial intravascular ultrasound study. *Circulation*, 94:1247–1254, 1996.

[74] R. Hoffmann, G. S. Mintz, R. Mehran, K. M. Kent, A. D. Pichard, L. F. Satler, and M. B. Leon. Tissue proliferation within and surrounding Palmaz-Schatz stents is dependent on the aggressiveness of stent implanation technique. *Am. J. Cardiol.*, 83:1170–1174, 1999.

[75] M. Hoher, J. Wohrle, O. C. Grebe, M. Kochs, H. H. Osterhues, V. Hombach, and A. B. Buchwald. A randomized trial of elective stenting after balloon recanalization of chronic total occlusions. *J. Am. Coll. Cardiol.*, 34:722–729, 1999.

[76] G. A. Holzapfel. *Nonlinear Solid Mechanics. A Continuum Approach for Engineering*. John Wiley & Sons, Chichester, 2000.

[77] G. A. Holzapfel. Determination of material models for arterial walls from uniaxial extension tests and histological structure. *J. Theor. Biol.*, 238:290–302, 2006.

[78] G. A. Holzapfel. Collagen in arterial walls. Biomechanical aspects. In P. Fratzl, editor, *Collagen. Structure and Mechanics*, Heidelberg, in press. Springer-Verlag.

[79] G. A. Holzapfel and T. C. Gasser. A viscoelastic model for fiber-reinforced composites at finite strains: Continuum basis, computational aspects and applications. *Comput. Meth. Appl. Mech. Eng.*, 190:4379–4403, 2001.

[80] G. A. Holzapfel, T. C. Gasser, and R. W. Ogden. A new constitutive framework for arterial wall mechanics and a comparative study of material models. *J. Elasticity*, 61:1–48, 2000.

[81] G. A. Holzapfel, T. C. Gasser, and R. W. Ogden. Comparison of a multi-layer structural model for arterial walls with a Fung-type model, and issues of material stability. *J. Biomech. Eng.*, 126:264–275, 2004.

[82] G. A. Holzapfel and R. W. Ogden, editors. *Mechanics of Biological Tissue*. Springer-Verlag, Heidelberg, 2006.

[83] G. A. Holzapfel, C. A. J. Schulze-Bauer, and M. Stadler. Mechanics of angioplasty: Wall, balloon and stent. In J. Casey and G. Bao, editors, *Mechanics in Biology*, New York, 2000. The American Society of Mechanical Engineers (ASME). AMD-Vol. 242/BED-Vol. 46, pp. 141–156.

[84] G. A. Holzapfel, G. Sommer, C. T. Gasser, and P. Regitnig. Determination of the layer-specific mechanical properties of human coronary arteries with non-atherosclerotic intimal thickening, and related constitutive modelling. *Am. J. Physiol. Heart Circ. Physiol.*, 289:H2048–2058, 2005.

[85] G. A. Holzapfel, G. Sommer, and P. Regitnig. Anisotropic mechanical properties of tissue components in human atherosclerotic plaques. *J. Biomech. Eng.*, 126:657–665, 2004.

[86] G. A. Holzapfel, M. Stadler, and T. C. Gasser. Changes in the mechanical environment of stenotic arteries during interaction with stents: Computational assessment of parametric stent design. *J. Biomech. Eng.*, 127:166–180, 2005.

[87] G. A. Holzapfel, M. Stadler, and C. A. J. Schulze-Bauer. A layer-specific three-dimensional model for the simulation of balloon angioplasty using magnetic resonance imaging and mechanical testing. *Ann. Biomed. Eng.*, 30:753–767, 2002.

[88] G. A. Holzapfel and H. W. Weizsäcker. Biomechanical behavior of the arterial wall and its numerical characterization. *Comp. Biol. Med.*, 28:377–392, 1998.

[89] H. Huang, R. Virmani, H. Younis, A. P. Burke, R. D. Kamm, and R. T. Lee. The impact of calcification upon the biomechanical stability of atherosclerotic plaques. *Circulation*, 103:1051–1056, 2001.

[90] J. Hulthe and B. Fagerberg. Circulating oxidized LDL is associated with subclinical atherosclerosis development and inflammatory cytokines (AIR study). *Arterioscl. Thromb. and Vasc. Biol.*, 22:1162–1167, 2002.

[91] J. D. Humphrey. *Cardiovascular Solid Mechanics. Cells, Tissues, and Organs*. Springer-Verlag, New York, 2002.

[92] A. Ibrahimbegović and M. Al Mikdad. Finite rotations in dynamics of beams and implicit time-stepping schemes. *Int. J. Numer. Meth. Eng.*, 66:781–814, 1998.

[93] R. Iijima, J. Mehilli, A. Schömig, and A. Kastrati. Clinical evidence on polymer-based sirolimus and paclitaxel eluting stents. *Minerva Cardioangiol.*, 54:539–555, 2006.

[94] I.-K. Jang, G. Tearney, and B. Bouma. Visualization of tissue prolapse between coronary stent struts by optical coherence tomography. Comparison with intravascular untrasound. *Circulation*, 104:2754, 2001.

[95] P. Kagan, A. Fischer, and P. Z. Bar-Yoseph. New B-spline finite element approach for geometrical design and mechanical analysis. *Int. J. Numer. Meth. Eng.*, 41:435–458, 1998.

[96] N. Karajan, W. Ehlers, B. Markert, A. Acartürk, and C. Wieners. FE treatment of inhomogeneities within the intervertebral disc. 5:237–238, 2005.

[97] A. Kastrati, J. Mehilli, J. Dirschinger, F. Dotzer, H. Schühlen, F.-J. Neumann, M. Fleckenstein, C. Pfafferott, M. Seyfarth, and A. Schömig. Intracoronary stenting and angiographic results: strut thickness effect on restenosis outcome (ISAR-STEREO) trial. *Circulation*, 103:2816–2821, 2001.

[98] D. E. Kiousis, T. C. Gasser, and G. A. Holzapfel. Smooth contact strategies with emphasis on the modeling of balloon angioplasty with stenting. submitted.

[99] D. E. Kiousis, T. C. Gasser, and G. A. Holzapfel. A numerical model to study the interaction of vascular stents with human atherosclerotic lesions. *Ann. Biomed. Eng.*, 35:1857–1869, 2007.

[100] D. E. Kiousis, A. Wulff, and G. A. Holzapfel. Experimental studies and numerical analysis of the inflation and interaction of vascular balloon catheter-stent systems. *Ann. Biomed. Eng.*, 2008. in press.

[101] A. König, T. M. Schiele, J. Rieber, K. Theisen, H. Mudra, and V. Klauss. Influence of stent design and deployment technique on neointima formation and vascular remodeling. *Z. Kardiol.*, 91:98–102, 2002.

[102] J. Korelc. Automatic generation of finite-element code by simultaneous optimization of expressions. *Theor. Comput. Sci.*, 187:231–248, 1997.

[103] R. Kornowski, M. K. Hong, F. O. Tio, O. Bramwell, H. Wu, and M. B. Leon. In-stent restenosis: contributions of inflammatory responses and arterial injury to neointimal hyperplasia. *J. Am. Coll. Cardiol.*, 31:224–230, 1998.

[104] L. Krstulović-Opara, P. Wriggers, and J. Korelc. Symbolically generated 3D smooth polynomial frictional contact element based on the quartic Bézier surfaces. In *CD–ROM Proceedings of the European Congress on Computational Methods in Applied Sciences and Engineering, ECCOMAS 2000*, E. Oñate and G. Bugeda and B. Suárez (Eds), Barcelona, Spain, 2000.

[105] L. Krstulović-Opara, P. Wriggers, and J. Korelc. A C^1-continuous formulation for 3D finite deformation frictional contact. *Comput. Mech.*, 29:27–42, 2002.

[106] C. Lally, F. Dolan, and P. J. Prendergast. Cardiovascular stent design and vessel stresses: a finite element analysis. *J. Biomech.*, 38:1574–1581, 2005.

[107] T. A. Laursen. *Computational Contact and Impact Mechanics*. Springer-Verlag, Berlin, 2002.

[108] T. A. Laursen and J. C. Simo. A continuum-based finite element formulation for the implicit solution of multibody, large deformation frictional contact problems. *Int. J. Numer. Meth. Eng.*, 36:3451–3485, 1993.

[109] R. T. Lee, H. M. Loree, G. C. Cheng, E. H. Lieberman, N. Jaramillo, and F. J. Schoen. Computational structural analysis based on intravascular ultrasound imaging before *in vitro* angioplasty: Prediction of plaque fracture locations. *J. Am. Coll. Cardiol.*, 21:777–782, 1993.

[110] R. T. Lee, F. J. Schoen, H. M. Loree, M. W. Lark, and P. Libby. Circumferential stress and matrix metalloproteinase 1 in human coronary atherosclerosis. Implications for plaque rupture. *Arterioscl. Thromb. and Vasc. Biol.*, 16:1070–1073, 1996.

[111] D. Y. Leung, S. Glagov, and M. B. Mathews. Cyclic stretching stimulates synthesis of matrix components by arterial smooth muscle cells *in vitro*. *Science*, 191:475–477, 1976.

[112] Z. Y. Li, S. P. Howarth, T. Tang, and J. H. Gillard. How critical is fibrous cap thickness to carotid plaque stability? A flow-plaque interaction model. *Stroke*, 37:1195–1199, 2006.

[113] Z. Y. Li, S. P. Howarth, R. A. Trivedi, J. M. U-King-Im, M. J. Graves, A. Brown, L. Wang, and J. H. Gillard. Stress analysis of carotid plaque rupture based on in vivo high resolution MRI. *J. Biomech.*, 39:2611–2622, 2006.

[114] D. K. Liang, D. Z. Yang, M. Qi, and W. Q. Wang. Finite element analysis of the implementation of a balloon expandable stent in a stenosed artery. *Int. J. Cardiol.*, 104:314–318, 2005.

[115] P. Libby. Current concepts of the pathogenesis of the acute coronary syndromes. *Circulation*, 104:365–372, 2001.

[116] H. M. Loree, R. D. Kamm, R. G. Stringfellow, and R. T. Lee. Effects of fibrous cap thickness on peak circumferential stress in model atherosclerotic vessels. *Circ. Res.*, 71:850–858, 1992.

[117] R. T. Lyon, C. K. Zarins, C. T. Lu, C. F. Yang, and S. Glagov. Vessel, plaque and lumen morphology after transluminal balloon angioplasty. Quantitative study in distended human arteries. *Arteriosclerosis*, 7:306–314, 1987.

[118] C. DeBoor. *A practical Guide to Splines*. Springer, Berlin, 1978.

[119] M. R. Kaazempur-Mofrad, A. G. Isasi, H. F. Younis, R. C. Chan, D. P. Hinton, G. Sukhova, G. M. LaMuraglia, R. T. Lee, and R. D. Kamm. Characterization of the atherosclerotic carotid bifurcation using MRI, finite element modeling, and histology. *Ann. Biomed. Eng.*, 32:932–946, 2004.

[120] J. P. McGarry, B. P. O'Donnell, P. E. McHugh, and J. G. McGarry. Analysis of the mechanical performance of a cardiovascular stent design based on micromechanical modelling. *Comp. Mater. Sci.*, 31:421–438, 2004.

[121] L. J. Van Ruijven, M. Beek, and T. M. G. J. Van Eijden. Fitting parametrized polynomials with scattered surface data. *J. Biomech.*, 32:715–720, 1999.

[122] D. R. McLean and N. L. Eiger. Stent design: implications for restenosis. *Rev. Cardiovas. Med.*, 3:16–22, 2002.

[123] R. McNeel and Associates. *Rhinoceros – NURBS modeling for Windows, Version 3.0 User's Guide*. Seattle, Washington, 2005.

[124] F. Migliavacca, L. Petrini, M. Colombo, F. Auricchio, and R. Pietrabissa. Mechanical behavior of coronary stents investigated through the finite element method. *J. Biomech.*, 35:803–811, 2002.

[125] F. Migliavacca, L. Petrini, P. Massarotti, S. Schievano, F. Auricchio, and G. Dubini. Stainless and shape memory alloy coronary stents: a computational study on the interaction with the vascular wall. *Biomech. Model. Mechanobio.*, 2:205–217, 2004.

[126] F. Migliavacca, L. Petrini, V. Montanari, I. Quagliana, F. Auricchio, and G. Dubini. A predictive study of the mechanical behaviour of coronary stents by computer modelling. *Med. Eng. Phys.*, 27:13–18, 2005.

[127] P. Moreno, E. Falk, I. Palacios, J. B. Newell, V. Fuster, and J. T. Fallon. Macrophage infiltration in acute coronary syndromes. Implications for plaque rupture. *Circulation*, 90:2775–778, 1994.

[128] A. C. Morton, D. Crossman, and J. Gunn. The influence of physical stent parameters upon restenosis. *Pathol. Biol. (Paris)*, 52:196–205, 2004.

[129] J. W. Moses, M. B. Leon, J. J. Popma, P. J. Fitzgerald, D. R. Holmes, C. O'Shaughnessy, R. P. Caputo, D. J. Kereiakes, D. O. Williams, P. S. Teirstein, J. L. Jaeger, R. E. Kuntz, and SIRIUS Investigators. Sirolimus-eluting stents versus standard stents in patients with stenosis in a native coronary artery. *N. Engl. J. Med.*, 349:1315–1323, 2003.

[130] D. W. M. Muller, S. G. Ellis, and E. J. Topol. Experimental models of coronary artery restenosis. *J. Am. Coll. Cardiol.*, 19:418–432, 1992.

[131] S. T. Nikkari and A. W. Clowes. Restenosis after vascular reconstruction. *Ann. Med.*, 26:95–100, 1994.

[132] E. M. Ohman, D. L. Bhatt, P. G. Steg, S. Goto, A. T. Hirsch, C. S. Liau, J. L. Mas, A. J. Richard, J. Röther, P. W. Wilson, and REACH Registry Investigators. The REduction of Atherothrombosis for Continued Health (REACH) Registry: an international, prospective, observational investigation in subjects at risk for atherothrombotic events-study design. *Am. Heart J.*, 151:786.e1–10, 2006.

[133] T. Olbrich and A. Murray. Assessment of computer–controlled inflation/deflation for determining the properties of PTCA balloon catheters with pressure–volume curves. *Physiol. Meas.*, 22:299–308, 2001.

[134] J. A. Ormiston, S. R. Dixon, M. W. Webster, P. N. Ruygrok, J. T. Stewart, I. Minchington, and T. West. Stent longitudinal flexibility: a comparison of 13 stent designs before and after balloon expansion. *Catheter Cardiovasc. Interv.*, 50:120–124, 2000.

[135] J. Pache, A. Kastrati, J. Mehilli, H. Schühlen, F. Dotzer, J. Hausleiter, M. Fleckenstein, F. J. Neumann, U. Sattelberger, C. Schmitt, M. Muller, J. Dirschinger, and A. Schömig. Intracoronary stenting and angiographic results: strut thickness effect on restenosis outcome (ISAR-STEREO-2) trial. *J. Am. Coll. Cardiol.*, 41:1283–1288, 2003.

[136] V. Padmanabhan and T. A. Laursen. A framework for development of surface smoothing procedures in large deformation frictional contact analysis. *Finite Elem. Anal. Des.*, 37:173–198, 2001.

[137] S. Petersen, V. Peto, M. Rayner, J. Leal, R. Luengo-Fernandez, and A. Gray. *European Cardiovascular Disease Statistics, 2005 Edition*. British Heart Foundation Health Promotion Research Group and Department of Public Health, University of Oxford, 2005.

[138] L. A. Piegel and W. Tiller. *The NURBS Book*. Springer-Verlag, New York, 2nd edition, 1997.

[139] G. Pietrzak and A. Curnier. Continuum mechanics modelling and augmented Lagrangian formulation of multibody, large deformation frictional contact problems. In *Proceedings of COMPLAS, Vol. 5*, D. R. Owen and E. Hinton and E.

Oñate (Eds.), Barcelona, 1997. International Center for Numerical Methods in Engineering (CIMNE). 878–883.

[140] M. A. Puso and T. A. Laursen. A 3D smoothing method using Gregory patches. In *USACM Sixth U.S. National Congress on Computational Mechanics: Abstracts*, University of Michigan, 2001. Mechanical Engineering Department.

[141] M. A. Puso and T. A. Laursen. A mortar segment-to-segment frictional contact method for large deformations. *Comput. Meth. Appl. Mech. Eng.*, 193:4891–4913, 2004.

[142] J. A. G. Rhodin. Architecture of the vessel wall. In D. F. Bohr, A. D. Somlyo, and H. V. Sparks, editors, *Handbook of Physiology, The Cardiovascular System*, volume 2, pages 1–31. American Physiologial Society, Bethesda, Maryland, 1980.

[143] P. D. Richardson, M. J. Davies, and G. V. R. Born. Influence of plaque configuration and stress distribution on fissuring of coronary atherosclerotic plaques. *Lancet*, 2(8669):941–944, 1989.

[144] R. Rieu, P. Barragan, C. Masson, J. Fuseri, V. Garitey, M. Silvestri, P. Roquebert, and J. Sainsous. Radial force of coronary stents: a comparative analysis. *Catheter Cardiovasc. Interv.*, 46:380–391, 1999.

[145] C. Rogers and E. R. Edelman. Endovascular stent design dictates experimental restenosis and thrombosis. *Circulation*, 91:2995–3001, 1995.

[146] C. Rogers, D. Y. Tseng, J. C. Squire, and E. R. Edelman. Balloon-artery interactions during stent placement: a finite element analysis approach to pressure, compliance and stent design as contributors to vascular injury. *Circ. Res.*, 84:378–383, 1999.

[147] W. J. Rogers, J. W. Prichard, Y. L. Hu, P. R. Olson, D. H. Benckart, C. M. Kramer, D. A. Vido, and N. Reichek. Characterization of signal properties in atherosclerotic plaque components by intravascular MRI. *Arterioscl. Thromb. and Vasc. Biol.*, 20:1824–1830, 2000.

[148] W. Rosamond, K. Flegal, K. Furie, A. Go, K. Greenlund, N. Haase, S. M. Hailpern, M. Ho, V. Howard, B. Kissela, S. Kittner, D. Lloyd-Jones, M. McDermott, J. Meigs, C. Moy, G. Nichol, C. O'Donnell, V. Roger, P. Sorlie, J. Steinberger, T. Thom, M. Wilson, Y. Hong, American Heart Association Statistics Committee, and Stroke Statistics Subcommittee. *Heart Disease and Stroke Statistics – 2008 Update*, volume 117. A Report From the American Heart Association Statistics Committee and Stroke Statistics Subcommittee, 2008.

[149] R. Ross. The pathogenesis of atherosclerosis: a perspective for the 1990's. *Nature*, 362:801–809, 1993.

[150] N. V. Salunke and L. D. T. Topoleski. Biomechanics of atherosclerotic plaque. *Crit. Rev. Biomed. Eng.*, 25:243–285, 1997.

[151] C. A. J. Schulze-Bauer, C. Mörth, and G. A. Holzapfel. Passive biaxial mechanical response of aged human iliac arteries. *J. Biomech. Eng.*, 125:395–406, 2003.

[152] C. A. J. Schulze-Bauer, P. Regitnig, and G. A. Holzapfel. Mechanics of the human femoral adventitia including high-pressure response. *Am. J. Physiol. Heart Circ. Physiol.*, 282:H2427–H2440, 2002.

[153] R. S. Schwartz and T. D. Henry. Pathophysiology of coronary artery restenosis. *Rev. Cardiovas. Med.*, 3, Suppl. 5:S4–S9, 2002.

[154] R. S. Schwartz, K. C. Huber, J. G. Murphy, W. D. Edwards, A. R. Camrud, R. E. Vliestra, and D. R. Holmes. Restenosis and proportional neointimal response to coronary artery injury: results in a porcine model. *J. Am. Coll. Cardiol.*, 19:267–274, 1992.

[155] S. M. Schwartz. Smooth muscle migration in atherosclerosis and restenosis. *J. Clin. Invest.*, 100:S87–89, 1997.

[156] P. W. Serruys, P. de Jaegere, F. Kiemeneij, C. Macaya, W. Rutsch, G. Heyndrickx, H. Emanuelsson, J. Marco, V. Legrand, P. Materne, J. Belardi, U. Sijwart, A. Colombo, J. Goy, P. van den Heuvel, J. Delcan, and M. Morel. A comparison of balloon-expandable-stent implantation with balloon angioplasty in patients with coronary artery disease. Benestent Study Group. *N. Engl. J. Med.*, 331:489–495, 1994.

[157] M. Shinnar, J. T. Fallon, S. Wehrli, M. Levin, D. Dalmacy, Z. A. Fayad, J. J. Badimon, M. Harrington, E. Harrington, and V. Fuster. The diagnostic accuracy of *ex vivo* MRI for human atherosclerotic plaque characterization. *Arterioscl. Thromb. and Vasc. Biol.*, 19:2756–2761, 1999.

[158] G. Sommer and G. A. Holzapfel. 3D constitutive modeling of the biaxial mechanical response of intact and layer-dissected human carotid arteries. *J. Biomech.*, 2008. Submitted.

[159] G. Sommer, P. Regitnig, L. Koeltringer, and G. A. Holzapfel. Biaxial mechanical properties of intact and layer-dissected human carotid arteries at physiological and supra-physiological loadings. *Am. J. Physiol. Heart Circ. Physiol.*, 2008. Submitted.

[160] M. Stadler and G. A. Holzapfel. Subdivision schemes for smooth contact surfaces of arbitrary mesh topology in 3D. *Int. J. Numer. Meth. Eng.*, 60:1161–1195, 2004.

[161] M. Stadler, G. A. Holzapfel, and J. Korelc. C^n-continuous modeling of smooth contact surfaces using NURBS and applications to 2D problems. *Int. J. Numer. Meth. Eng.*, 57:2177–2203, 2003.

[162] H. C. Stary. *An Atlas of Atherosclerosis Progression and Regression*. Parthenon, New York, 1999.

[163] H. C. Stary. *Atlas of Atherosclerosis: Progression and Regression*. The Parthenon Publishing Group, Boca Raton, London, New York, Washington, D.C., 2nd edition, 2003.

[164] A. Stiaras. *The InVision Guide to a Healthy Heart*. JHarperCollins, New York, 2005.

[165] J. Stolpmann, H. Brauer, H.-J. Stracke, R. Erbel, and A. Fischer. Practicability and limitations of finite element simulation of the dilation behaviour of coronary stents. *Mat.-wiss. u. Werkstofftechn.*, 34:736–745, 2003.

[166] G. W. Stone, S. G. Ellis, D. A. Cox, J. Hermiller, C. O'Shaughnessy, J. T. Mann, M. Turco, R. Caputo, P. Bergin, J. Greenberg, J. J. Popma, M. E. Russell, and TAXUS-IV Investigators. One-year clinical results with the slow-release, polymer-based, paclitaxel-eluting TAXUS stent: the TAXUS-IV trial. *Circulation*, 109:1942–1947, 2004.

[167] T. M. Sullivan, S. D. Ainsworth, E. M. Langan, S. Taylor, B. Snyder, D. Cull, J. Youkey, and M. Laberge. Effect of endovascular stent strut geometry on vascular injury, myointimal hyperplasia, and restenosis. *J. Vasc. Res.*, 36:143–149, 2002.

[168] L. A. Taber. Biomechanics of growth, remodelling, and morphognesis. *Appl. Mech. Rev.*, 48:487–543, 1995.

[169] D. Tang, C. Yang, J. Zheng, P. K. Woodard, J. E. Saffitz, J. D. Petruccelli, G. A. Sicard, and C. Yuan. Local maximal stress hypothesis and computational plaque vulnerability index for atherosclerotic plaque assessment. *Ann. Biomed. Eng.*, 33:1789–1801, 2005.

[170] D. Tang, C. Yang, J. Zheng, P. K. Woodard, J. E. Saffitz, G. A. Sicard, T. K. Pilgram, and C. Yuan. Quantifying effects of plaque structure and material properties on stress distributions in human atherosclerotic plaques using 3D FSI models. *J. Biomech. Eng.*, 127:1185–1194, 2005.

[171] R. L. Taylor. *FEAP – A Finite Element Analysis Program, Version 7.5 User Manual*. University of California at Berkeley, Berkeley, California, 2005.

[172] CUBIT Team. *CUBIT 10.0 User's Manual*. Sandia National Laboratories, Albuquerque, New Mexico, USA, 2005.

[173] A. N. Tenaglia, C. E. Buller, K. B. Kisslo, R. S. Stack, and C. J. Davidson. Mechanisms of balloon angioplasty and directional coronary atherectomy assessed by intracoronary ultrasound. *J. Am. Coll. Cardiol.*, 20:685–691, 1992.

[174] L. H. Timmins, M. R. Moreno, C. A. Meyer, J. C. Criscione, A. Rachev, and J. E. Moore Jr. Stented artery biomechanics and device design optimization. *Med. Biol. Eng. Comput.*, 45:505–513, 2007.

[175] J. F. Toussaint, G. M. LaMuraglia, J. F. Southern, V. Fuster, and H. L. Kantor. Magnetic resonance images lipid, fibrous, calcified, hemorrhagic, and thrombotic components of human atherosclerosis *in vivo*. *Circulation*, 94:932–938, 1996.

[176] R. A. Trivedi, J. U-King-Im, M. J. Graves, J. Horsley, M. Goddard, P. J. Kirkpatrick, and J. H. Gillard. Multi-sequence in vivo MRI can quantify fibrous cap and lipid core components in human carotid atherosclerotic plaques. *Eur. J. Vasc. Endovasc. Surg.*, 28:207–213, 2004.

[177] T. Thom et al. *Heart Disease and Stroke Statistics – 2006 Update*, volume 113. A Report From the American Heart Association Statistics Committee and Stroke Statistics Subcommittee, 2006.

[178] A. Versluis, A. J. Bank, and W. H. Douglas. Fatigue and plaque rupture in myocardial infarction. *J. Biomech.*, 39:339–347, 2006.

[179] R. Virmani, A. P. Burke, and A. Farb. Plaque rupture and plaque erosion. 82:1–3, 1999.

[180] B. F. Waller. Crackers, breakers, stretchers, drillers, scrapers, shavers, burners, welders and melters - the future treatment of atherosclerotic coronary disease? a clinical-morphological assessment. *J. Am. Coll. Cardiol.*, 13:969–987, 1989.

[181] D. L. Wang, B. S. Wung, Y. J. Shyy, C. F. Lin, Y. J. Chao, S. Usami, and S. Chien. Mechanical strain induces monocyte chemotactic protein-1 gene expression in endothelial cells. Effects of mechanical strain on monocyte adhesion to endothelial cells. *Circ. Res.*, 77:294–302, 1995.

[182] W. Q. Wang, D. K. Liang, D. Z. Yang, and M. Qi. Analysis of the transient expansion behavior and design optimization of coronary stents by finite element method. *J. Biomech.*, 39:21–32, 2006.

[183] H. W. Weizsäcker and J. G. Pinto. Isotropy and anisotropy of the arterial wall. *J. Biomech.*, 21:477–487, 1988.

[184] J. J. Wentzel, J. Kloet, I. Andhyiswara, J. A. Oomen, J. C. Schuurbiers, B. J. de Semet, M. J. Post, D. de Kleijn, G. Paterkamp, C. Borst, C. J. Slager, and R. Krams. Shear-stress and wall-stress regulation of vascular remodeling after balloon angioplasty: effect of matrix metalloproteinase inhibition. *Circulation*, 104:91–96, 2001.

[185] Inc. Wolfram Research. *Mathematica 5.2*. Wolfram Research, Inc., Champaign, Illinois, 2005.

[186] P. Wriggers. *Computational Contact Mechanics*. John Wiley & Sons, Chichester, 2002.

[187] P. Wriggers, L. Krstulovic-Opara, and J. Korelc. Smooth C^1-interpolations for two-dimensional frictional contact problems. *Int. J. Numer. Meth. Eng.*, 51:1469–1495, 2001.

[188] P. Wriggers, C. Miehe, M. Kleiber, and J. C. Simo. On the coupled thermomechanical treatment of necking problems via finite element methods. *Int. J. Numer. Meth. Eng.*, 33:869–883, 1992.

[189] W. Rosamond et al. *Heart Disease and Stroke Statistics – 2007 Update*, volume 115. A Report From the American Heart Association Statistics Committee and Stroke Statistics Subcommittee, 2007.

[190] W. Wu, W. Q. Wang, D. Z. Yang, and M. Qi. Stent expansion in curved vessel and their interactions: a finite element analysis. *J. Biomech.*, 40:2580–2585, 2007.

[191] Z. Xia, F. Ju, and K. Sasaki. A general finite element analysis method for balloon expandable stents based on repeated unit cell (RUC) model. *Finite Elem. Anal. Des.*, 43:649–658, 2007.

[192] C. Yuan, L. M. Mitsumori, K. W. Beach, and K. R. Maravilla. Carotid atherosclerotic plaque: noninvasive MR characterization and identification of vulnerable lesions. *Radiology*, 221:285–299, 2001.

[193] C. Yuan, L. M. Mitsumori, M. S. Ferguson, N. L. Polissar, D. Echelard, G. Ortiz, R. Small, J. W. Davies, W. S. Kerwin, and T. S. Hatsukami. In vivo accuracy of multispectral magnetic resonance imaging for identifying lipid-rich necrotic cores and intraplaque hemorrhage in advanced human carotid plaques. *Circulation*, 104:2051–2056, 2001.

[194] J. Zheng, I. El Naqa, F. E. Rowold, T. K. Pilgram, P. K. Woodard, J. E. Saffitz, and D. Tang. Quantitative assessment of coronary artery plaque vulnerability by high-resolution magnetic resonance imaging and computational biomechanics: a pilot study ex vivo. *Magn. Reson. Med.*, 54:1360–1368, 2005.

[195] J. Zhou and Y. C. Fung. The degree of nonlinearity and anisotropy of blood vessel elasticity. *Proc. Natl. Acad. Sci. USA*, 94:14255–14260, 1997.

Monographic Series TU Graz

Computation in Engineering and Science

Vol. 1 Steffen Alvermann
Effective Viscoelastic Behaviour of Cellular Auxetic Materials
2008
ISBN 978-3-902465-92-4

Vol. 2 Sendy Fransiscus Tantono
The Mechanical Behavior of a Soilbag under Vertical Compression
2008
ISBN 978-3-902465-97-9

Vol. 3 Thomas Rüberg
Non-conforming FEM/BEM Coupling in Time Domain
2008
ISBN 978-3-902465-98-6

Vol. 4 Dimitrios E. Kiousis
Biomechanical and Computational Modeling of Atherosclerotic Arteries
2008
ISBN 978-3-85125-023-7